University of Latvia

FACULTY OF PHYSICS, MATHEMATICS AND OPTOMETRY

Katrīna Laganovska

DEFECTS AND OPTICAL PROPERTIES OF UNDOPED AND RARE-EARTH DOPED HfO_2/ZrO_2

DOCTORAL THESIS

Submitted for the Degree of Doctor of Natural Sciences
Field of Physics and Astronomy
Subfield of Material Physics

Scientific supervisor: PhD. Phys. Krišjānis Šmits

RĪGA, 2024

Promocijas darbs izstrādāts Latvijas Universitātes Cietvielu fizikas institūtā laika posmā no 10.2017. līdz 01.2024.

Darbs sastāv no ievada, četrām nodaļām, aizstāvamām tēzēm un literatūras saraksta.
Darba forma: disertācija fizikas nozarē, Materiālu Fizikas apakšnozarē.

Darba vadītājs:
Dr. Phys. Krišjānis Šmits, vadošais pētnieks, Mikroskopijas laboratorijas vadītājs, LU Cietvielu fizikas institūts.

Darba recenzenti:
1. Dr. phys. Laima Trinklere, Latvijas Universitāte
2. Dr. habil. Phys. Artūrs Medvids, Rīgas Tehniskā universitāte
3. Dr. Valter Kiisk, Tartu Universitāte, Igaunija

Promocijas darba aizstāvēšana notiks Latvijas Universitātes Fizikas, astronomijas un mehānikas zinātņu nozares promocijas padomes atklātajā sēdē 2024. gada 17. janvārī, Ķengaraga ielā 8, Latvijas Universitātes Cietvielu fizikas institūta konferenču zālē.

Ar promocijas darbu un tā kopsavilkumu var iepazīties Latvijas Universitātes Bibliotēkā Kalpaka bulvārī 4, Rīgā un Latvijas Universitātes Akadēmiskajā bibliotēkā (Rūpniecības iela 10, Rīga).

Latvijas Universitātes Fizikas un astronomijas zinātņu nozares, materiālu fizikas apakšnozares promocijas padomes priekšsēdētājs	Dr. habil. phys. Ruvins Ferbers
Promocijas padomes sekretāre	Sintija Siliņa

Anotācija

Hafnija dioksīds ir kļuvis par iecienītu silīcija dioksīda aizstājēju lauktranzistoros, pateicoties tā augstajai dielektriskajai konstantei, plašajai aizliegtajai zonai, ķīmiskajai stabilitātei un kopējai saderībai ar silīcija dioksīda komponentēm. Turklāt, segnetoelektriskās fāzes esamības atklāšana hafnija dioksīdā ir atvērusi iespējas tā izmantošanai segnetoelektriskajās brīvpiekļuves atmiņās, segnetoelektriskajos lauktranzistoros, kā arī citos pielietojumos. Pateicoties tā īpašībām, hafnija dioksīds vairākos aspektos ir labāks par pašlaik izmantotajiem segnetoelektriskajiem materiāliem.

Galvenais izaicinājums izmantojot hafnija dioksīdu, ir tā relatīvi augstais pašvielas defektu daudzums. Šie defekti izraisa lielākas noplūdes strāvas plānajās kārtiņās, samazina ķīmisko stabilitāti, ietekmē segnetoelektrisko fāžu stabilitāti, kā arī materiāla raksturlielumus un īpašības kopumā.

Šo iemeslu dēļ, šis darbs koncentrējas uz **hafnija dioksīda un tā dvīņu oksīda cirkonija dioksīda pašvielas defektu pētīšanu**, izmantojot luminescences izmeklējumus, lai iegūtu informāciju par defektu apkārtni un izcelsmi, papildus izmantojot termostimulēto luminescenci, lai noteiktu konkrēto defektu veidu un to ierosmes enerģijas. Lai gan par šo tēmu ir veikti daudzi teorētiskie pētījumi, sistemātiska eksperimentāla izpēte līdz šim nav bijusi realizēta.

Galvenās tēmas, kas tiek apskatītas šajā disertācijā, ir:

1. Skābekļa vakanču sadalījuma un koncentrācijas ietekme uz rezultējošo retzemju jonu luminescenci.
2. Retzemju jonu zonžu izmantošana saķepināšanas procesu kontrolēšanai keramikās.
3. Skābekļa vakanču veidu identificēšana monoklīnajā hafnijā.
4. Skābekļa vakanču rašanās un to ietekme uz retzemju jonu iebūvēšanos pamatmatricā.

Hafnija dioksīds ir daudzsološs elektroniskais materiāls un zināšanas par defektu cēloņiem, veidiem un īpašībām sniedz jaunu izpratni par to, kā tos novērst, lai uzlabotu kopējo materiāla kvalitāti un pielāgotu to aktuālajiem augsta pieprasījuma pielietojumiem.

Abstract

Hafnium oxide currently replaces silicon dioxide as the gate oxide in metal-oxide-semiconductor transistors of ultra-high density integrated circuits. It is selected due to its high dielectric constant, broad band gap, chemical stability, and compatibility with silica.

Furthermore, the discovery of a ferroelectric phase existence in hafnia has opened up its use in applications such as ferroelectric random-access memories, ferroelectric transistors and others, having properties that surpass many of the existing ferroelectric materials.

The main challenge presented by hafnia is its relatively high amount of intrinsic defects. Defects lead to larger leakage currents in thin films, reduce the chemical stability, impact the stability of the ferroelectric phases and overall affect the characteristics and properties of the material.

This work, therefore, focuses on the **study of intrinsic defects found in hafnia and its twin oxide zirconia**, using luminescent probes to gather information about defect surroundings and origins, as well as using thermoluminescence to determine the exact type of defects present and their excitation energies. Despite numerous theoretical studies on the subject, a thorough experimental investigation had not yet been performed.

The main topics covered in this thesis are:

1. Impact of oxygen vacancy distribution and concentration on the resulting rare-earth ion luminescence.
2. Use of rare-earth ion probes as a way to control the sintering processes in ceramics.
3. Identification of oxygen vacancy types in monoclinic hafnia.
4. Creation of oxygen vacancies and their impact on rare-earth ion distribution in the host matrix.

Hafnia is a highly promising electronic material and the knowledge of causes, types, and characteristics of intrinsic defects present provides a new understanding of how to limit these defects and improve the overall properties to further advance the quality of the material and its uses in high-demand applications.

List of abbreviations

CMOS - Complementary Metal-Oxide-Semiconductor

k – dielectric constant

CN – Coordination Number

sX – Screened exchange (method)

WDA – Weighted Density Approximation

DOS – Density Of States

PDOS - Projected Density Of States

VB – Valence Band

CB – Conduction Band

EPR – Electron Paramagnetic Resonance

DFT – Density Functional Theory

GGA - Generalized Gradient Approximation

GGA+U - Generalized Gradient Approximation plus Hubbard- U correction

VBM - Valence-Band Maximum

DMC - Diffusion Monte Carlo

ALD – Atomic Layer Deposition

PL – Photoluminescence

PLE – Photoluminescence Excitation

TL – Thermoluminescence

XPS - X-ray Photoelectron Spectroscopy

XRD – X-ray Diffraction

DRS – Diffuse Reflectance Spectrum

OA – Optical Absorption

STE – Self-Trapped Excitons

FE – Free Excitons

ED – Electric Dipole

MD – Magnetic Dipole

ET – Energy Transfer

EOT - Equivalent Oxide Thickness

FeRAM – Ferroelectric Random-Access Memory

FeFET – Ferroelectric Field-Effect Transistor

NEMS – Nano-Electro-Mechanical-Systems

SEM – Scanning Electron Microscopy

TEM – Transmission Electron Microscopy

TLD – Through-the-Lens Detector

CCD - Charge-Coupled Device

XRL – X-ray Luminescence

JO – Judd-Ofelt

SPVD – Solar Physical Vapor Deposition

FIB – Focused Ion Beam

RT – Room Temperature

FWHM – Full Width at Half Maximum

VO – oxygen vacancy

$\mathbf{VO}_3^{1+}$ – singly charged threefold coordinated oxygen vacancy

$\mathbf{VO}_3^{2+}$ – doubly charged threefold coordinated oxygen vacancy

$\mathbf{VO}_4^{1+}$ – singly charged fourfold coordinated oxygen vacancy

$\mathbf{VO}_4^{2+}$ – doubly charged fourfold coordinated oxygen vacancy

CONTENTS

1.INTRODUCTION

1.1 Motivation

Following Moore's law [1] (the number of transistors in an integrated circuit doubles about every two years), the scaling down of silicon dioxide dielectrics was formerly thought to be a useful way to improve transistor performance in complementary metal-oxide semiconductor (CMOS) technology. Reduced silicon dioxide gate dielectric thickness has permitted larger numbers of transistors per chip with improved circuit functionality and performance at cheap costs in recent decades.

However, as devices approach the sub-45 nm scale, the effective oxide thickness of typical silicon dioxide dielectrics must be less than 1 nm, which is around 3 monolayers and close to the physical limit, resulting in large gate leakage currents due to the obvious quantum tunneling effect. To keep the downward scaling going, dielectrics with a higher dielectric constant (high-k) are being proposed as a way to get the same transistor performance while keeping the physical thickness low. [2]

Because of its desirable features such as a broad band gap of 5.25–5.95 eV [3] and a high-k value of 25 [4], hafnia has become a popular choice among high dielectric constant materials for CMOS. Hafnia also has a higher heat of formation than silica and has excellent chemical compatibility with silicon, as well as being chemically and thermally stable. Because gate stacks go through quick thermal annealing processes, this is very critical for the silica contact. Additionally, the recent discovery of a ferroelectric phase existence and the aforementioned properties, make hafnia a promising material for ferroelectric field-effect transistor (FeFET) and ferroelectric random-access memory (FeRAM) applications [5].

However, compared to SiO_2, HfO_2 has a higher defect concentration, resulting in a higher density of charge traps, transient instability of the gate threshold voltage, coulomb scattering of carriers in the substrate channel, and source-level voltage instability. Therefore it is of great importance to study the defects in HfO_2 and ZrO_2 [6], which is the focus of this thesis.

1.2 Aim

The aim of this work is to study the defects and optical properties in undoped and doped HfO_2 and ZrO_2 in order to understand the influence of defects such as oxygen vacancies on the resulting characteristics of these materials.

The following tasks are set:

1) study the impact of the vicinity and distribution of nearby oxygen vacancies on rare-earth ion luminescence when the phase transitions from monoclinic to tetragonal;

2) use rare-earth ion luminescent probes to show defect formation and phase transformation in nanostructured ZrO_2 ceramics during the sintering process;

3) identify VO_3^{1+}, VO_3^{2+} and VO_4^{1+}+VO_4^{2+} defects in monoclinic HfO_2 using thermoluminescence;

4) determine whether Eu^{3+} ions are incorporated in monoclinic HfO_2 as single ions as well as in pairs, creating VO_3^{1+} and VO_3^{2+} oxygen vacancies, respectively.

2.LITERATURE REVIEW

In many physical and chemical properties, HfO_2 resembles its twin oxide, ZrO_2. The resemblance is due to structural and electronic similarities between the two oxides, with atomic and ionic radii 0.78 Å and 0.79 Å for Hf^{4+} and Zr^{4+} respectively [7]. Therefore both are used in this study interchangeably.

2.1 Polymorphism in hafnia and zirconia

Hafnium oxide exhibits distinct properties depending on the crystal structure of the material, which can exist in different phases such as monoclinic, tetragonal, and cubic and others. Thus, it is crucial to differentiate between these phases and determine the conditions under which they arise to fully comprehend the characteristics of the material.

The most stable form of HfO_2 in ambient settings is a monoclinic fluorite-type crystal structure (Fig. 2.1), which is a polymorphic distortion of the cubic fluorite crystal structure. The monoclinic fluorite-type crystal structure belongs to the crystallographic space group P21/c [8]. Zr^{4+} and Hf^{4+} have similar electronic configurations, ionic radii (0.78 Å and 0.76 Å respectively, for (coordination number) CN=7), and electronegativities (1.22 eV and 1.23 eV, respectively)[9]. The Hf^{4+} ion is surrounded by a sevenfold oxygen coordination in the monoclinic fluorite-type crystal structure (Fig. 2.2A), which has four O_2 ions at the base of the cube, one at each corner, and two at the midpoints [1, 11]. The a, b, and c axes were found by Ruh et al.[10] to be parallel to the oxygens labeled IId-Ic, IIc-IId, and IId-IIa, respectively, based on Fig.2.1(G).

Although ZrO_2 and HfO_2 both exhibit monoclinic crystal structure, the monoclinic structure of HfO_2 is slightly smaller than the monoclinic structure of ZrO_2 due to the smaller ionic radius of Hf^{4+} in comparison to Zr^{4+} [11]. The great similarity between hafnium compounds and those of zirconium, is related to the electron configurations of hafnium and zirconium: (i)$4f^{14}5d^26s^2$ for hafnium, and (ii) $4d^25s^2$ for zirconium. The inner transition elements (cerium through lutetium) that come before hafnium produce this contraction by introducing electrons to the inner $4f$ shell. No outside electrons exist to offset the increased nuclear charge. Compared to ZrO_2, a reduction in atomic size leads to shorter bond lengths between the Hf^{4+} and O^{2-} atoms within the monoclinic structure [10, 11].

In contrast to typical rare-earth metals, Hf^{4+} and Zr^{4+} ions exhibit unusual chemical behavior and bonding characteristics (e.g., Ce). Studies on the chemistry of Zr^{4+} came to the conclusion that because of its relatively short ionic radius, the majority of its bonds with other atoms are covalent. In the monoclinic fluorite-type crystal structure, the sevenfold coordination is preferred, and covalent bonding is thought to at least partially account for this [12].

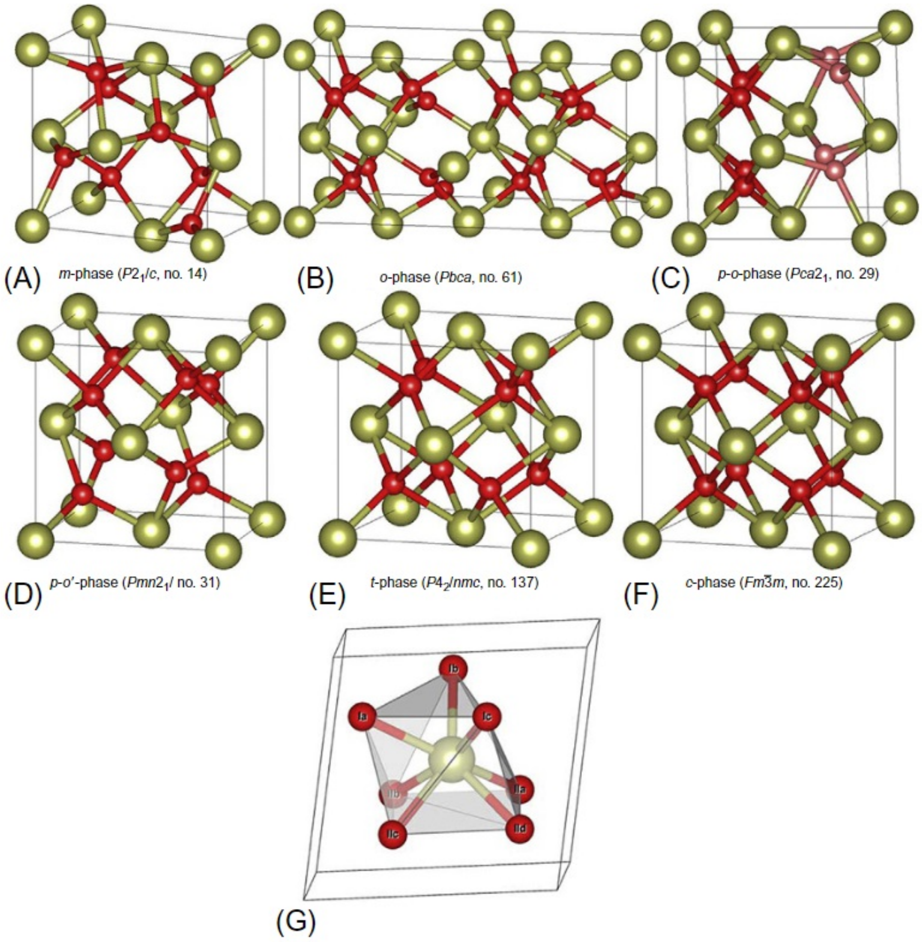

Figure 2.1: Six crystal structures of HfO_2 [8].

Other high-temperature and high-pressure polymorphs of HfO_2 have been identified in addition to the monoclinic crystal structure. The two high-temperature polymorphs are the tetragonal (P42/nmc) and cubic (Fm3m) phases [13]. It has been demonstrated that the phase transitions from monoclinic to tetragonal and from tetragonal to cubic occur at temperatures exceeding 1700°C and 2600°C, respectively [11]. A 3.4% increase in density is associated with the shift from the monoclinic to tetragonal phase [14]. an important characteristic of the monoclinic to tetragonal phase transformation is the shift in the Hf^{4+} CN from 7 (monoclinic) to 8 (tetragonal). The Zr^{4+} and O^{2-} bonds are said to be broken during this transformation in some earlier papers that explain the mechanism of this coordination change in the monoclinic to tetragonal phase transition in ZrO_2. The change to a nearest neighbor Zr^{4+} causes the triangularly coordinated O^{2-} (Ia, Ib, and Ic) in Fig. 2.1(G) to move, forming an eightfold coordination in the tetragonal structure [15, 16]. Under pressure, multiple phases of HfO_2 are shown to exist. With increasing pressure, the phase transition sequence is shown to be monoclinic, two different orthorhombic phases, then tetragonal and cubic. HfO_2 is monoclinic at room temperature, although different polymorphs can be stabilized thereby reducing particle size. At a threshold size of 30 nm, for instance, the tetragonal or cubic phases can be stabilized [11].

Dopants can be used to stabilize the tetragonal or cubic structures of HfO_2 at ambient temperatures. Differences in ionic radii (trivalent ions greater than Hf^{4+}) and valency (3+ relative to 4+ of Hf) have been linked to the stabilization of the cubic fluorite phase in trivalent-doped HfO_2. The larger ionic radii of the dopants require elongation of the M^{3+} bond with the O_2 ion [11]. When trivalent dopants substitute for Hf^{4+} it causes a charge deficiency. Oxygen vacancies are formed to make up for these deficits. In order to balance the charge, oxygen vacancies occur close to the cation, which lowers the local CN of the cation. The optimal CN of O_{2-} for Hf^{4+}, as was previously mentioned, is 8. The cubic or tetragonal HfO_2 phases can be stabilized because to this lowering of the CN of the Hf^{4+} [14].

While the phase of hafnia determines the main characteristics of the material, intrinsic defects have a significant impact on the resulting properties as well.

2.2 Intrinsic defects

While HfO_2 and ZrO_2 are used in this study interchangeably, this section will focus more on HfO_2 as that is the material represented in thesis 3 and 4, where the following information is applied more in detail than for thesis 1 and 2.

2.2.1 Theoretical studies

Like most materials, hafnia can contain defects that can significantly affect its performance. Intrinsic defects in hafnia, such as oxygen vacancies and hafnium interstitials, have been a topic of discussion for many years due to their impact on the electrical, optical, and mechanical properties of the material.

This chapter will therefore provide an overview of intrinsic defects in hafnia and their formation mechanisms, using theoretical calculations to evaluate the formation energies and energy levels of said defects.

Stable configurations of neutral oxygen vacancies and interstitial oxygen atoms and molecules in the bulk of hafnia were first considered by Foster et al. in 2002. The electron and hole affinities of these defects were calculated, and their stable configurations in various charge states were investigated. The findings showed that positively charged oxygen vacancies and interstitial oxygen atoms can trap electrons from the bottom of the hafnia conduction band and silicon. [17]

Electrons or holes tunneling from Si can charge defects in gate oxides. As a result, Foster et al. looked at the production and equilibrium structures of charged species $X{=}O^{-}$

and O^{2-} before moving on to the interstitial neutral oxygen atom. Each interstitial can produce a stable defect at a fourfold-coordinated tetragonally bonded lattice oxygen site or a threefold-coordinated trigonally bonded lattice oxygen site, as shown in Figure 2.2 All data associated with a threefold-coordinated oxygen will be labeled X_3 for convenience of reference, whereas all values associated with a fourfold-coordinated oxygen will be labeled X_4, where X is the faulty species.

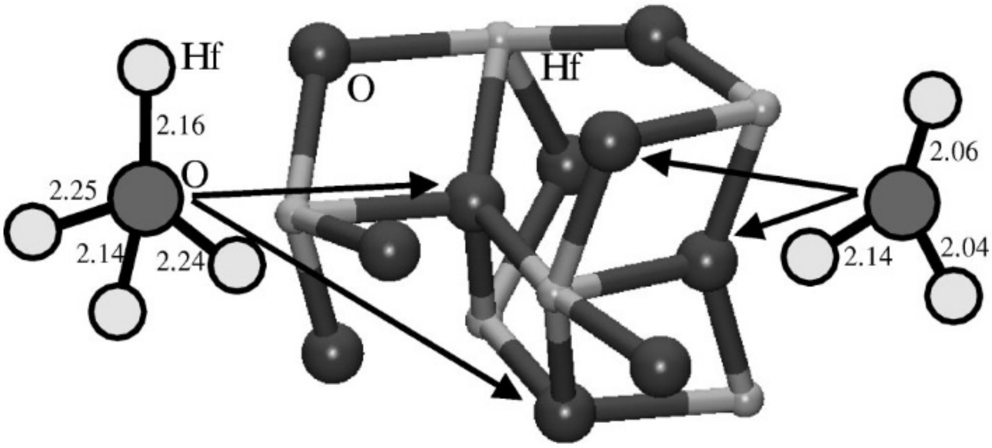

Figure 2.2: Diagram showing the fourfold-coordinated tetragonal (left) and threefold-coordinated trigonal (right) bonding of the oxygen ions in the monoclinic phase of hafnia as calculated in this work. The numbers show interatomic distances in Å. [17]

Formation energies for single O atom incorporation into the monoclinic hafnia lattice were found to be -1.3 eV (O_3^0) and -0.6 eV (O_4^0). Since calculations showed that the triclinic O_3^0 site is energetically favored, the rest of the discussion regarding the calculations of Foster et al. will focus mainly on this site. Note also that previous studies in zirconia have shown that there is no stable minimum for charged defects at the O_4 sites. [18]

The neutral interstitial creates a distinct covalent link with the threefold-coordinated lattice oxygen, as seen by a charge density map in Figure 2.3a. The interstitial and lattice oxygen form a "dumbbell" defect pair structure, which is also seen in other oxides, such as zirconia [18] and zircon ($ZrSiO_4$) [19]. The lattice oxygen displaces from its planar position between three Hf ions to form a shallow pyramid to accommodate the interstitial. Although small differences in bond lengths indicate slightly different environments, the two oxygens in this structure are effectively identical structurally and electronically, and the interstitial is connected to just two of the three hafnium ions in the pyramid. The interstitial incorporates in the lowest singlet state, but the triplet state is 0.9 eV higher in energy.[17]

An extra electron was added to the system in the atomic configuration of the neutral interstitial to explore electron trapping by the defect. System relaxation leads to the complete localization of the electron on the oxygen pair. The increased charge on the defect oxygen pair causes the ions to separate, also increasing the depth of the triple oxygen pyramid. Figure 2.3b shows that the covalent bond between the two has almost disappeared, despite the fact that they remain effectively the same species within the crystal. The relaxation energy of the O_3^0 structure in its initial state is 2.3 eV. The electron is fully localized in a doublet state on the defect pair.

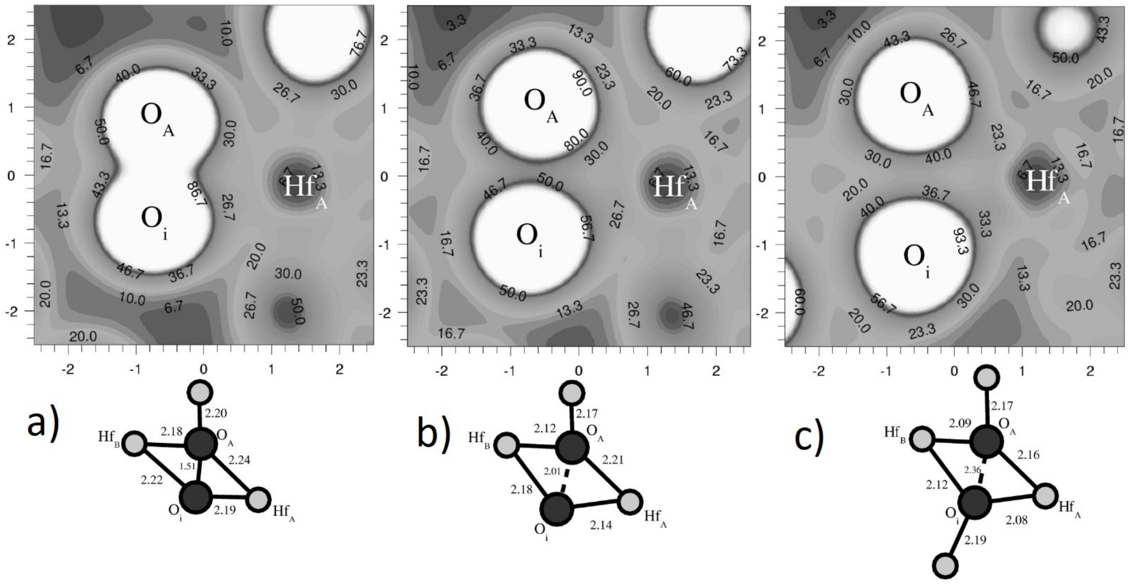

Figure 2.3: Charge density in the plane through Hf_A, O_A, and O_i, and a schematic diagram of neutral (a), singly charged (b) and doubly charged (c) oxygen interstitials (O_i) near a threefold-coordinated oxygen (O_A) in hafnia. The charge density is in $0.1e/\text{Å}^3$ and all distances are in Å [17]

.

The addition of a second electron from the conduction band to the negatively charged defect is accompanied by substantial lattice relaxation. The introduction of the second electron effectively produces two independent lattice oxygen ions. The separation between them increases even further, to about 2.4 Å. Figure 2.3c shows the lack of bond between the two oxygen ions. The corresponding relaxation energy is about 1.53 eV. The three Hf ions push the initial threefold-coordinated lattice oxygen into a deeper pyramid structure, while the interstitial now creates a new threefold-coordinated site at 2.2 Å, bonding with a third, independent hafnium ion. This hafnium ion was over 2.6 Å from the interstitial (and over 4 Å from the lattice oxygen) in the prior defect structures, and no bond could be found in the charge density. The new electron is fully localized on the defect oxygen pair, which is in the singlet state with equal spin components.

Molecular oxygen Molecular oxygen species may incorporate into the hafnia lattice from the gas phase or arise as a result of interactions with atomic oxygen species already located inside the lattice. It was found that incorporation in the threefold-coordinated lattice was more favorable due to allowing for more space.

The results showed that the molecule has a high electron affinity in the oxide, as a stable minimum could only be found with the molecule bonding to hafnium ions, meaning that it seeks the most abundant source of electrons in the system - lattice oxygen sites. Adding electrons into the molecular defect produced similar results to single oxygen atom incorporation. The molecule displaced away from the lattice oxygen and was effectively bonded only to Hf ions. The development of the oxygen molecule as an ionic species in the crystal continues with the addition of another electron.

Oxygen vacancies Growth, deposition, and doping processes can all result in vacancies in hafnia films and bulk samples. The obtained displacements of oxygen vacancies in monoclinic hafnia were in the range of 0.01 - 0.02 Å, which is similar to the displacement seen in zirconia [18]. Such small displacements are characteristic of the F-center type defects well studied in cubic ionic oxides, such as MgO [20]. They correlate to the two remaining electrons being firmly localized around the vacancy site, almost completely screening the anion vacancy. Removing an electron from the relaxed neutral vacancies results in the formation of the positively charged defects, VO_3^{1+} and VO_4^{1+} and yields a significantly larger outward displacement (0.1-0.2 Å) of hafnium atoms surrounding the vacancy site as part of the screening effect is lost. The results for the removal of another electron and the creation of doubly positively charged vacancies imply that once the electrons are removed, the threefold-coordination site is strongly favored and vacancies are likely to diffuse to these sites [17].

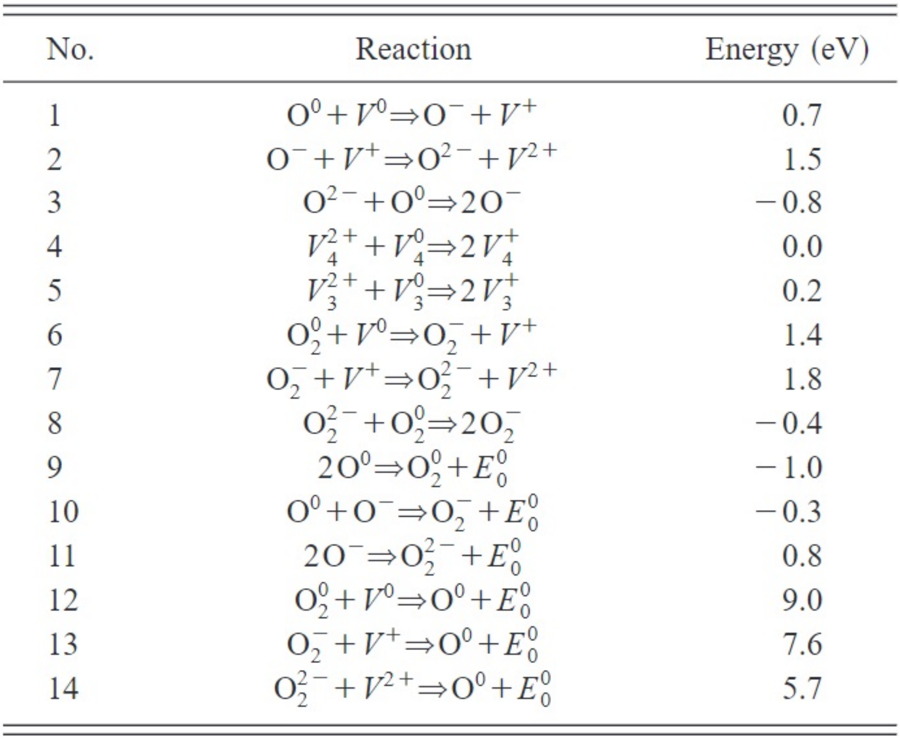

No.	Reaction	Energy (eV)
1	$O^0 + V^0 \Rightarrow O^- + V^+$	0.7
2	$O^- + V^+ \Rightarrow O^{2-} + V^{2+}$	1.5
3	$O^{2-} + O^0 \Rightarrow 2O^-$	−0.8
4	$V_4^{2+} + V_4^0 \Rightarrow 2V_4^+$	0.0
5	$V_3^{2+} + V_3^0 \Rightarrow 2V_3^+$	0.2
6	$O_2^0 + V^0 \Rightarrow O_2^- + V^+$	1.4
7	$O_2^- + V^+ \Rightarrow O_2^{2-} + V^{2+}$	1.8
8	$O_2^{2-} + O_2^0 \Rightarrow 2O_2^-$	−0.4
9	$2O^0 \Rightarrow O_2^0 + E_0^0$	−1.0
10	$O^0 + O^- \Rightarrow O_2^- + E_0^0$	−0.3
11	$2O^- \Rightarrow O_2^{2-} + E_0^0$	0.8
12	$O_2^0 + V^0 \Rightarrow O^0 + E_0^0$	9.0
13	$O_2^- + V^+ \Rightarrow O^0 + E_0^0$	7.6
14	$O_2^{2-} + V^{2+} \Rightarrow O^0 + E_0^0$	5.7

Figure 2.4: Defect reactions and associated energies [17].

Predictions by Foster et al. about defect reactions and their energies are show in Figure 2.4, however the reader should take into account that the results should be regarded to as more qualitative than quantitative due to not considering the chemical potential and Fermi level as controlling variables for defect formation energies. However, a significant characteristic is seen - the ”negative U” behaviour (which will later on be also discussed in works of Zheng et al.[21] and Chimata et al.[22]) of an oxygen ion in hafnia, i.e., that two isolated O^- species would decay into O^{2-} and O^0. The normal condition is a ”positive U”, in which electrons in a trap resist each other due to Coulombic potential. When there is a significant electron-lattice coupling, the ions relax as the defect charge state changes, resulting in a negative U [23]. This terminology was acquired from the Anderson’s model for semiconductors where this effect is much more common than in insulators [24].

In summary, the work of Foster showed that interstitial oxygen species and charged vacancies may serve as traps for electrons from the hafnia conduction band. The oxygen vacancies have structures and properties similar to those of F centers in cubic oxides (see also discussion in Ref. [20]). Another significant conclusion is that when electrons are available from the bottom of the hafnia conduction band, charged atomic and molecular oxygen species are more stable than neutral oxygen species.

In 2005 the calculations of Xiong et al. were published [23], using the screened exchange (sX) method [25] and the weighted density approximation (WDA) [26] to derive the energy levels. A sizable shift in the vacancy energy level was found, to a value much more consistent with experimental values [27].

The energy gap of bulk HfO_2 was calculated to be 5.5 eV, 5.95 eV and 5.75 eV for cubic, tetragonal and monoclinic respectively, which compares well to the 5.9 eV experimental value [27]. The oxygen interstitial and vacancy are denoted I and V respectively. The I^{2-} interstitial or O^{2-} is a closed shell system with energy levels that fall within the oxide valence band. The O^{2-} ion is separated from the other O^{2-} (bulk) ions by a large distance.

The I^- or O^- ion behaves in a similar fashion to O^{2-}. It is located about 2Å away from the other O^{2-} ions. Figure 2.5 shows the local DOS of the interstitials. It can be seen that the O^- ion gives rise to a half-filled state 1 eV above the valence band maximum.

A different behaviour is seen for I^0 and O^0. The two empty states allow it to form an O-O bond of length 1.49 Å to a bulk O^{2-} ion to form a superoxyl ion O_2^-. As a result, an empty antibonding $\sigma*$ state is created in the upper gap with a bonding partner at -5.5 eV in the valence band. O^+ ion also forms a bond with a O^{2-} ion with a shorter bond length of 1.39 Å, resulting in a O_2^- ion. The Fermi level is found right above the VB top in the * state. This type of O_2^- ion is called a superoxyl ion. It is paramagnetic and its characteristic signature has been observed by EPR in excited bulk HfO_2 by Kang [28].

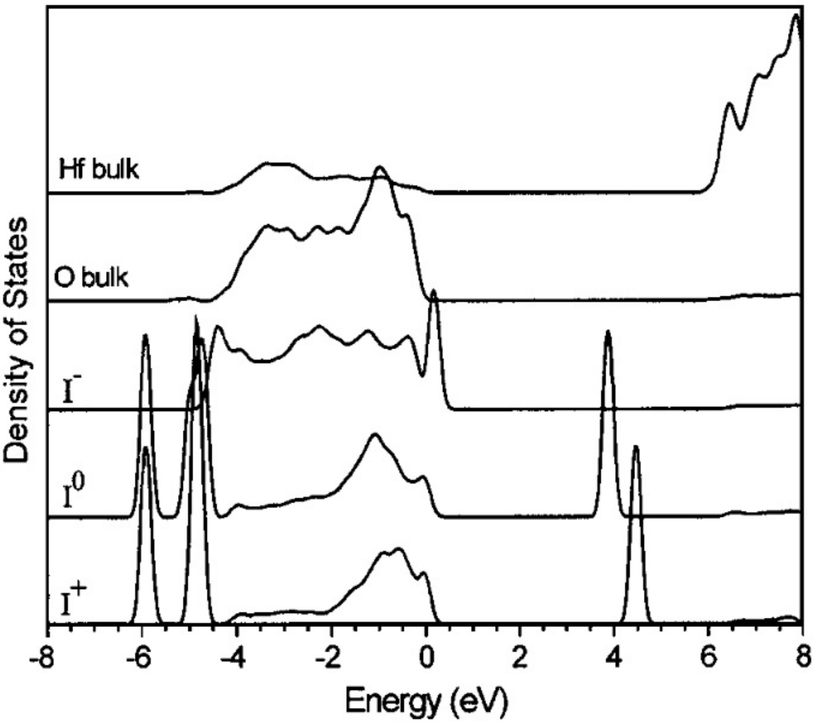

Figure 2.5: Calculated local density of states at the relaxed oxygen interstitial in its various charge states. [29]

When considering oxygen vacancies, we see that the O vacancy creates a single gap state of A_1 symmetry and is occupied by two electrons. The state is strongly localised on the d orbitals of the adjacent Hf ions. In cubic hafnia, the state is found at 3.8 eV above the VB edge. The relaxation of the ionic positions is minimal for the neutral vacancy. For the positive vacancy VO^{1+}, the positive charges cause a stronger relaxation of the adjacent Hf ions and the Hf-Hf separation is now 3.7 Å compared to 3.59 Å for the neutral vacancy VO^0. The state lies at 4.45 eV in c-HfO_2. The doubly charged vacancy causes an even greater displacement of the Hf ions, resulting in a Hf-f separation of 3.8 Å and gap state of 5.0 eV. Figure 2.6 shows the summary of the calculated energy levels of the relaxed O vacancy and interstitial at various charges.

The calculations of Xiong et al. place the vacancy levels much higher than Foster [17] and are more consistent with charge trapping data, indicating that the oxygen vacancy is the most common defect in HfO_2 gate oxide films. This suggests that electrons are responsible for conduction in HfO_2 films. HfO_2 to Si [30] has a substantially lower conduction band than the valence band offset, which favors electron injection. The electrons conduct through the film using Poole-Frenkel or trap-assisted tunneling [31]. As a result, the trap depth of $VO^{+}1$ is of the order of 1 eV below the oxide conduction band edge.

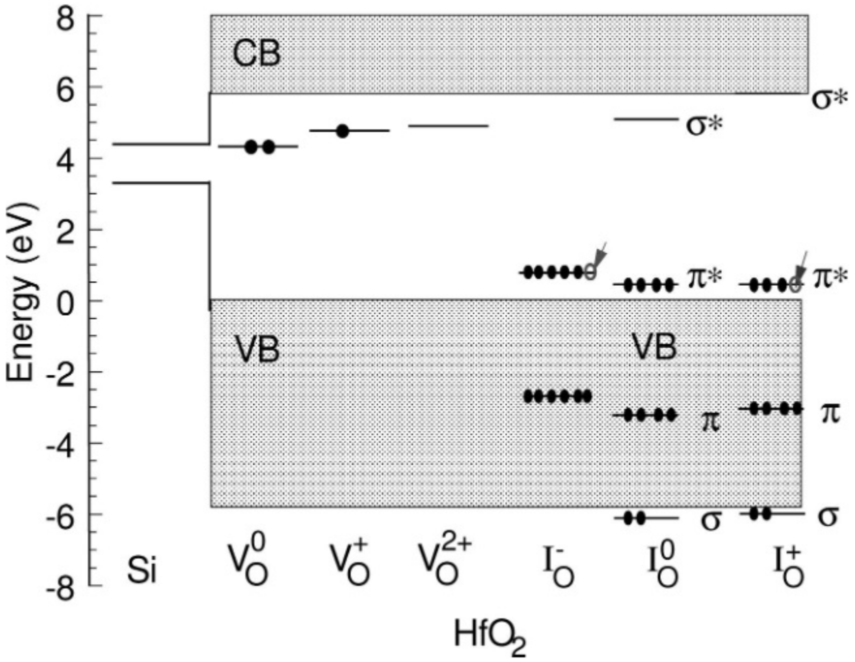

Figure 2.6: Energy levels of (a) the neutral, positive and double positive oxygen vacancy calculated by the sX method, (b) negative, neutral and positively charged O interstitial calculated by the WDA method, showing energy levels and electron occupancies. Partially filled states are arrowed. [23]

In 2007 Zheng et al. presented a paper [21] in which the authors give a detailed research of HfO_2 and ZrO_2 native point defects as a function of external chemical potentials and Fermi level, as these are the factors that can be influenced by doping and processing conditions. In this study, the monoclinic low-temperature phase hafnia was considered as it is typically present in the gate dielectric film [32, 33]. The calculated band gap for HfO_2

was 3.9 eV, which is smaller than the aforementioned experimental value of 5.9 eV [27]. As was also seen in the work of Foster, the underestimation of the band-gap energy value is typical of DFT calculations in the GGA approximation. Similarly, the stable neutral oxygen interstitial formed a dumbbell-shaped defect pair with a threefold-coordinated oxygen atom. Metal interstitials are most stable in 2c sites (at position (0 1/4 0) in a monoclinic unit cell), which are octahedrally coordinated by six oxygen atoms.

The formation energy of point defects in various charge states at the VBM (valence band maximum) ϵ_F=0 eV under extreme oxidation condition $\mu_O= \mu_O^0$ and extreme reducing condition $\mu_M=\mu_M^0$ are given in Table 2.1 without image charge corrections. Comparing the energy differences for oxygen point defects with the work of Foster et al. [17] for VO_3 and VO_4, it can be seen that HfO_2 and ZrO_2 are 0.50 and 0.48 eV, respectively, which are close to the values of 0.48 and 0.46 eV obtained by Foster. For O_i, the energy difference is 0.27 eV, comparable to 0.2 eV.

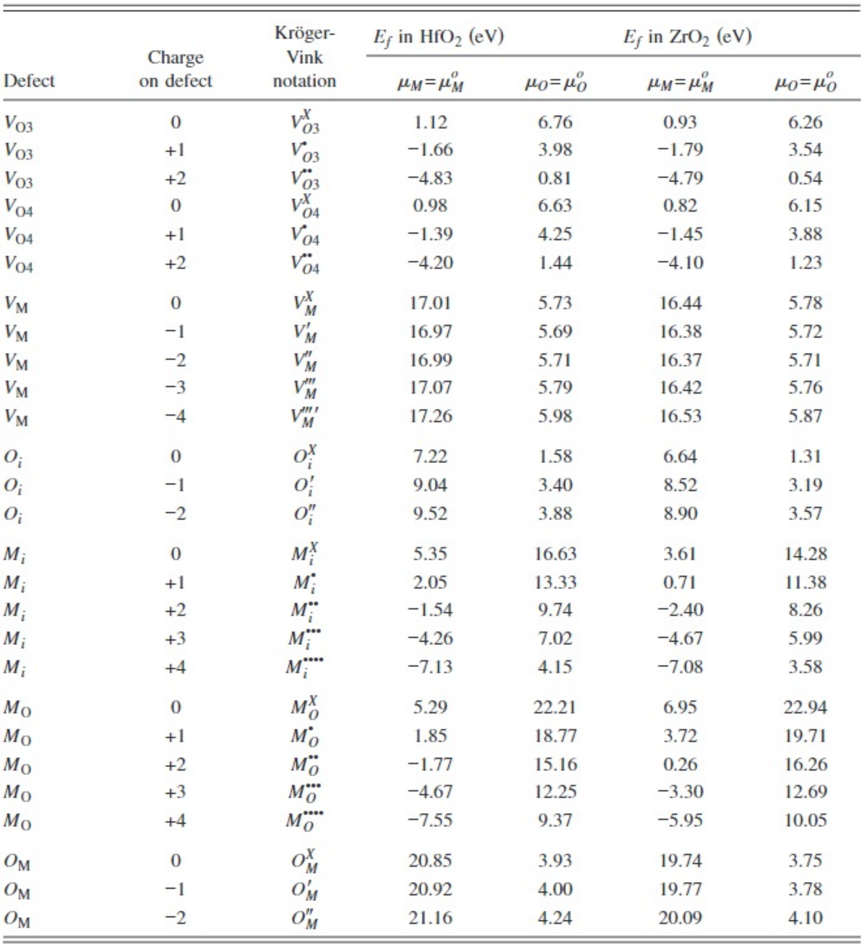

Defect	Charge on defect	Kröger-Vink notation	E_f in HfO_2 (eV)		E_f in ZrO_2 (eV)	
			$\mu_M=\mu_M^o$	$\mu_O=\mu_O^o$	$\mu_M=\mu_M^o$	$\mu_O=\mu_O^o$
V_{O3}	0	V_{O3}^{X}	1.12	6.76	0.93	6.26
V_{O3}	+1	$V_{O3}^{\bullet}$	−1.66	3.98	−1.79	3.54
V_{O3}	+2	$V_{O3}^{\bullet\bullet}$	−4.83	0.81	−4.79	0.54
V_{O4}	0	V_{O4}^{X}	0.98	6.63	0.82	6.15
V_{O4}	+1	$V_{O4}^{\bullet}$	−1.39	4.25	−1.45	3.88
V_{O4}	+2	$V_{O4}^{\bullet\bullet}$	−4.20	1.44	−4.10	1.23
V_M	0	V_M^{X}	17.01	5.73	16.44	5.78
V_M	−1	$V_M^{\prime}$	16.97	5.69	16.38	5.72
V_M	−2	$V_M^{\prime\prime}$	16.99	5.71	16.37	5.71
V_M	−3	$V_M^{\prime\prime\prime}$	17.07	5.79	16.42	5.76
V_M	−4	$V_M^{\prime\prime\prime\prime}$	17.26	5.98	16.53	5.87
O_i	0	O_i^{X}	7.22	1.58	6.64	1.31
O_i	−1	$O_i^{\prime}$	9.04	3.40	8.52	3.19
O_i	−2	$O_i^{\prime\prime}$	9.52	3.88	8.90	3.57
M_i	0	M_i^{X}	5.35	16.63	3.61	14.28
M_i	+1	$M_i^{\bullet}$	2.05	13.33	0.71	11.38
M_i	+2	$M_i^{\bullet\bullet}$	−1.54	9.74	−2.40	8.26
M_i	+3	$M_i^{\bullet\bullet\bullet}$	−4.26	7.02	−4.67	5.99
M_i	+4	$M_i^{\bullet\bullet\bullet\bullet}$	−7.13	4.15	−7.08	3.58
M_O	0	M_O^{X}	5.29	22.21	6.95	22.94
M_O	+1	$M_O^{\bullet}$	1.85	18.77	3.72	19.71
M_O	+2	$M_O^{\bullet\bullet}$	−1.77	15.16	0.26	16.26
M_O	+3	$M_O^{\bullet\bullet\bullet}$	−4.67	12.25	−3.30	12.69
M_O	+4	$M_O^{\bullet\bullet\bullet\bullet}$	−7.55	9.37	−5.95	10.05
O_M	0	O_M^{X}	20.85	3.93	19.74	3.75
O_M	−1	$O_M^{\prime}$	20.92	4.00	19.77	3.78
O_M	−2	$O_M^{\prime\prime}$	21.16	4.24	20.09	4.10

Table 2.1: Point defect formation energies (E_f) without image charge corrections in HfO_2 and ZrO_2 at $\mu_M= \mu_M^0$ (M=Hf,Zr) and $\mu_O= \mu_O^0$ at VBM (ϵ_F=0 eV). [21]

The formation energies for different defects in HfO_2 as a function of Fermi level for the two limiting values of the oxygen chemical potentials and one intermediate oxygen chemical potential are shown in Fig.2.7. The lower limit of the Fermi level (ϵ_F=0 eV) corresponds to the top of the valence band, while the upper limit ϵ_F=E_g represents the bottom of the experimental conduction band. The energy of a defect with a certain charge state is only displayed for the Fermi levels in which that charge state has the lowest energy. As a result, the slope of the lines in these figures correlates to the charge state of the defect, and changes in slope indicate a charge state transition. Vertical dashed lines represent the VBM of silicon, E_V(Si).

All stable defects result in oxygen deficit in HfO_2 at low oxygen partial pressure (and high hafnium partial pressure). When the Fermi level is near the VBM of HfO_2 (see Fig.2.7a), Hf_i is the dominating defect, whereas VO takes over as the Fermi level rises. The stability of the hafnium interstitial is reduced when the oxygen partial pressure increases, and it can no longer be stabilized even at low Fermi levels (Fig.2.7b). At low Fermi levels, however, VO remains stable. Hafnium vacancies are more likely to occur at higher Fermi levels. When the Fermi level is close to the VBM, VO and O_i dominate across a small range, and when the Fermi level is further away from the VBM, V_{Hf} dominates.

Additionally, when the Fermi level is near to the VBM and the oxygen partial pressure is very low, a hafnium antisite (Hf_O) can occur (Fig.2.7a). This can be explained as the lowest feasible value of μO in the oxide (which is depicted in Fig.2.7a) being lower in HfO_2 than, for example, in ZrO_2 (also examined in Zheng et al. [21]) due to the greater negative formation enthalpy of HfO_2.

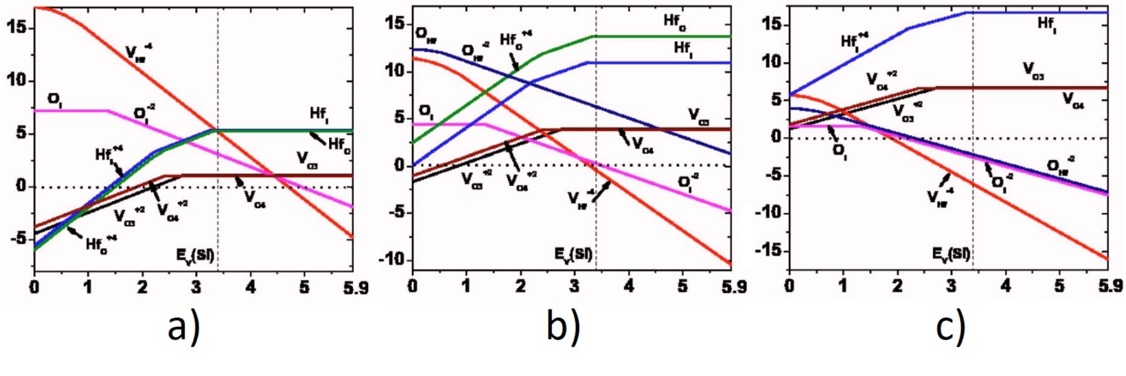

Figure 2.7: Calculated defect formation energy for native point defects in HfO_2 as a function of Fermi level and for (a) $\mu_O = \mu_O^o + \frac{1}{2}\Delta E_f^{MO_2}$ (low oxygen partial pressure and high metal partial pressure),(b) $\mu_O = \mu_O^o + \frac{1}{4}\Delta E_f^{MO_2}$ (intermediate oxygen and metal partial pressure), and (c) $\mu_O = \mu_O^o$ (high oxygen partial pressure and low metal partial pressure). The image charge corrections have been applied. The positions of the valence-band maximum of the silicon (E_V(Si)) are marked by vertical dashed lines. [21]

Zheng's study confirms oxygen interstitials having a "negative-U" characteristic, where O_i^- is unstable versus O_i and O_i^{2-}. Because an oxygen interstitial adds three 2p states and four 2p electrons to the top of the valence band, the defect levels caused by oxygen interstitials have valence-band characteristics, and the formation energy for oxygen interstitials is unlikely to be significantly influenced by the band gap underestimation. The negative-U behavior for oxygen interstitials is consistent with studies by Foster and co-workers [17, 18].

Oxygen vacancies also exhibit ”negative-U” behavior, i.e., VO^{1+} is not stable against disproportionation into VO^0 and VO^{2+}, although their behavior cannot be predicted with any precision because of the underestimated band gap.

Many of the defect formation energies in Fig.2.7 are negative. Some of the negative values towards the extremes of oxygen chemical potential could indicate that these chemical potentials are not truly achievable. It is probable that suboxides will form before reduction to the metal occurs at the low end of the oxygen chemical potential, limiting the lower oxygen potential that may be obtained in HfO_2. On the high oxidation side, the underestimation of the O_2 binding energy [34] allows for an excessively high oxygen chemical potential, resulting in a significant tendency to generate metal vacancies. Negative formation energies at intermediate chemical potentials of oxygen, on the other hand, cannot be attributable to these difficulties and may reflect a true material instability at specific Fermi level values.

Finally, we examine the work of Chimata et al., where defect energetics of cubic hafnia are studied using quantum Monte Carlo simluations [22].

Calculations by Chimata et al. show that adjacent Hf ions were relaxed towards the vacancy position by a displacement of 0.02 Å from their ideal positions. The electronic configuration around the vacancy site drives the relaxation of Hf atoms: taking one oxygen atom out of a perfect cubic hafnia crystal leaves two extra electrons, with each Hf dangling bond contributing 1/2 electron in its 5d shell. By gradually compressing the Hf atoms towards the vacancy site, the total energy of the system is reduced. The nearby Hf ions relax 0.084 and 0.180 Å, respectively, outward from the vacancy site in the positively charged defect states VO^{1+} and VO^{2+}, which is consistent with the observations in Ref. [29].

In contrast, the Hf ions relax inwards by around 0.03 and 0.13 Å, respectively, for negatively charged defects VO^{1-} and VO^{2-} O, which are created by adding one and two electrons to the neutral vacancy.

Additionally, the reported formation energy for a neutral oxygen vacancy is lower than the 6.95 eV derived from GGA calculations for cubic HfO_2 [35]. When compared to neutral oxygen vacancies, the GGA+U and DMC formation energies for VO^{1-} and VO^{2-} states are greater, indicating that these vacancies are more unstable. As a result, we will not go into detail about these charged defect states. Under oxygen-rich and oxygen-poor conditions, the GGA+U and DMC formation energies for VO^{1+} and VO^{2+} are both lower than the formation energy of neutral oxygen vacancy, indicating that both of these states are more stable than neutral and negatively charged oxygen vacancies.

An effective U parameter was derived (which is different from the Hubbard U in GGA+U) to comprehend the disproportion of -2, -1, 0, +1, and +2 charge oxygen vacancies in hafnia. The physical meaning of the U parameter is that it represents the quantitative repulsive electrostatic interaction (U_{el}) between ionic defects and the electron-lattice relaxation energy (U_{rel}), $U' = U_{el} + U_{rel}$ [36]. It is evaluated in three scenarios as discussed in Ref [37].

(1) Injecting an electron into hafnia, $2VO^{1-} \rightarrow VO^{0} + VO^{2-}$: When an electron is injected into hafnia, it is trapped in a neutral vacancy state, which becomes VO^{1-}, and adding another electron to a VO^{1-} state forms a VO^{2-} defect.

(2) Injecting a hole into hafnia $2VO^{1+} \rightarrow VO^{0} + VO^{2+}$: When a hole is injected into hafnia, it is trapped by a neutral vacancy, which turns into a VO^{1+} vacancy. A VO^{2+} state is generated by adding a hole to the VO^{1+} state.

(3) Neutral defect creation in hafnia, $VO^{2-} + VO^{2+} \rightarrow VO^{0}$: This is accomplished by de-trapping charges from the charged vacancies.

In all three cases, a negative U' is obtained for both GGA+U and DMC.

Figure 2.8 shows the GGA+U total electron density of states (DOS) and orbital-projected density of states (PDOS) for pure, VO^{0}, and VO^{2+} charge oxygen vacancies in hafnia.

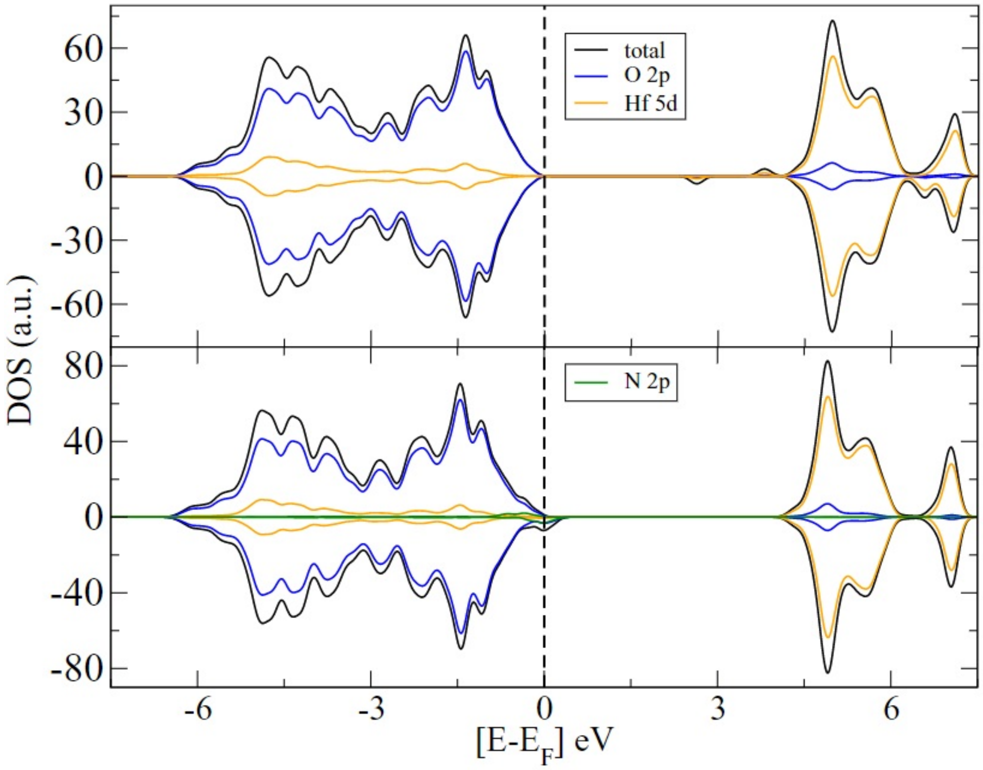

Figure 2.8: Total density of states for hafnia with a VO^{1+} defect state(top) and N substitutional defect (bottom). The magnetism in the N-doped system is mainly due to the N 2*p* at the Fermi level, while in the VO^{1+} is due to the Hf 5*d* states. [22]

The GGA+U band gap for hafnia was calculated to be 4.04 eV, which is lower than the experimental measurement of 5.8 eV [38]. The oxygen 2*p* states dominate the top of the valence band, whereas the hafnia 5*d* states contribute to the bottom of the conduction band, as can be seen by the PDOS. A defect state forms in the middle of the gap for a neutral oxygen vacancy. The defect state is strongly localized on the nearby Hf ion 5*d* orbitals and 2*p*, respectively. The band gap is effectively reduced to roughly 2.0 eV when the defect state is mid-gap. The band gap is lowered to 3.9 eV for the VO^{2+} charge state, and the gap contains no defect states.

Chimata also investigates the effects of nitrogen substitutional doping at an oxygen site in the supercell and as a result a substitutional N defect with a defect concentration of 1.04% was created. The positive charge (one hole) at the N site causes a slight inward relaxation of the adjacent hafnium shell, as well as an outward relaxation of nearby oxygen atoms. It was also discovered that a spin-polarized structure with a total magnetic moment of 1.0 μ_B B is more stable than an un-polarized one. The overall moment is primarily residing in the single 2*p* hole generated by the N dopant; N has a magnetic moment of 0.4 μ_B, while the nearby Hf atoms and second-NN O attain induced ferromagnetic moments of 0.0012 μ_B and 0.0486 μ_B, respectively.

A considerable hybridization between the N 2*p* and O 2*p* states at the Fermi level, E_F was observed. The hybridization causes the energy levels near E_F to separate. The spin-split states near E_F give rise to a ferromagnetic insulator with a 3.6 eV band gap. This band gap is similar to that of pure cubic hafnia, implying that leakage currents can be lowered by nitrogen doping, such as annealing in a nitrogen-rich environment to eliminate oxygen vacancies and their mid-gap states. According to previous first-principles calculations [29, 39], the inclusion of two N atoms near to the oxygen vacancy sites shifts the vacancy level out of the gap, which agrees with the results of Chimata [22]. The findings show that replacing a single nitrogen atom at the oxygen vacancy site eliminates the single defect level caused by the neutral oxygen vacancy, lowering leakage currents. However, the excess charge at the N-dopant site still causes a fixed-charge problem, which may be resolved by adding another N atom to the supercell. Table 2.9 shows the calculated DMC and DFT formation energies for various oxygen vacancy charge states and a neutral N dopant.

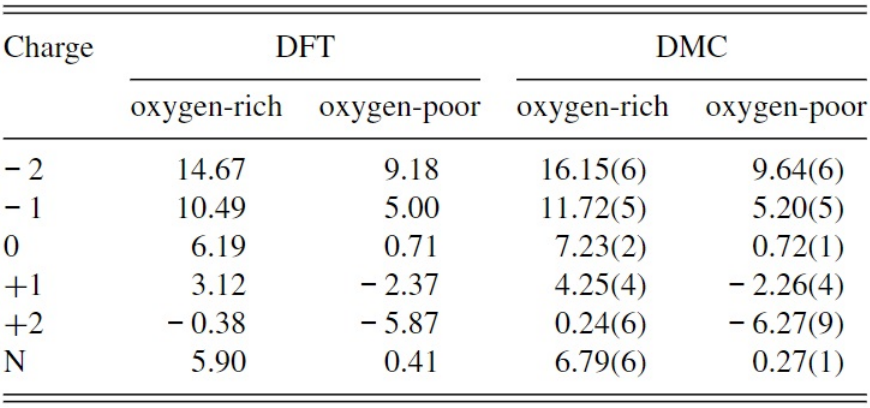

Charge	DFT		DMC	
	oxygen-rich	oxygen-poor	oxygen-rich	oxygen-poor
− 2	14.67	9.18	16.15(6)	9.64(6)
− 1	10.49	5.00	11.72(5)	5.20(5)
0	6.19	0.71	7.23(2)	0.72(1)
+1	3.12	− 2.37	4.25(4)	− 2.26(4)
+2	− 0.38	− 5.87	0.24(6)	− 6.27(9)
N	5.90	0.41	6.79(6)	0.27(1)

Figure 2.9: Defect formation energies in eV for different oxygen vacancy charge states and for a neutral substitutional N defect. [22]

Under oxygen-rich conditions, DMC values are often 0.6–1.5 eV higher than the equivalent GGA+U formation energies. The disparities between the DMC and GGA+U energies are attributed to the differing descriptions of the 5d orbitals and the correlation energy, similar to defects observed in 3d transition metal oxides: GGA+U typically underestimates the formation energies and band gap [40, 41].

In summary, the calculations showed that in oxygen-poor conditions, a substitutional N dopant has a substantially lower formation energy than a neutral oxygen vacancy. Furthermore, the N dopant does not effectively lower the band gap as it does not introduce mid-gap states. These findings support previous observations that nitrogen can passivate HfO_2 [42]. Additionally, the N dopant induces a ferromagnetic state of around 0.4B per nitrogen. Under oxygen-poor conditions, the positively charged oxygen defects VO^{1+} and VO^{2+} have negative formation energies, indicating that they will form spontaneously. However, stability analysis show that VO^{1+} is unstable in terms of neutral vacancies and VO^{2+} creation, while the neutral vacancy VO^0 is stable in terms of VO^{2+} and VO^{2-} formation. Such defects are expected to emerge because the production energies of VO^{2+} and VO^{1+} are negative in oxygen-poor conditions. Therefore, to avoid the production of charged oxygen vacancies, it is necessary to prevent charging (allowing electrons to escape) during cubic hafnia formation; neutral defects can be eliminated by nitrogen passivation.

In conclusion, the work of Foster showed that interstitial oxygen species and charged vacancies may serve as traps for electrons from the hafnia conduction band. Oxygen vacancies also exhibited ”negative-U” behavior, i.e., VO^{1+} was not stable against disproportionation into VO^0 and VO^{2+}, although their behavior could not be predicted with any precision due to the underestimated band gap.

The calculations of Xiong et al. placed the vacancy levels much higher than Foster [17] and were more consistent with charge trapping data, indicating that the oxygen vacancy was the most common defect in HfO_2 gate oxide films.

The work of Zheng confirmed oxygen interstitials having a ”negative-U” characteristic that was consistent with studies by Foster. Because an oxygen interstitial adds three 2p states and four 2p electrons to the top of the valence band, the defect levels caused by oxygen interstitials had valence-band characteristics, and the formation energy for oxygen interstitials was unlikely to be significantly influenced by the band gap underestimation in the work of Foster.

Additionally, Chimata further showed that under oxygen-poor conditions, the positively charged oxygen defects VO^{1+} and VO^{2+} have negative formation energies, indicating that they will form spontaneously.

While theoretical studies offered significant information on the potential mechanisms of defect formation and their properties, experimental studies provide additional valuable insights and confirmations.

2.2.2 Experimental studies

In this chapter the author examines the experimental data to complement the theoretical studies, thereby furthering the understanding of defects in hafnia.

One of the first experimental studies on defects in bulk hafnia powders was performed by Kiisk et al.[43] where photoluminescence properties of pure hafnia prepared by using the sol-gel method were characterized.

Kiisk reports all samples being monoclinic after annealing at 1000°C. Apparent crystallite sizes were found to be 29 ± 3 nm. At low temperatures, excitation of the samples with a photon energy of 5.7 eV (exceeding band-gap of monoclinic hafnia) led to an emission spectrum consisting of two distinct emission bands around 2.4 eV and 4.0 eV (Fig. 2.10). The fundamental absorption of hafnia and the excitation spectra of the latter band are well-correlated. The 2.4 eV emission band, however, has a much more pronounced excitation band centered at 4.2 eV. At around 200K, the 4.0 eV emission band was rapidly quenched, while the 2.4 eV emission band showed no significant quenching even at room temperatures. The emission characteristics of the bulk hafnia slightly differ from previously reported data on thin films, with the 4.0 eV band being located at 4.3 eV instead, however overall behaviour is similar.

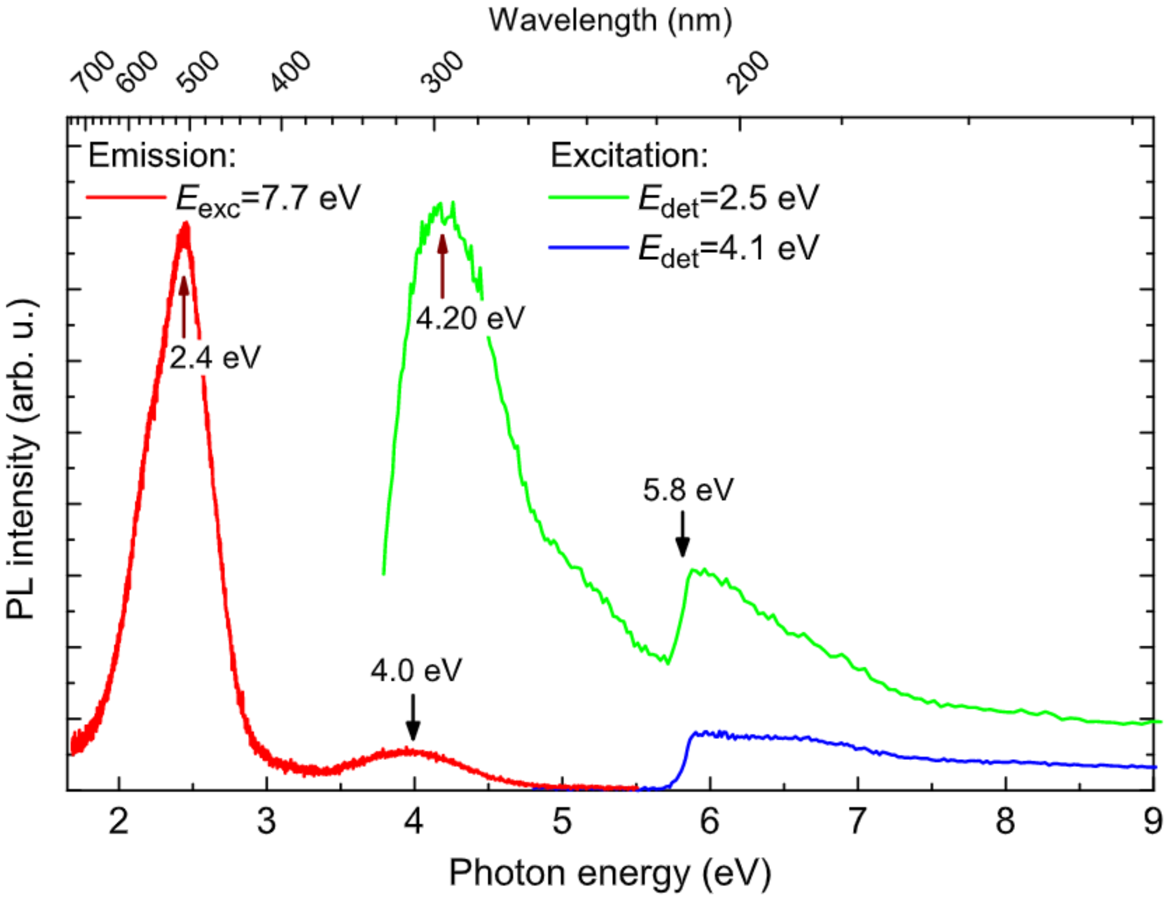

Figure 2.10: Emission and excitation spectra of HfO_2 at 10K using steady state excitation. [43]

A steady increase (about 2–3 times) of the 2.4eV emission band (excited into the 4.2 eV band) was observed with annealing temperatures being increased from 600°C to 1000°C. The increase is explained by the elimination of non-radiative relaxation pathways, as supported by lengthening of decay curves (Fig. 4.29). The decay kinetics of the 2.4eV emission band are non-exponential and expose a power-law tail characteristics at higher temperatures.

The unusual shape and temperature dependency of the 2.4eV luminescence decay kinetics suggests that the 4.2eV excitation band is caused by charge carrier delocalization and subsequent thermally accelerated migration to the luminescence center, rather than an intra-center transition. Such delocalization would be likely to occur in the case of a charge transfer process (from a localized state to the conduction band or from the valence band to a localized level).

The decay kinetics are particularly long-lasting below 100K and do not significantly vary with temperature. As a result, recombination is not thermally stimulated in this range. A probable mechanism for the low temperature range could be tunneling recombination. Above 100K, the decay kinetics grow progressively shorter and have a higher initial intensity.

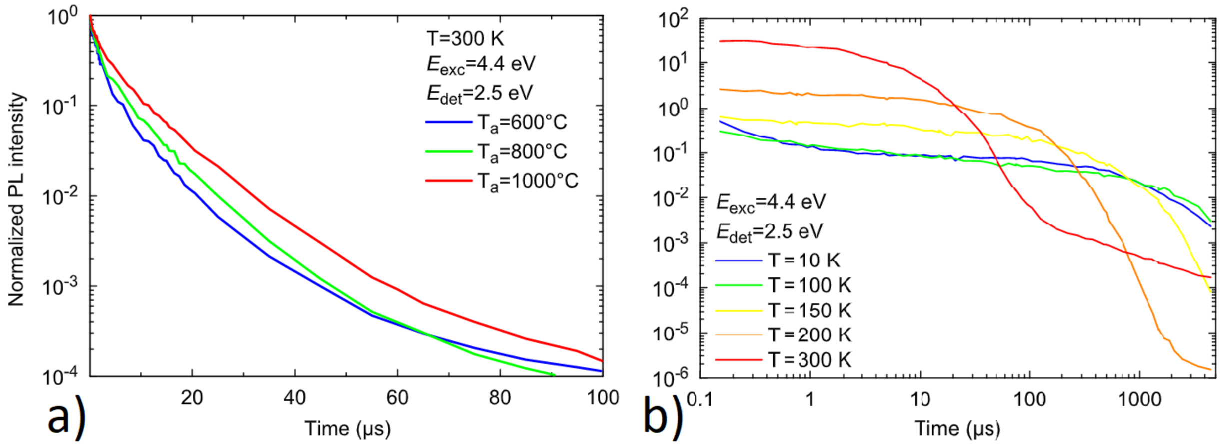

Figure 2.11: a) The room-temperature decay kinetics of the 2.4 eV emission band independence on the annealing temperature of sample and b) temperature dependence of the decay kinetics of the 2.4 eV emission band (for 1000°C annealed sample). Log–log scale is used to emphasize the tail of the decay curve. [43]

The theoretical calculations of Foster et al. [17] and Munoz Ramo et al. [44] predicted optical transitions of an electron from valence band to singly ionized vacancy (at 4.67 eV) and doubly ionized vacancy (at 4.91 eV) with the presence of ionized vacancies (with electron transfer to oxygen interstitials) being energetically favorable. Kiisk therefore proposes the excitation band at 4.2 eV being related to charge transfer transitions from valence band to singly or doubly ionized oxygen vacancies. A similar case is also found in yttrium-stabilized zirconia, where the recombination of a hole in the valence band with an electron trapped at the oxygen vacancy promotes the vacancy into an excited state, resulting in a 2.4 eV emission [45].

In 2016. Gritsenko et al.[46] published a paper summarizing the work of previous colleagues [47, 48] as well as studying the atomic structure of defects responsible for the 5.2 eV absorption and 2.7 eV luminescence, as well as charge transport mechanisms in HfO_2.

Hafnium oxide crystals grown by directional crystallization of the melt in a water-cooled crucible were used for thermoluminescence studies, while hafnia films obtained by ALD were used for photoluminescence and charge transport measurements. To produce oxygen vacancies, the HfO_2 crystals were annealed in a 10-4 vacuum medium at 1600°C and 2100°C.

Figure 2.12 shows the X-ray luminescence spectra of bulk HfO_2 crystals before and after annealing at 1600°C and 2100°C. Two broad luminescence bands at 2.6 and 4.4 eV are seen. The peak intensity of the luminescence at 2.7 eV increases dramatically after annealing at 1600°C. It is explained by increasing the concentration of radiative centers (oxygen vacancies).

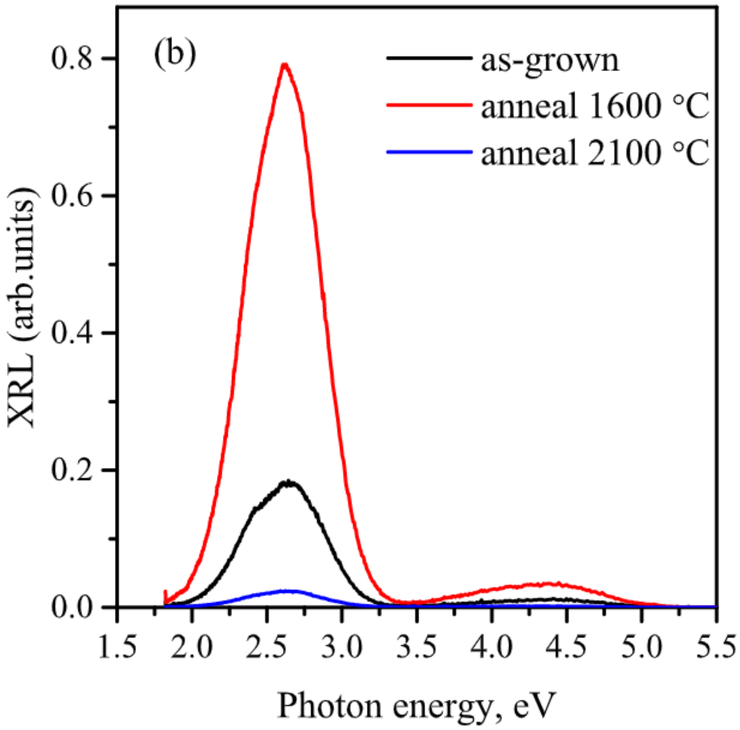

Figure 2.12: XRL spectra of pure bulk HfO_2 before (black) and after annealing at 1600°C (red) and at 2100°C(blue). [46]

Annealing at 2100°C, however, reduces the RL intensity significantly. The considerable increase in oxygen vacancies concentration accounts for this result. When the defect concentration exceeds a threshold point, the luminescence intensity drops as the concentration of radiative centers increases leading to concentration quenching. The effect is caused by non radiative energy loss during resonant excitation transfer from one center to another [49]. The band at 4.4 eV, observed in both single crystal and film hafnia, is interpreted as self-trapped exciton luminescence.

Figure 2.13 shows PL, PLE and simulated absorption spectra for almost stochiometric $HfO_{x\leq 2}$ and nonstochiometric $HfO_{1.83}$. An optical absorption peak near 5.2 eV was observed in [50, 51] and [52]. The oxygen vacancy in HfO_2 has an absorption peak around 5.3 eV, according to quantum-chemical simulations. The predicted oxygen vacancy absorption peak is similar to a PLE characteristic for 2.7 eV emission. This suggests that photons with a wavelength of 5.2 eV excite oxygen vacancies in HfO_2. A PL emission near 2.7 eV, on the other hand, shows the presence of oxygen vacancies in the bulk HfO_2 [46].

The optical transitions in the oxygen vacancy in HfO_2 and luminescence processes were described in a configuration diagram in the single-band model (Fig.2.13). The absorption of the 5.2 eV photons (vertical up arrow) results in a ground-to-excited state electron transition. After the transition, the vacancy becomes capable of generating photons. It can be concluded, that the 5.2 eV bands of absorption and PLE spectra correspond to the same transition. The vacancy then relaxes non-radiatively when the electron transitions to a minimum of the excited state. With the emission of the 2.7 eV photon, the electron returns to the ground state (vertical down arrow), and the system relaxes to the ground state minimum (starting point). The thermal activation energy W_t of the trap-capturing charge carriers corresponds to the polaron energy of 1.25 eV and the transition with energy $W_{opt}=2W_t=2.5$ eV corresponds to its optical activation energy. Given the foregoing, one can deduce that oxygen vacancies are responsible for the blue intrinsic defect luminescence of bulk HfO_2 [46].

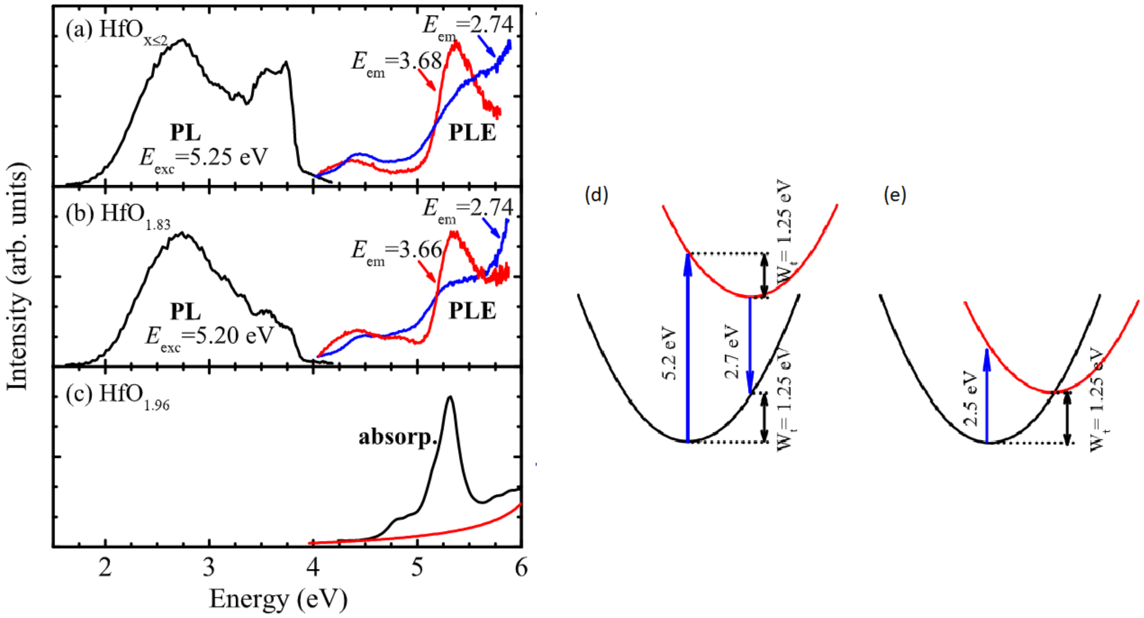

Figure 2.13: 1. (a) PL spectra measured at excitation by quantum energy 5.25 eV (black), and the PLE spectra of the 2.74 eV (blue) and 3.66 eV (red) emission band for almost stoichiometric hafnia $HfO_{x\leq2}$. (b) PL spectra at energy 5.25 eV, and the PLE spectra of the 2.74 eV (blue) and 3.66 eV (red) emission band for nonstoichiometric hafnia $HfO_{1.83}$. (c) The simulated optical absorption spectra for c-HfO_2 with the oxygen vacancy (black curve) and for perfect c-HfO_2 (red curve), (d) A configuration energy diagram for an oxygen vacancy in hafnia. (e) Absorption and luminescence in a neutral vacancy (black and red lines show the ground occupied and unoccupied excited states, respectively). [46]

The polaron energy calculated from the Stokes shift in PL/PLE spectra and the thermal activation energy of the trap reported from charge transport experiments are similar, indicating that oxygen vacancies in HfO_2 behave as traps.

To describe charge transport experiments quantitatively, simulations in terms of the phonon-assisted tunneling between traps were performed [53]. A multiparametric fitting procedure was used to get the values of different transport parameters and good agreement with previous studies was seen.

Thermoluminescence (TL) measurements were performed and the TL peaks were described by the following equation [54]

$$I(T) = n_0 vexp\left(\frac{W_t}{kT}\right) exp\left[-\frac{v}{\beta}\int_{T_0}^{T}\frac{dT'}{exp\left(\frac{W_t}{kT'}\right)}\right] \quad (2.1)$$

where n_0 is the initial concentration of trapped electrons, β is the rate of linear heating (K/s), and T_0 is the initial temperature. The obtained thermoluminescence curve is presented in Figure 2.14. A fixed value of the frequency factor (2x10^{15} s^{-1}), obtained for the oxygen vacancy in charge transport experiments, was used. The inset of Fig. 2.14 presents the thermal activation energies Wt corresponding to glow peaks.

The thermal activation energy for the peak near 372 K is 1.25 eV. This value is half of the Stokes shift and corresponds to the thermal activation energy W_t= 1.25 eV, as measured in the charge transport studies. It can be concluded, that the peak around 372K is caused by an oxygen vacancy. Gritsenko further suggests that the thermoluminescence peaks at temperatures 255, 291, and 315 K are caused by oxygen polyvacancies in HfO_2 based on similarities with other studies [55, 56].

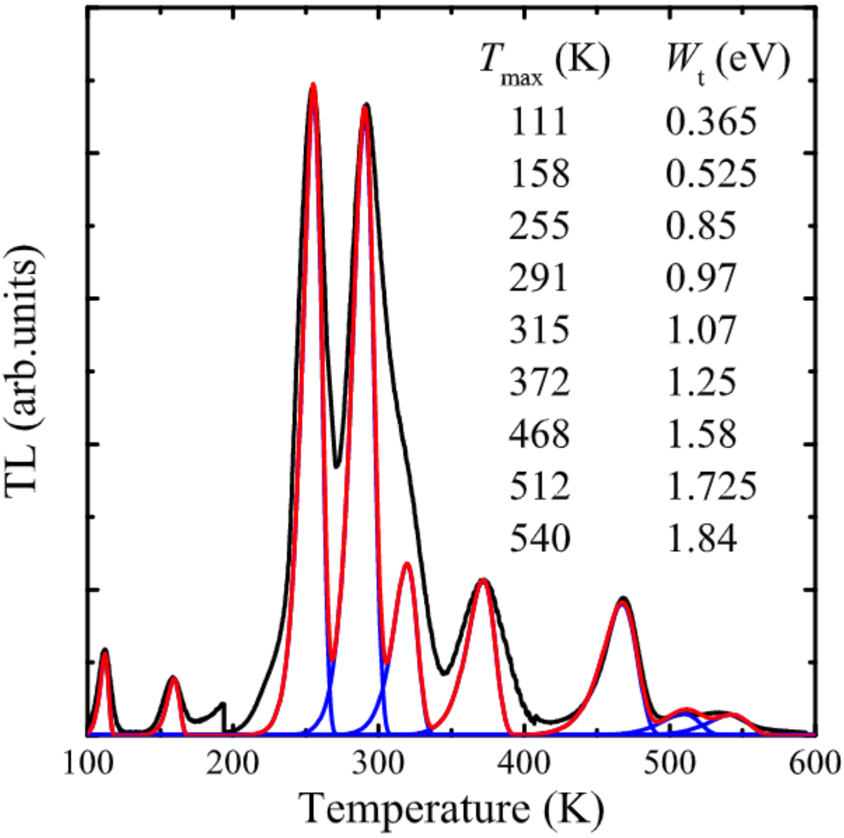

Figure 2.14: The experimentally obtained TL curve for HfO_2 annealed at 1600°C (thick blackcurve), and the deconvolution curves: the thin blue curves show individual peaks and the red line is their sum. The inset: each TL peak there corresponds to a value of W_t.). [46]

Complementing the theoretical studies, there has also been interest in nitrogen incorporation into hafnium oxide as adding N could markedly improve the resulting characteristics of hafnia - the highly electronegative nature of the *d*-state electrons in undoped hafnia makes it easy to crystallize and result in a large number of oxygen vacancies and a high bulk oxide trap density.

Sen et al.[57] explores the effects of nitrogen doping of hafnia by using electrical and XPS measurements. Plasma immersion ion implantation was used to add nitrogen atoms into an as-deposited hafnium oxide in order to achieve low implantation energy and small penetration depth which is paramount in very low physical thickness dielectrics.

The resulting amount of nitrogen incorporation was very low - around 5%. It is explained by very few replacements of O by N, due to the Hf–O bond being stronger than the Hf–N bond. Replacement would still occur at some disordered sites, such as the neighbours of oxygen vacancies. The phenomenon is similar to the case of N_2O or NH_3 nitridation of SiO_2 [58]. However, unlike the nitridation of SiO_2, in HfO_2 the nitrogen incorporation is uniform throughout the sample with no significant lowering of N concentration in the bulk. This observation can be explained by the uniform distribution of oxygen vacancies in the HfO_2 samples.

Figure 2.15 shows the Hf 4*f* XPS spectra obtained in the bulk of the sample implanted with nitrogen at a dose level of $10^{16}/\text{cm}^2$. The main peaks at 18 eV and 20 eV are attributed to Hf–O bonding with Hf $4f_{7/2}$ and Hf $4f_{5/2}$, respectively. Both peaks show significant (around 0.5eV) high-energy changes when compared to samples without nitrogen implantation. The Hf–N bonding is thought to be responsible for the double peak with binding energies of 15 and 16.7 eV.

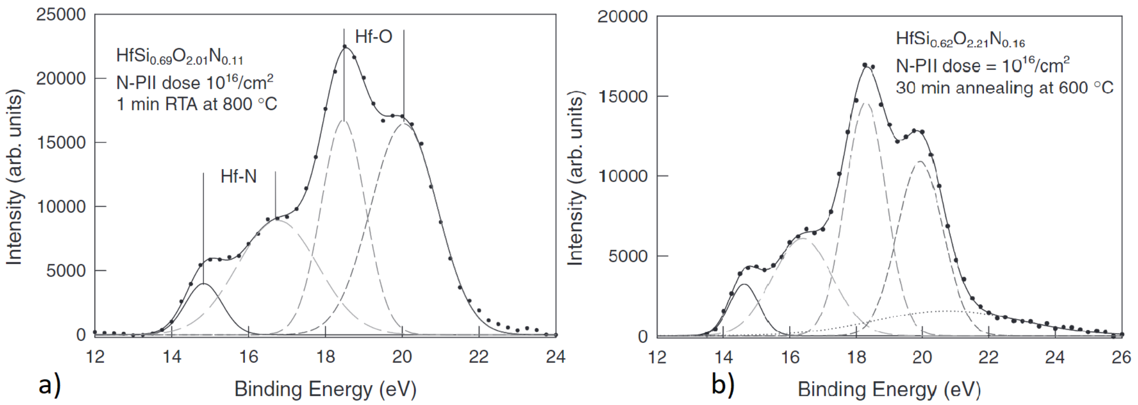

Figure 2.15: Gaussian deconvolution of Hf 4*f* core level XPS in bulk for nitrogen-implanted samples prepared under different annealing conditions: a) rapid thermal annealing at 800°C for 1 min, and b) furnace annealing at 600°C for 30 min. The nitrogen dose was $10^{16}/\text{cm}^2$.). [57]

The Hf–N bonding is fourfold coordinated, which helps to reduce the average atomic coordination number, and hence the defect level in HfO_xN_y. It is noted that the sample annealed at 600°C has a peak with an energy of roughly 21 eV. The peak is attributed to O 2*s*. This indicates that N-PII causes oxygen displacements. From an energy standpoint, the oxygen sites near the O-vacancies can be replaced by nitrogen atoms. The oxygen atoms that are released create interstitial oxygen, exhibiting the O 2*s* spectrum.

Although the amount of nitrogen incorporated into the lattice is minimal, the material and electrical properties show significant improvements. The temperature-dependent C–V characteristics of HfO_2 samples with and without nitrogen implantation are shown in Figure 2.16.

The samples without N-PII had a larger shift in the C–V curves and a smooth transition between the depletion and accumulation regions, indicating that the bulk trap and interface trap densities are quite high. The large bulk trap density is caused by O-vacancies and grain boundary states [59].

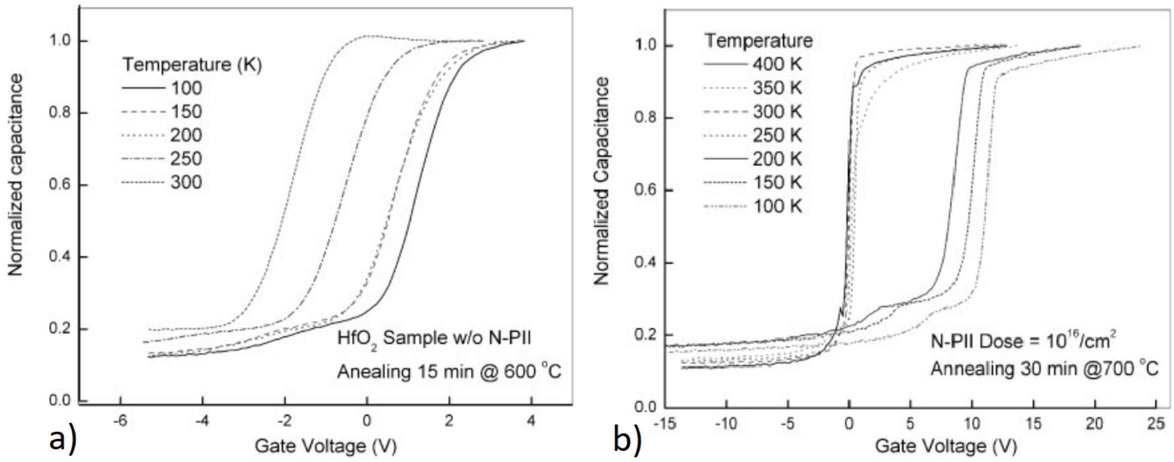

Figure 2.16: a) C–V characteristics of hafnium oxide and b) hafnium oxide with nitrogen implantation. [57]

As demonstrated by the small flat band shift and steep slope in the transition region of the C–V curves, the nitrogen-implanted sample has considerable reductions in both bulk trap and interface trap levels over a wide energy range. After incorporating nitrogen, the bulk trap is essentially removed due to the reduction of VO centers. The large drop in interface trap density is the combined result of numerous improvements at the interface.

Although the literature presented a large variety of data on luminescence for doped HfO_2 films [60–62], the nominally pure structures remained largely unexplored with the aforementioned studies providing information on the 2.7 eV intense blue luminescence, but lacking insight into the 4.0 - 4.5 eV emission band. Shilov et al. therefore provides an elaborate examination of the behaviour of the self-trapped exciton photoluminescence and estimates approximate fundamental parameters of the exciton-phonon interaction [63].

Shilov et al. examined crystalline hafnium dioxide powder. SEM images show a powder consisting of individual grains with a size of 10-400 μm. The grains are nanostructured and composed of smaller particles of 40-220 nm, giving a median size of 67 nm.

XRD and Raman data show a completely matching monoclinic HfO_2, P21/c space group [64].

PL emission and PL excitation (PLE) spectra measured at different temperatures is shown in Figure 2.17. At room temperature a single broad emission peak is seen at 2.6 eV, excited under UV light. This is associated with oxygen-deficient centers as shown previously Gritsenko et al. When the temperature is lowered below 200K, emission peak at 4.2 eV dominates the spectrum with the most efficient excitation taking place at 5.9 eV. The optical absorption (OA) spectrum shown in Fig. 2.17 shows an increase in absorption at photon energies of $hv > 3.5$ eV with a weakly pronounced shoulder in the 4.9 - 5.1 eV region. This is consistent with the presence of the 4.5 eV band in the PLE spectrum.

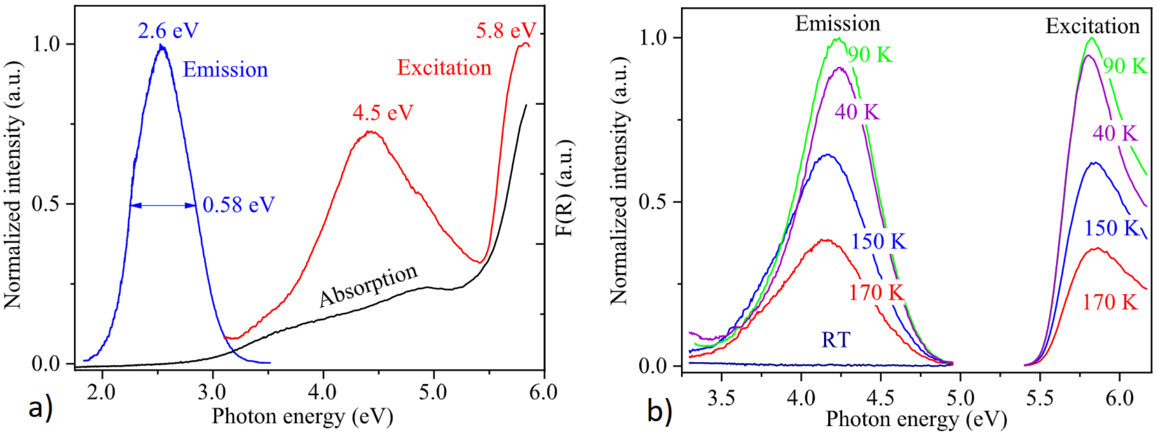

Figure 2.17: Hafnia PL, PLE and OA spectra measured at different temperatures. a) the spectra at room temperature; b) the spectra under study at different temperatures. PL and PLE spectra are normalized to maximum intensity. [63]

According to calculations [44, 65], oxygen vacancies in different charge states of O_{3f} and O_{4f} create new energy levels in the forbidden gap, with corresponding optical transitions defining spectral characteristics of the OA spectrum. The sharp increase in absorption at $hv > 5.5$ eV corresponds to the typical monoclinic hafnia intrinsinc absorption edge and also coincides with the excitation energy of the STE (self-trapped excitons) [66–68].

Direct (5.61 ±0.05 eV) and indirect (5.31 ±0.05 eV) band gaps were estimated using the Tauc approach [69]. In the region of $hv < 5.68$ eV, in-direct permitted transitions dominated, however in the range of 5.68 eV$< hv <$5.76 eV, both direct and indirect transitions form the OA spectrum within the intrinsic edge region. Only the direct allowed transitions take place in the range of $hv > 5.76$ eV.

The band gaps estimated in the work of Shilov et al. are in good agreement with these studies. It can be concluded that the intrinsic absorption edge in pure hafnium dioxide can be created via both direct and indirect allowed band-to-band transitions. It has been previously demonstrated in thin films [51, 68]and monoclinic HfO_2 single crystals [70] the possibility of simultaneous realization of the two types of optical transitions. According to Refs. [71, 72], an indirect allowed transition occurs between the Brillouin zone points $\Gamma \rightarrow B$, whereas the direct one corresponds to the process $\Gamma \rightarrow \Gamma$.

The experimental temperature dependency I(T) of the PL intensity of the monoclinic HfO_2 powder is shown in Fig. 2.18. The emission intensity increases in the temperature range of 40–90 K and reaches a maximum at 90 K. At T>90 K, the intensity begins to fade, and at T 200 K, no emission is detected. As a result, the I(T) dependency has two distinct behaviors: enhancement (negative quenching) at T<90 K and quenching at T>90 K.

The modified Mott relation [73] was used to investigate the temperature dependence I(T) of the luminescence intensity:

$$I(T) = I_0 \frac{1 + P_{NQ} exp\left(-\frac{E_{NQ}}{kT}\right)}{1 + P_Q exp\left(-\frac{E_Q}{kT}\right)} \tag{2.2}$$

where I_0 is the emission intensity at T $\rightarrow$ 0 K; P_{NQ} and P_Q are corresponding pre-exponential factors; E_{NQ} is the activation energy of the emission enhancement process, eV; E_Q is the activation energy of the emission quenching process, eV; k is the Boltzmann constant, $eV \cdot K^{-1}$.

Fig. 2.18 shows the experimental data of I(T) approximated by the expression (2.2).A plot in Arrhenius coordinates is shown in the inset of Fig. 2.18. For T>90 K, the linear segment (R^2 =0.97) points to the PL temperature quenching activation origin.

The magnitude of the barrier for a thermally induced non-radiative transition from the luminous state of a self-trapped exciton and an F-center – hole pair on the same adiabatic potential surface could possibly be controlled by the energy E_Q [74]. The computed energy E_{NQ} comes near to the thermally activated barrier that must be exceeded for a free exciton to self-trap in monoclinic HfO_2 [75].

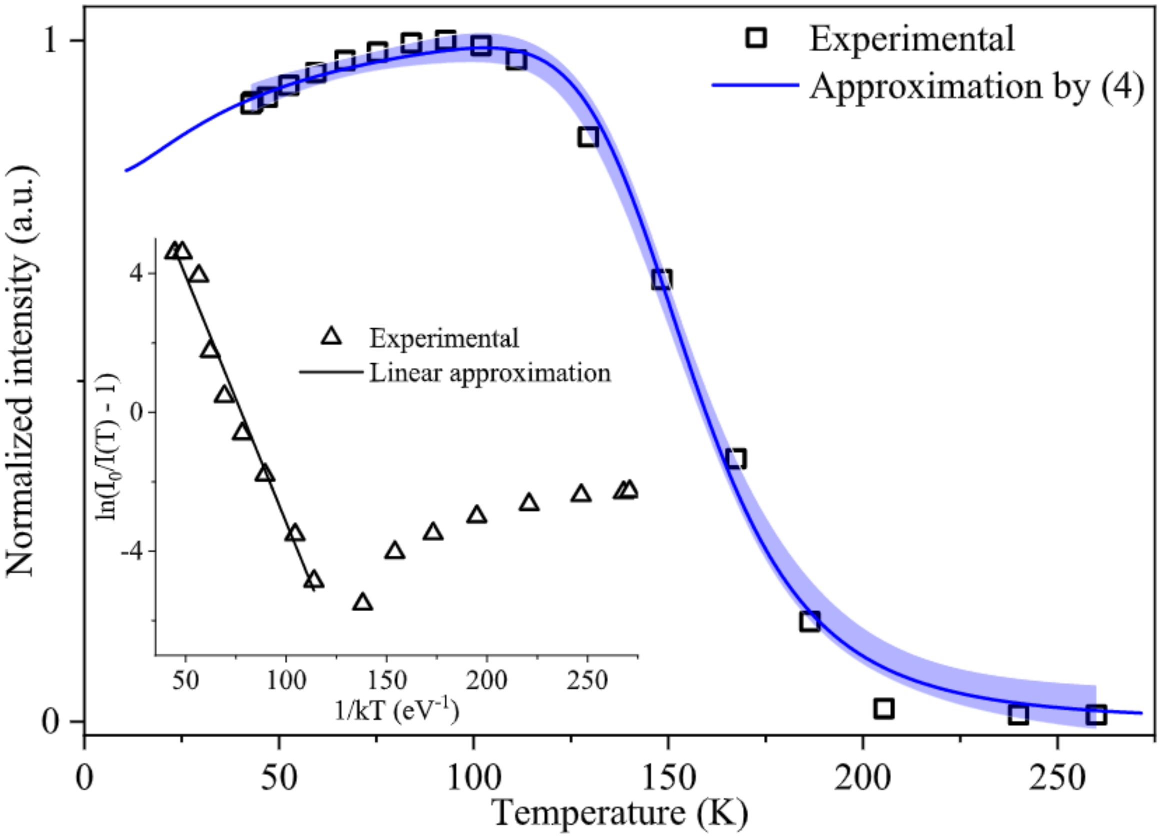

Figure 2.18: Temperature dependence of the emission intensity for the 4.2 eV band. The experimental values (square symbols) are approximated using the modified Mott relation (4) (blue line), blue shaded area along the line indicates 95% confidence interval. The inset contains the data for the temperature quenching of the investigated luminescence plotted in Arrhenius coordinates and their linear approximation (black line) in the corresponding range. [63]

The significant Stokes shift and large half-width suggest that the mechanisms of creating the 4.2 eV emission are based on STE radiative decay processes [75]. As monoclinic HfO_2 perfect crystals have a primarily ionic type of bond, theoretical predictions from [76] allow to hypothesize that charge carriers can self-trap and STE can occur. In particular, holes are localized near the top of the valence band formed by oxygen 2p-orbitals [76]. Insignificant displacements of non-equivalent O_{3f} and O_{4f} atoms cause localisation. As a result, STE interacts extensively with the A_u and B_u oxygen vibrational modes. The effect of oxygen vacancies can be enhanced by changing their charge state. In the process, the Hf–O bond is distorted significantly (up to 11% for a fully ionized vacancy) and a suitable potential well for a hole is created [44, 65]. Furthermore, the mutually approaching atoms increase the covalent contribution to this bond and cause the localiation of an electron [74]. It is worth noting that capturing an electron via an oxygen vacancy is energetically favorable [74]. This fact results in the coexistence of excitons and optically active F-type centers in different charge states. This is consistent with the findings of

Shilov, as a 2.6 eV blue luminescence typical of oxygen vacancies is observed simultaneously with the STE emission investigated when band-to-band excitation is used (see Fig. 2.17).

The obtained results were summarized in a configuration diagram of STE luminescence processes in Figure 2.19. Excitons with a theoretical binding energy of 0.57 eV are formed via 5.9 eV band-to-band excitation [77]. Heavy holes then cluster at the top of the valence band (VB) at $2p$ orbitals of O_{3f} atoms [76] (see fragment of elementary crystal cell in Fig. 2.19). Furthermore, similar to other transition metal oxides, more mobile electrons could be captured to states near the bottom of the conduction band (CB), which are dominated by the narrow 5d orbitals of hafnium atoms [76]. As a result these characteristics indicate that excitons in monoclinic HfO_2 with 4.2 eV luminescence have a self-trapping nature [46, 78–80]. The calculated quenching energy EQ =140 meV corresponds to the thermally triggered barrier of non-radiative decay of STE in this case, as shown in Fig. 2.19.

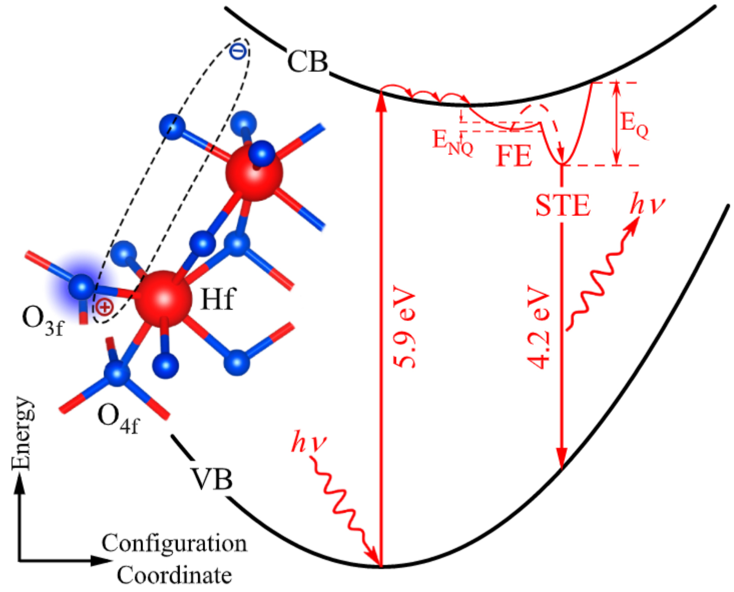

Figure 2.19: Model of the luminescence involving the STE under band-to-band excitation in monoclinic HfO_2. Inset shows schematically the fragment of monoclinic HfO_2 crystal cell with an electron and localized hole forming the self-trapped exciton (dashed line). [63]

The observed PL enhancement at temperatures below 90 K, according to the model developed by Shilov et al., could be attributable to excitations transfer during the decay of free excitons FE→STE. Furthermore, charge transfer mechanisms from oxygen vacancy traps to luminescent centers based on STEs are possible [76]. The lowest computed barriers for self-trapped holes and electrons hopping between equivalent sites in monoclinic HfO_2 in this case are 80 and 50 meV, respectively, and their thermal ionization energies are greater than 0.6 eV, i.e. $\geq E_{NQ}$ [76, 81–83]. As a result, the role of the aforementioned capture centers in the mechanisms of T<90 K STE PL augmentation appears to be insignificant.

To summarize the experimental studies, Shilov et al. showed that the magnitude of the Huang-Rhys factor 12.0–40.6 and the temperature trend of the spectrum features reveal STE radiative decay processes underlying the procedures of forming the indicated emission. The energies of effective phonons were estimated for the first time and were found to be 32 meV and 36 meV and being responsible for the shift and broadening of energy levels, respectively. As a consequence of the A_u+2B_u superposition of longitudinal and transverse vibrational modes of oxygen atoms, the estimated vibrational energies are close to the predicted maximum in the IR spectrum. In this regard, it was concluded that STE in monoclinic HfO_2 is caused by holes localizing near the top of the valence band formed by the electron shells of oxygen atoms.

The modified Mott equation was used to evaluate the temperature behavior of the 4.2 eV emission. The activation energies of STE luminescence quenching (E_Q =140 meV) and enhancement (E_{NQ} =3 meV) were also calculated. It was shown that the magnitude of E_{NQ} can be attributed to the height of a barrier that must be overcome in order for a free exciton to be self-trapped. A thorough investigation of the discussed excitonic phenomena could aid the development of hafnia-based structures with controlled optical response of intrinsic origin.

In summary, Kiisk proposed the excitation band at 4.2 eV being related to charge transfer transitions from valence band to singly or doubly ionized oxygen vacancies. A similar case was also found in YSZ, where the recombination of a hole in the valence band with an electron trapped at the oxygen vacancy promotes the vacancy into an excited state, resulting in a 2.4 eV emission [45].

Gritsenko showed that the thermal activation energy for the peak near 372 K is 1.25 eV. This value is half of the Stokes shift and corresponds to the thermal activation energy W_t= 1.25 eV, as measured in the charge transport studies. It was concluded, that the peak around 372K is caused by an oxygen vacancy. Gritsenko further suggests that the thermoluminescence peaks at temperatures 255, 291, and 315 K are caused by oxygen polyvacancies in HfO_2 based on similarities with other studies [55, 56].

Shilov et al. notes that according to calculations [44, 65], oxygen vacancies in different charge states of O_{3f} and O_{4f} create new energy levels in the forbidden gap, with corresponding optical transitions defining spectral characteristics of the OA spectrum. The sharp increase in absorption at $hv > 5.5$ eV corresponded to the typical monoclinic hafnia intrinsinc absorption edge and also coincided with the excitation energy of the STE (self-trapped excitons) [66–68]. Heavy holes were then thought to cluster at the top of the valence band (VB) at $2p$ orbitals of O_{3f} atoms [76]. Furthermore, similar to other transition metal oxides, more mobile electrons could be captured to states near the bottom of the conduction band (CB), which were dominated by the narrow 5d orbitals of hafnium atoms [76]. As a result these characteristics indicated that excitons in monoclinic HfO_2 with 4.2 eV luminescence have a self-trapping nature [46, 78–80].

Shilov also concludes that STE in monoclinic HfO_2 is caused by holes localizing near the top of the valence band formed by the electron shells of oxygen atoms.

As the theoretical and experimental aspects have been reviewed, we will now look into the phenomena and methods that will be used in the original studies of the author presented further in this work.

2.3 Material studies using luminescence

As a non-invasive and highly informative method, spectroscopy is used in all of the presented studies. We will therefore look at the luminescent properties of undoped HfO_2, europium and erbium, which are used as luminescent probes in hafnia and zirconia matrices. Luminescent probes that consist of rare-earth materials offer a way to obtain a more comprehensive understanding of the symmetry and local structures of the host materials. Moreover, they enable us to make inferences about the origin of oxygen vacancies in hafnia.

2.3.1 Intrinsic defect luminescence

The photoluminescence spectra of undoped HfO_2 and ZrO_2 is usually characterised by a broad PL band, centered at around 2.5 eV, consisting of several subbands. The origin of PL in undoped metal oxides is often explained by the intrinsic defects present in the host material.

While the literature does not provide a thorough analysis of the potential origins of these subbands, the most intense band (2.5 eV) has been identified as an F+ center - an anion vacancy with a missing electron. This band has been identified due to its very fast ns decay time is similar to the decay time values of F+ centers in several oxides [20, 84, 85].

2.3.2 Photoluminescence of rare-earth ions

Rare-earth ions are distinguished by their well-defined electronic levels established by the $4f^n$ electronic configuration [86]. The shielding effect given by the $5s$ and $5p$ electronic shells to the $4f$ electrons is another key characteristic of rare-earth ions [87]. Rare-earth ions are great candidates as luminous probes of the local structure of the system in which they are embedded because of these features.

Europium photoluminescence

Eu^{3+} has 60 electrons in total, with 54 electrons in the same closed shells as a xenon atom and 6 electrons in the $4f$ shell. This can be written as [Xe]$4f6$ or shortened to $4f^6$. The $4f$ shell is protected by the $5s^2$ and $5p^6$ outer shells [88].

The $4f^6$ configuration of Eu^{3+} is affected by several factors, including electron repulsion, spin–orbit coupling, the crystal-field perturbation and eventually the Zeeman effect (Fig.2.20). The electron repulsion is the interaction between the electrons in the $4f$ shell. The spin-orbit coupling is the interaction between the spin of an electron and the magnetic field created by its movement around the nucleus. The crystal field effect is caused by the interactions between the $4f$ electrons and the electrons of the surrounding ligands. The Zeeman effect is the splitting of energy levels in the presence of an external magnetic field[89].

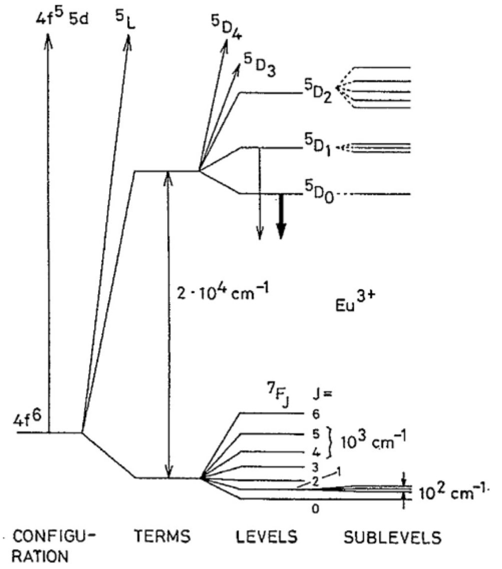

Figure 2.20: Partial energy diagram of Eu^{3+} ($4f^6$) showing the relative magnitude of the interelectronic repulsion (terms), spin–orbit coupling (levels) and crystal-field effects (sublevels). The downward arrows indicate the excited states $^5D_0$ and $^5D_1$ from which luminescence occurs. [89]

For an isolated ion, all $4f^6$ intraconfigurational transitions are forbidden electrical dipole (ED) transitions. When an europium ion is embedded in a matrix it interacts with the local crystal field. The mixing of distinct parity states caused by the local symmetry distortion eventually leads to partially allowed electric dipole transitions. Magnetic dipole transitions are allowed by spin–orbit coupling between various states, resulting in independence of local symmetry in the first order. This means that the degree of distortion of the Eu^{3+} site in relation to the centrosymmetric configuration can be determined by comparing the intensities associated with ED and MD transitions [90].

Erbium photoluminescence

Erbium is well known for enabling the upconversion luminescence phenomenon, absorbing infrared radiation and emitting a light of higher energy wavelength. A diagram of the energy levels involved in the upconversion emission of a sample doped with Yb^{3+} and Er^{3+} ions when excited with infrared light is shown in Figure 2.21.

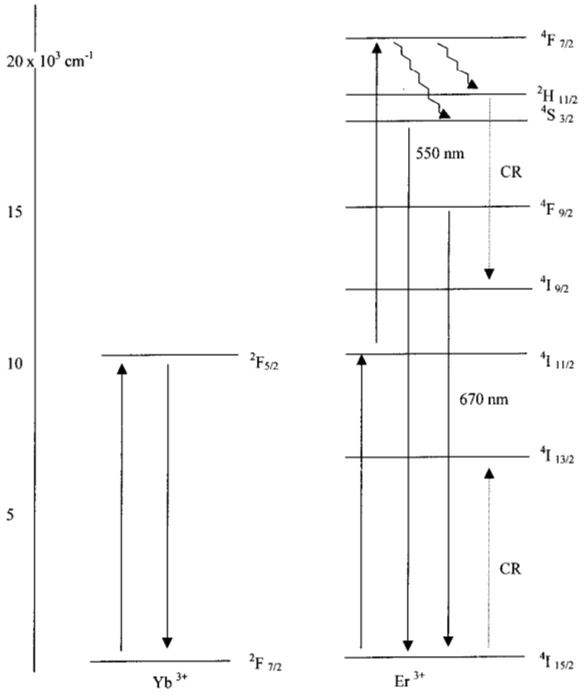

Figure 2.21: The energy level diagram for Yb^{3+} and Er^{3+} ions under infrared excitation. [91].

The wavelength of the diode laser is chosen to match the absorption transition between the ground state $^4I_{15/2}$ and the excited level $^4I_{11/2}$. When the atom is excited to the $^4I_{11/2}$ level, the same laser is used to pump it to the $^4I_{7/2}$ level. Nonradiative relaxation then causes the atom to populate the $^4S_{3/2}/^2H_{11/2}$ and $^4F_{9/2}$ levels, resulting in bright green (550 nm) and red (675 nm) emission due to the transitions $^4S_{3/2}$ to $^4I_{15/2}$ and $^4F_{9/2}$ to $^4I_{15/2}$, respectively [92–94]. At low concentrations of dopants, the $^4S_{3/2}/^2H_{11/2}$ levels primarily decay through radiation to the $^4I_{15/2}$ level, which results in a higher intensity of green emission [91].

When additionally doped with Yb^{3+}, there are three mechanisms of upconversion possible. The first is simple excited-state absorption, where Yb^{3+} ions do not participate in the process. The second is energy transfer upconversion, where two excited Er^{3+} ions (in the $^4I_{11/2}$ state) interact with each other, resulting in one ion being de-excited to the $^4I_{15/2}$ state and the other being excited to the $^4F_{7/2}$ state. This second mechanism involves the participation of Yb^{3+} ions in the energy transfer process [91]. This mechanism can be described as

$$2^4\mathrm{I}_{11/2} \rightarrow^4 \mathrm{I}_{15/2} +^4 \mathrm{F}_{7/2}$$

A third mechanism is realised via energy transfer from Yb^{3+} ($^2\mathrm{F}_{5/2}$) to Er^{3+} ($^2\mathrm{H}_{11/2}$). The ET from Yb^{3+} ($^2\mathrm{F}_{5/2}$) to Er^{3+} ($^2\mathrm{H}_{11/2}$) is dependent on the concentration of Yb^{3+} ions. This means that the efficiency of the transfer process is determined by the concentration of the donor and acceptor ions. After a second photon is absorbed by Yb^{3+} ions, the energy is transferred to Er^{3+} ions, which are then raised from the $^4\mathrm{I}_{11/2}$ level to the $^4\mathrm{F}_{7/2}$ level. This process can result in the emission of green and red upconversion luminescence through the following channels.

$$^2\mathrm{F}_{5/2}(\mathrm{Yb}^{3+}) +^4 \mathrm{I}_{11/2}(\mathrm{Er}^{3+}) \rightarrow^2 \mathrm{F}_{7/2}(\mathrm{Yb}^{3+}) +^4 \mathrm{F}_{7/2}(\mathrm{Er}^{3+})$$

The $^4\mathrm{F}_{7/2}$ (Er^{3+}) state decays nonradiatively to the $^4\mathrm{S}_{3/2}/^2\mathrm{H}_{11/2}$ and $^4\mathrm{F}_{9/2}$ (Er^{3+}) levels. The green emission is observed from the $^4\mathrm{S}_{3/2} \rightarrow {}^4\mathrm{I}_{15/2}$ transition while the $^4\mathrm{F}_{9/2} \rightarrow {}^4\mathrm{I}_{15/2}$ transition produces red emission. The increase in overall emission intensity in the presence of Yb^{3+} ions and Er^{3+} ions is consistent with the idea that the energy transfer process between these ions is dependent on their concentration. This suggests that the efficiency of the transfer process increases as the concentration of Yb^{3+} and Er^{3+} ions increases [91].

While rare-earth luminescent probes offer a valuable insight into the structure and symmetry of the host material, an equally important method of spectroscopy is thermoluminescence.

2.3.3 Thermoluminescence

Thermoluminescence in this work is used to determine the types of oxygen vacancies present in hafnia and their activation energies. The theoretical background of this phenomena is therefore studied in this section.

Thermoluminescence is the emission of light from an insulator or a semiconductor when it is heated. It is the thermally stimulated emission of light following the previous absorption of energy from radiation [54]. In general, emission-luminescence occurs when energy from radiation is transferred to the electrons of a solid, exciting them from a ground state to an excited state (transition (i) in figure 1.3a).

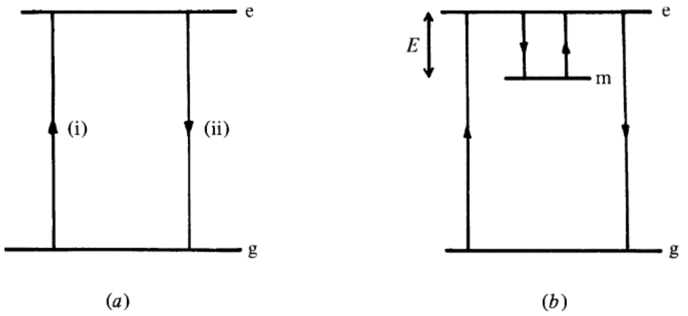

Figure 2.22: Energy transitions involved in the production of (a) fluorescence and (b) phosphorescence. [54].

The emission of a luminescence photon occurs when an excited electron returns to its ground state (transition (ii)). In the case of fluorescence, the delay between transitions (i) and (ii) is less than 10^{-8} seconds, and the process is not influenced by temperature [54]. According to Chen & Kirsh [95], Jablonski [96] was the first to explain temperature-dependent phosphorescence. In this model, the energy level diagram is modified by the presence of a metastable level (m) in the forbidden energy gap between the excited state (e) and the ground state (g). This allows an electron that is excited from the ground state to the excited state to become trapped in the metastable level. The electron will remain in this level until it is given enough energy to return to the excited state, at which point it can undergo a normal transition back to the ground state and emit a photon of light. This process is sensitive to temperature because the amount of energy needed to return to the excited state from the metastable level increases with decreasing temperature[54].

In general, the presence of impurities and structural defects in a material can create discrete energy states within the forbidden gap of the material. These energy states allow for radiative recombination to take place, leading to luminescence. These defects are known as ”luminescent centers.” The presence of vacant lattice sites or other impurities, lattice defects, and irregularities in the host lattice can also create unoccupied states, known as traps. These traps can delay the luminescence (phosphorescence) by temporarily holding the charge carriers (electrons and holes) before they can recombine with the luminescent centers [97].

The release of charge carriers from trapping levels by thermal processes depends on the probability of their escape, as described by equation 2.3.

$$p = s\exp(-E/kT) \tag{2.3}$$

where p is the probability of escape, s is the frequency factor, k is Boltzmann’s constant, E is the trap depth below the excited state and T is the sample temperature [54].

The charge carriers (electrons and holes) that are released from the traps when the material is heated can recombine radiatively through the CB or the VB, leading to thermoluminescence. The intensity of this TL, denoted as I_t, is proportional to the rate at which electrons and holes recombine at the recombination center level C (as shown in Figure 4). It can be expressed mathematically by equation 2.4, where the rate of recombination is determined by the probability of the charge carriers escaping from the trapping levels [54].

$$I_t = I_0 \exp(-pt) \tag{2.4}$$

where I_0 is inital intensity at $t = t_0$. The frequency factor s varies slowly with temperature and can be constant for a particular trap.

In practice, when an electron or hole is released from a trap, it has a certain probability of being recaptured. If the charge carriers that are released on heating are not retrapped, and all of them recombine radiatively, the TL intensity I_{TL} will be proportional to the rate at which the trapped carriers are released. This relationship is described by equation 2.5, where the rate of release of the trapped carriers determines the intensity of the TL [54].

$$I_{TL} = N_{t_0} s \exp(-E/kT) \exp\left[-(s/\beta)\int_{T_0}^{T} \exp(-E/kT)\, dT\right] \tag{2.5}$$

where N_{t_0} is the number of electrons trapped at initial temperature T_0 and β the rate of heating. Equation 2.5 is the Randall and Wilkins (1945) expression for the first-order kinetics under conditions of no retrapping.

In the case of second-order kinetics (as described by Garlick and Gibson in 1948 [98]), the released charge carriers are considered to have an equal probability of recombining at a luminescent center or being recaptured by the same trap. Under these conditions, the TL intensity I_{TL} can be expressed as

$$I_{TL} = \frac{N_{t_0}^2}{N} s \exp\left(\frac{-E}{kT}\right)\left[\frac{N_{t_0}}{N}\frac{s}{\beta}\int_{T_0}^{T} \exp\left(\frac{-E}{kT}\right) dT + 1\right]^{-2} \tag{2.6}$$

Finally, to determine trap depth levels in this work, the following second order deconvolution function developed by Chen et al. (1970)[99] is used

$$I_m = n_0 s \exp\left(-\frac{E}{kT_m}\right)\left[\frac{skT_m^2}{\beta E}\mathrm{e\dot{x}p}\left(-\frac{E}{kT_m}\right)(1-\Delta_m) + 1\right]^{-2} \tag{2.7}$$

where $\Delta_m = 2kT_m/E$, I_m is the glow peak intensity, E (eV) the activation energy, s (s^{-1}) the frequency factor, n_0 the initial concentration of trapped carriers, k (eV K^{-1}) the Boltzmann constant, T_m (K) the absolute temperature of the peaks.

While we have reviewed the methods used in the studies of hafnia and zirconia present in this work, it is also important to acknowledge the properties that make hafnia a useful and promising material in electronic applications such as the dielectric response.

2.4 Dielectric response

The property that makes hafnia stand out among other materials and enables it to be a substitute of SiO_2 in field-effect transistors is its high dielectric constant (high-k value), that as a result lowers the total leakage currents present and allows the reduction of the size of the thin-film layers even further.

The k value must be greater than 12, preferably 25–30, in order to achieve good capacitance performance. With an acceptable k value, the dielectrics will have a physical thickness that is sufficient to prevent gate leakage while not being too thick to obstruct physical scaling while obtaining the target EOT (equivalent oxide thickness). A large k value, on the other hand, is undesirable in CMOS design because it results in disadvantageous large fringing fields in the source and drain regions [100]. Fig. 2.23 demonstrate that the k values of certain oxides are inversely proportional to the band gap, implying that a higher k values is not necessarily better for practical applications.

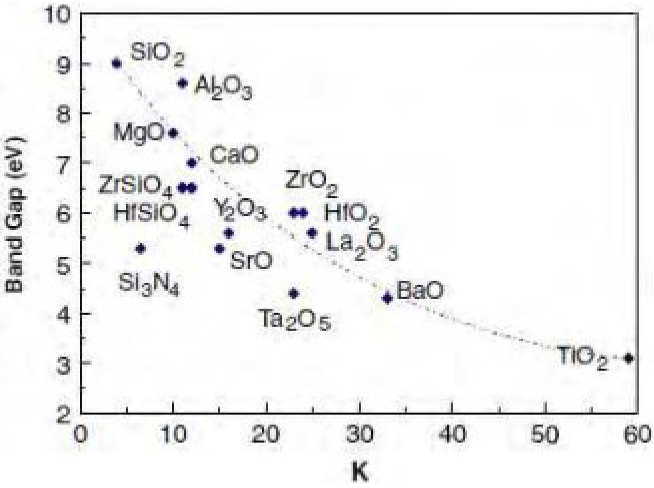

Figure 2.23: Static dielectric constant versus band gap for candidate gate oxides [4].

The tetragonal ($k \sim 70$) and cubic ($k \sim 29$) phases exhibit a substantially greater dielectric response than the monoclinic phase ($k \sim 16$), according to first-principles investigations [7]. S. Migita et al. recently revealed that ultra-thin cubic hafnia films have a very high kvalue of about 50 and a band gap that is similar to monoclinic hafnia. From as-deposited amorphous hafnia, ultrathin films of cubic hafnia have been achieved employing an ultrafast ramp with a reduced holdtime in the annealing process [22]. Low-temperature synthesis approaches to extremely crystalline cubic hafnia have also been established in other, more recent studies [101].

However, HfO_2 films have an unstable threshold potential, which is often attributed to charge trapping. Defects, in particular oxygen vacancies, have been thought to be a plausible cause for this charge trapping [102]. Cockayne in his 2006 study researched the impacts of oxygen vacancies on the electric properties of hafnia and discovered that while the introduction of vacancies alter the overall phonon density of states DOS, the changes in the dielectric constant are quite small - 3% or less with one O vacancy per 64 O atoms. Thus, the insertion of O vacancies has little to no impact on the polar phonons that make up the majority of the dielectric response of HfO_2. If vacancies vary at all, charged vacancies tend to suppress the dielectric response while neutral vacancies tend to amplify it. Neutral vacancies tend to enhance the dielectric response while charged vacancies tend to decrease it, if the dielectric constant is influenced at all. While the changes changes introduced by oxygen vacancies in monoclinic hafnia are small, the static dielectric tensor k_s almost doubles with phase shift from monoclinic to metastable cubic. This implies that the estimated increase in k_s of the associated compound ZrO_2 with the addition of oxygen vacancies is not primarily attributable to the oxygen vacancies themselves but rather to the stabilization of the cubic phase in comparison to the monoclinic phase [103].

The dielectric response of hafnia, however, is only a part of what makes hafnia a prospective material in future applications. The key property that has opened the path to many applications such as the ferroelectric field-effect transistor and ferroelectric random-access memories is its ferroelectric properties which are discussed shortly.

2.5 Ferroelectric Applications

For more than half a century, ferroelectricity has attracted widespread attention as a material property with the goal of bridging the performance gap between data processing and nonvolatile storage [104]. Nonvolatile storage choices such as hard disks, which have limited bandwidth, impose important performance restrictions, often known as the von Neumann bottleneck ([105].

Ferroelectricity was first discovered by Valasek in Rochelle salt in the 1920s [106], with subsequent investigations of conventional perovskite ferroelectrics such as $BaTiO_3$ (BT) and $Pb(Zr,Ti)O_3$ (PZT) taking place in the 1950s [107, 108]. However, the concept of FeFETs that was created in the 1950s had largely remained a theory until the discovery of ferroelectricity in $Si:HfO_2$ films due to limitations of materials. Hafnia films can finally overcome te thickness limitation and CMOS incompatibility of ferroelectrics with perovskite structures that existed previously [5].

Due to the substantially lower data storage speed relative to the operation performance when dealing with huge volumes of data, the von Neumann bottleneck has become a serious concern nowadays. Based on distributed parallel information processing, neural networks can effectively handle these challenges, and ferroelectric films can operate as biological synapses to effectively simulate the behavior of the human brain and produce artificial intelligence with high speed and low loss [109].

Elemental doping, interfacial engineering, surface energy effects, and deposition procedures have all been employed to alter and control the ferroelectric characteristics of HfO_2-based films [110–114]. HfO_2-based materials have received interest in a wide range of applications due to its multifunctional features, which include dielectric, ferroelectric, anti-ferroelectric, and piezoelectric performance.

HfO_2-based materials with ultra-thin thickness can be used in 3D integration of FeRAM, FeFET, and bioelectronic synapses due to their non-volatile properties [115, 116]. In Zr-rich circumstances, Muller et al. identified anti-ferroelectric characteristics of ZrO_2/HfO_2 films [117], and comparable phenomena were also discovered in Al: HfO_2[118] and Si: HfO_2[5]. The remaining polarization could be very tiny, or perhaps negligible, with no hysteresis loops, which is ideal for energy storage applications that want to improve efficiency. They are appealing for applications in supercapacitors, energy harvesting, and solid-state cooling [115, 119] because they have an electric field-induced anti-ferroelectric to ferroelectric phase change.

Mimura et al. also improved the thickness limitation from the nano- to micro-scale, and 1 m-thick Y:HfO_2 films with a remnant polarization of 14 C/cm^2 demonstrated good ferroelectric and piezoelectric capabilities [120]. Kirbach et al. discovered piezoelectricity in 20 nm-thick Si:HfO_2 films, which could aid in the creation of highly integrated nano-electro-mechanical-systems (NEMS) and sensor devices [121]. Under an external electric field, ferroelectric films can exhibit considerable strain, which can trigger micro- or nanoscale devices. Ferroelectricity has recently been observed in bulk Y:HfO_2, overcoming the present thickness limitation and paving the way for next-generation ferroelectric devices [122].

Several review papers on the structures and applications of HfO_2-based films in ferroelectric and anti-ferroelectric devices have been published in this field. Park et al., for example, summarized ferroelectricity and anti-ferroelectricity in HfO_2-based films from their origins to an overview of experimental work to their potential applications [115]. Following that, Park et al. discussed the benefits and drawbacks of fluorite-structure HfO_2 for memory devices, as well as how suitable doping, lowering oxygen vacancy concentrations, and anti-ferroelectric characteristics might help with device endurance [123]. Due to its low permittivity and high coercive field, Mikolajick et al. highlighted how HfO_2 can overcome major concerns in 1-transistor-1- capacitor (1T-1C) ferroelectric random-access memory (FeRAMs) and ferroelectric field-effect transistors (FeFETs) as compared to standard perovskite materials [124]. Park et al. discussed the current challenges and potential influencing factors in HfO_2 from the standpoint of fundamental physics for semiconductor devices, and provided possible solutions [125]. Based on models of physical mechanisms, Pesic et al. presented in-depth research of ferroelectric hafnium and related devices. Park et al. extensively evaluated anti-ferroelectric hafnium from its fundamental physics to energy-related applications based on both pyroelectricity and anti-ferroelectricity [126].

In addition to the simulation and experimental reviews mentioned above, novel insights are examined from the standpoint of defects and domains. Park et al. evaluated the effects of point defects (e.g. oxygen vacancies, carbon, and hydrogen) and two-dimensional defects on the ferroelectric characteristics of fluorite-structure oxides (e.g. interfacial layer and grain boundaries) [127]. Lee et al. presented a complete analysis of ferroelectricity in fluorite-structured ferroelectrics, with a focus on domain dynamics and related applications, particularly in neuromorphic computing [128].

The origins of ferroelectricity and the kinetic phase transitions of HfO_2 are still being debated. Wake-up effects, long-term tiredness response, and imprint effect are among the problems that must be overcome.

In order to enable hafnia as a potential ferroelectric material, it is important to understand the processes of defect formation and defect characterization. Defect formation can be influenced by doping the material with rare-earth ions, that both affect the bulk material by creating oxygen vacancies in a controlled manner and act as luminescent probes that provide information about the structure and symmetry of the material.

We therefore conclude the review of the theoretical and experimental evidence on oxygen vacancies in hafnia, having reviewed the methods used in this work to study these defects and the key properties of hafnia that make it a valuable material in already existent applications, as well as promising future ones.

The next chapters discuss the materials and methods used in this work in details, while the rest of the work focuses on the formation and characterization of oxygen vacancies.

3.MATERIALS AND METHODS

In this chapter, the methods of synthesis used in the studies that comprise this work are discussed. This section discusses the main methods for synthesizing hafnia and zirconia samples, namely sol-gel, hydrothermal, and solar physical vapor deposition techniques. It also examines the technical aspects of the measurements and equipment used to characterize the resulting samples.

3.1 Synthesis

Most of the samples used in this work have been synthesized either by the sol-gel method or the hydrothermal method. Additional descriptions of other methods of synthesis are provided in the Results and Discussion section.

3.1.1 Sol-gel

The amorphous network architectures of sol-gel materials are the result of rapid and (nearly) irreversible processes, as opposed to glass production from melts, where the thermodynamically advantageous crystalline structure is avoided by quick enough cooling. Therefore, molecular precursors, which serve as the foundation for the subsequent materials, are converted into metastable solids known as sol-gel materials through kinetically controlled processes. As a direct result, all reaction factors, including the precursor properties, have a significant impact on the structure and therefore the properties of sol-gel materials [129].

A **sol** is a suspension of colloidal particles in a liquid. These particles can be amorphous or crystalline and can have complex substructures, such as dense, porous, or polymeric structures. These substructures can be the result of aggregation of subcolloidal chemical units [130].

A **gel** is a solid network with a porous, three-dimensional structure that supports a continuous liquid phase. In many sol-gel systems used to synthesize oxide materials, gelation (the formation of gels) occurs when covalent bonds form between the particles in the sol. Gel formation can be reversible if other types of bonds, such as van der Waals forces or hydrogen bonds, are involved. The structure of a gel network is largely determined by the size and shape of the particles in the sol [130].

The tendency of fine particles in a sol to aggregate or clump together is caused by attractive van der Waals forces and the minimization of total surface or interfacial energy in the system. To prevent this aggregation and stabilize the sol, repulsive forces of similar magnitude must be introduced. This can be achieved by adsorbing an organic layer on the particles (known as a ”steric barrier”) or by creating electrostatic repulsion between the particles. This demonstrates the strong influence that organic additives and ionic species can have on the gelation process. The stability and coagulation of sols is crucial to sol-gel chemistry. Gelation can also be induced by rapidly evaporating the solvent, which is useful for the preparation of films or fibers [130].

When the liquid in the pores of a wet gel is allowed to evaporate, capillary forces cause the gel network to shrink, often by a factor of 5-10. This resulting dried gel is called a xerogel. The drying process can cause the monolithic gel body to be destroyed, resulting in a powder. If the gel is dried in a way that preserves its pore and network structure, the resulting dried gel is called an aerogel [130].

3.1.2 Hydrothermal

The hydrothermal method involves the use of an aqueous solution as a reaction system in a specialized closed reaction vessel to create a high-temperature, high-pressure environment. This is achieved by heating the reaction system and pressurizing it (or by allowing the vapor pressure generated by the system itself to build up). This process can dissolve and recrystallize substances that are poorly soluble or insoluble under normal conditions [131].

The main steps of crystalline growth under hydrothermal conditions are as follows:

1. The reactants are dissolved in a hydrothermal medium and enter the solution in the form of ions or molecular groups.

2. The ions or molecules are separated by the temperature difference between the upper and lower portions of the reaction vessel. The ions or molecular groups are transported to the lower temperature region, where they form a supersaturated solution around the seed crystal.

3. The ions or molecular groups are adsorbed, decomposed, and desorbed at the growth interface.

4. The adsorbed material moves at the interface.

5. The dissolved matter crystallizes.

In a hydrothermal reaction, water can either participate in the reaction as a chemical component or serve as a solvent or puffing accelerator [132, 133]. By using water as a pressure transmission medium, the formation of inorganic compounds can be accelerated by controlling the physical and chemical factors of the process. In high-temperature and high-pressure hydrothermal systems, the properties of water will undergo the following changes: The ionic product increases, and the ionic product of water rapidly increases with increasing pressure and temperature. Under high-temperature and high-pressure hydrothermal conditions, the rates of hydrolysis reactions and ionic reactions will increase naturally with water as the medium [134].

The compounds involved in the hydrothermal method have low solubility in water, so even at high hydrothermal reaction temperatures, the solubility of most substances in pure water is typically less than 0.1-0.2 wt.%. To increase solubility during the crystal growth process, one or more substances, known as ”mineralizers,” are often introduced into the system. Mineralizers are typically compounds that have high solubility in water and continue to increase in solubility with increasing temperature, such as certain low-melting salts, acids, and bases [135–137]. Adding a suitable mineralizer not only increases the solubility of the solute in the hydrothermal solution but also changes its solubility temperature coefficient. Some mineralizers can also form complexes with the crystalline material to speed up the rate of crystal nucleation [134].

3.1.3 Solar physical vapor deposition

The increasing interest in nanostructured materials has led to the development of new methods for creating novel materials with the ability to engineer their properties on the nano scale. The use of concentrated solar power technology, which has proven to be effective in converting solar radiation into high-temperature heat, has also been a driving force behind this development. As a clean and efficient form of renewable energy, concentrated solar power has been used to develop a unique process known as solar physical vapor deposition [138]. SPVD method was developed at the Odeillo-Font Romeu laboratory in France by utilizing ”heliotron” solar reactors that operate under concentrated sunlight in 2 kW solar furnaces [139]. This process involves melting and vaporizing a material in a solar reactor using concentrated solar radiation, before condensing it to form nanopowders [138].

Zirconia is a material that can withstand high temperatures, and as a result, the evaporation temperature for zirconia in the Heliotron reactor is estimated to be around 3000°C. These temperatures are reached by utilizing heat transfer through the concentration of solar radiation onto small spot sizes [140].

The schematic of the SPVD method is shown in Fig. 3.1 along with the evaporation process in Fig. 3.2.

The solar radiation is directed onto the sample by using mobile plane mirrors that track the movement of the sun and reflect the light onto a parabolic mirror. The parabolic mirror concentrates the light onto the sample with spot sizes smaller than 1 cm^2. To control the power, the flaps between the mobile plane mirrors and the parabolic mirror are adjusted. The target material is placed at the focal point of the parabolic mirror in a water-cooled target holder, which is located at the center of the glass balloon of the reactor [140]. This setup allows for the control of the ambient gas and gas pressure, as well as the flow of gas, which facilitates the transport of the evaporated particles. The evaporated particles are carried by the gas flow along the cooling part (the cold finger) to nanoporous ceramic filters. This method of particle transport reduces the amount of particle condensation on the walls and allows for controlled collection of the particles at the filters. The properties of the prepared samples are also affected by the power density, gas type, pressure, and flow rate in the reactor [140].

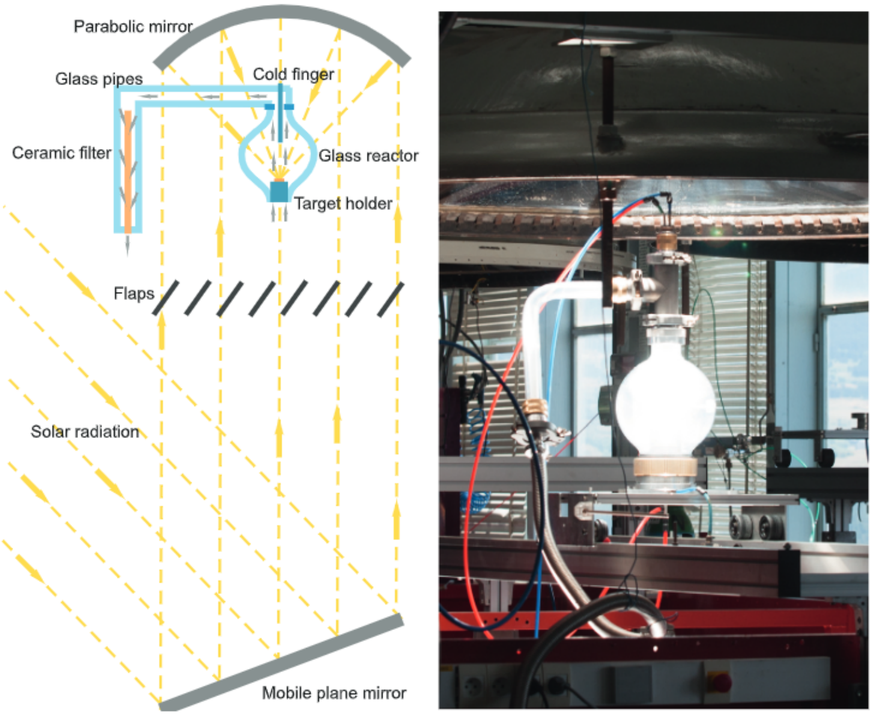

Figure 3.1: Schematic of Heliotron reactor (left) and its photograph (right) [140].

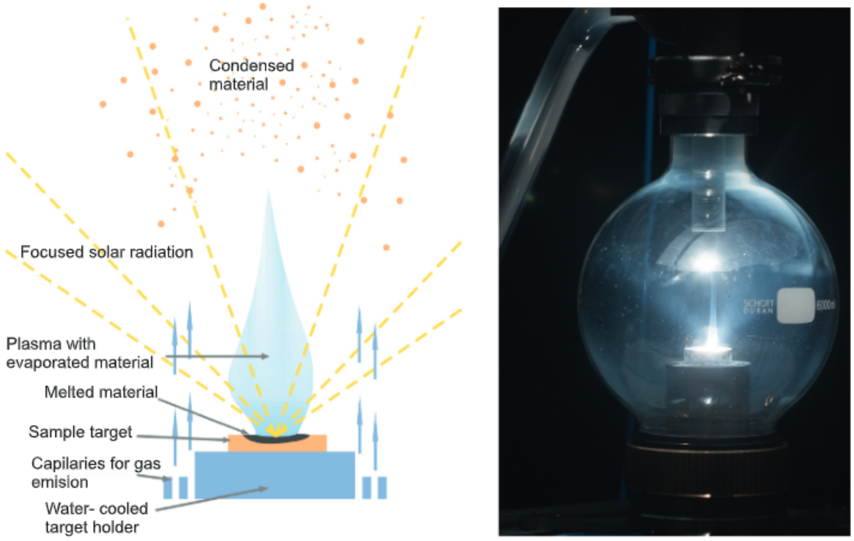

Figure 3.2: Schematic of plasma evaporation process inside Heliotron reactor (left) and photograph of reactor (right) [140].

3.2 Characterization

3.2.1 Structure and Morphology

X-ray diffraction (XRD) was measured using PANalytical X'Pert Pro diffractometer with Cu Kα radiation (1.5418 Å). The morphology of all samples was characterized by high-resolution SEM- FIB electron microscope Helios 5 UX (Thermo Scientific) operated at 2 kV using the TLD (through-the-lens detector) detector.

For lamella preparation samples were covered with gold. The crystalline size verification and morphology studies were performed using a transmission electron microscope (TEM, Tecnai G20, FEI) operated at 200 kV. The samples for TEM studies were placed on a holey carbon coated grid AGS147-4 (Agar Scientific).

3.2.2 Luminescence

Two different setups were utilized for luminescence measurements. The first setup included an Andor Shamrock SR-303i spectrometer paired with an Andor iDus401 CCD for the measurement of photoluminescence spectra, TL studies, and XRL. The second setup was a Horiba iHR320 imaging spectrometer combined with a SampleMax sample chamber and a Jobin Yvon/Horiba TRIAX320 excitation monochromator, which was used for the measurement of photoluminescence and luminescence decay kinetics. This spectrometer was also coupled with a photomultiplier tube and CCD. A list of parameters for these measurements is provided below:

Andor Shamrock SR-303i is a Czerny-Turner spectrometer that utilizes imaging toroidal optics with a focal length of 303mm and an aperture of f/4. Its wavelength resolution is 0.1 nm, and it can achieve a resolution of <0.2 nm with a 25 m pixel CCD detector. Its wavelength reproducibility is ±0.05 nm and its wavelength accuracy is ±0.2 nm. The spectrometer is equipped with an interchangeable triple grating turret that holds gratings of 150 lines/mm, 600 lines/mm, and 1200 lines/mm.

Andor iDus401 (DU401A-BV) CCD has 1024x128 active pixels and a pixel size of 26x26 m. It is air-cooled, capable of reaching temperatures as low as -55°C. It also has a maximum acquisition rate of 81 spectra per second.

Horiba iHR320 is an imaging spectrometer that uses a Czerny-Turner arrangement with a 320 mm focal length and an aperture of f/4.1. It covers a spectral range of 150 to 1500 nm when using the 1200 l/mm grating and it has a triple grating turret. The spectral resolution is 0.06 nm, and its wavelength accuracy is ±0.20 nm, repeatability is ± 0.075 nm, spectral dispersion 2.35 nm/mm, scan speed 159 nm/sec and step size 0.002 nm. It is equipped with three different gratings options: 1200 grooves/mm, 950 grooves/mm and 150 grooves/mm.

Jobin Yvon/Horiba TRIAX320 is a single grating excitation monochromator that comes with three different grating options: 1800 grooves/mm, 1200 grooves/mm, and 600 grooves/mm. For luminescence measurements, different excitation sources were used. They include a YAG:Nd laser (266 nm, 532 nm), conventional Deuterium and Xenon lamps, and an X-ray source which is directly connected to the sample chamber in the Andor setup.

In addition to Andor Shamrock SR-303i and Andor iDus401 setup, TL measurements were performed by **Lexsyg Research TL/OSL reader** from Freiberg Instruments with samples being irradiated by X-rays for 30min before measuring TL.

The decay kinetics of luminescence were measured using a photon counting head **H8259-02 (HAMAMATSU) and a P7887 counting board** (Fast ComTec GmbH) with minimal time bin 0.25 ns. The time resolution of the system was 1 ns.

The spectra that were obtained with the CCD in PL, XRL and TL measurements were not adjusted to account for variations in detection at different wavelengths, as the study only involved comparisons. For detailed information about the hardware used for luminescence measurements, the reader should refer to the corresponding papers included in this work.

3.2.3 Software

The majority of the software used was for graphical data representation, performing deconvolution functions on the obtained data and analysing X-ray diffractograms. Non-specific software used is not mentioned.

OriginPro is a scientific data analysis and graphing software. It provides tools for data analysis, graphing, and programming, and was used for creating graphical representations in this work. Additional scripts using the built-in programming language LabTalk were created for more efficient use of the software.

Mathematica provides a wide range of functions for numerical and symbolic computations, visualization, and programming. A custom script was used for deconvolution calculations for both photoluminescence and thermoluminescence spectra.

Profex software was used for the analysis of X-ray diffractograms and the determination of the phases of the materials using Rietveld refinement.

4.RESULTS AND DISCUSSION

4.1 Charge compensation in hafnia

Hypothesis 1:

A hypothesis is put forward that the luminescence intensity of rare-earth ions in HfO_2 is determined more by the vicinity and distribution of oxygen vacancies than by phase transition from monoclinic to tetragonal. This is explored by doping hafnia and zirconia with a charge-compensating element such as Nb^{5+} in addition to the Eu^{3+} ions. When a charge-compensating element is introduced, the amount of oxygen vacancies is reduced and as a result, the phase of the host material remains monoclinic and is not transformed to tetragonal. This allows us to judge the intensity of luminescence in different conditions.

4.1.1 Introduction

Many modern applications like LED emitters and various scintillators require durable luminescent materials. These applications are often based on wide band gap materials (HfO_2 or ZrO_2) doped with rare earth elements such as Eu, Er, Pr, Tb ad others [101, 141, 142]. The wide band gap also ensures that the thermal quenching effects of luminescence are lower thus increasing the overall luminescence intensity [143, 144]. Besides promising optical properties hafnia is also a high-k material and has already been applied in various microelectronic devices [145, 146]. It is one of the most promising materials in the search for a replacement of SiO_2 [143], for which a reduction in size any further is difficult to achieve due to its relatively low dielectric permittivity constant.

Both optical and electric properties in hafnia depend on crystal phase and defects. Undoped hafnia is expected to exist in monoclinic phase at room temperature and ambient pressure [101]; however, by adding dopants with lower valence or by decreasing the size of nanocrystals (crystal sizes below 30 nm) and thus increasing the surface energy, the tetragonal phases can be stabilized [147]. Theoretical calculations demonstrate that the tetragonal or cubic phases can be stabilized by oxygen vacancies alone [148]. This effect was proven by experimental studies performed on ZrO_2 matrix [149]. Recent studies [140, 146, 150] showed that in zirconia a strong overall reduction in Ln^{3+} luminescence intensity can be explained by intrinsic defects. However, the implementation of Nb^{5+} ions as charge compensators in the matrix can change the defect concentration and distribution thus highly increasing the resulting intensity. Zirconia and hafnia have very similar optical, electrical and structural properties, therefore, they are called twin oxides. Hence in this study, we are looking at Nb effect on Eu ion luminescence in hafnia.

4.1.2 Materials and methods

Materials

Hafnium tetrachloride ($HfCl_4$, purity 98 %), europium oxide (Eu_2O_3, purity 99,99 %), niobium pentachloride ($NbCl_5$, purity 99 %), were used as the starting materials and were purchased from Alfa Aesar. Citric acid ($C_6H_8O_7$, purity 99,5 %) and ethylene glycol ($HO(CH_2)_2OH$, purity 99 %) were used as a complexing and chelating agents, both purchased from Sigma Aldrich. Nitric acid (HNO_3, assay 65 %) was used to dissolve Eu_2O_3 and was purchased from Sigma Aldrich. Methanol (CH_3OH, purity 99,9 %) was used to dissolve $NbCl_5$ and was purchased from AppliChem. Analytical grade chemicals were used without any further purification.

Synthesis of doped HfO_2 nanoparticles

In the present work, HfO_2:Eu^{3+} and HfO_2:Eu^{3+}, Nb^{5+} nanoparticles were synthesized using a sol-gel polymerized complex method following the procedure described by Ramos-González et al. [151]. The molar ratio of metal ions, citric acid and ethylene glycol was 1:1:4, respectively. Three different doped HfO_2 samples were synthesized, where molar concentrations of Eu^{3+} ions were 5 and 10 mol%, and the molar concentration of Nb^{5+} ions was 5 mol%. To avoid the formation of niobium oxide, the appropriate amount of $NbCl_5$ was dissolved in methanol and was added dropwise to the metal citrate complex solution while constantly stirred. When gel consistency was obtained, this gel was heated at 350°C in an open oven for 2 hours for nitric oxide elimination and a black powder was obtained. After synthesis, each sample was split into three parts and calcined at 800°C, 1000°C and 1200°C for 2 hours and as a result, white powders were obtained.

Measurement methods

The crystalline structure of the samples was determined by X-ray diffraction (XRD) using an X-ray diffractometer (X'Pert Pro MPD) with Cu-Kα radiation (λ=1.54 nm). Crystalline sizes were not measured but are roughly estimated based on previous research.

Luminescence measurements were performed using two different excitation sources: a YAG laser FQSS266 (CryLas GmbH) 4th harmonic at 266 nm (4.66 eV) for photoluminescence measurements at room temperature and an X-ray tube with a tungsten anode operated at 30 kV and 10 mA for TL measurements.

All samples were pressed into tablets of equal size, which allowed for intensity comparison between the samples. The luminescence spectra were recorded using an Andor Shamrock B-303i spectrograph equipped with a CCD camera (Andor DU-401A-BV).

The decay kinetics of luminescence were measured using a photon counting head

H8259-02 (HAMAMATSU) and a P7887 counting board (Fast ComTec GmbH) with minimal time bin 0.25 ns. The time resolution of the system was 1 ns.

4.1.3 Results and discussion

Earlier works show that maximum luminescence intensity is acquired at 5mol% Eu concentration [152–154], therefore a sample of 5mol% Eu was chosen as a reference. However, the 5% of Eu is not enough to fully stabilize the tetragonal phase at higher annealing temperatures (with larger grain sizes of over 30nm). To assist the phase stabilization at higher temperatures, an additional sample with a higher concentration of 10mol%Eu was chosen. The aim of this research was to study the role of Nb ions in the crystalline structure, and Nb^{5+} ion concentration was chosen to match the lanthanide concentration, similar to previous studies [149, 155]. This decision was based on the fact that for each pair of ions only one oxygen vacancy is needed to compensate the charge. No vacancies are needed to form monoclinic phase, which means that Ln^{3+} ions are non-uniformly distributed in the matrix and tend to agglomerate (especially at higher temperatures monoclinic phase and large grain size). Samples with less than 5% content did not seem to provide any additional information and were not studied. A lower luminescence intensity and monoclinic phase would be expected as is seen in similar studies in Zr [153] and [152].

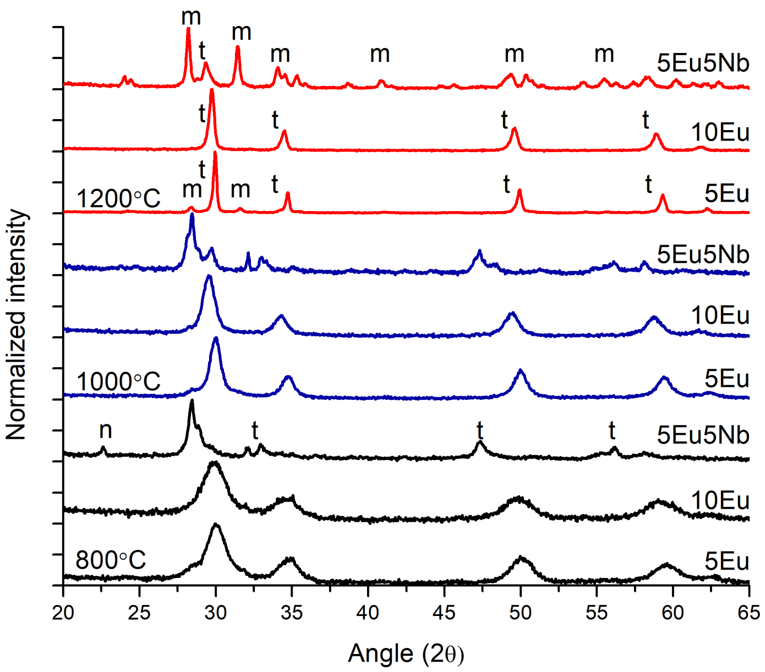

Figure 4.1: Hafnia structure dependence for all annealing temperatures and dopant concentrations (XRD)

As it is expected for the structure and the resulting luminescence intensity of hafnia to be dependent on the size of nanocrystal grains, all samples were annealed at three different temperatures: 800°C , 1000°C , 1200°C , similar to the approach used in other research works [140, 149, 152].

X-ray diffraction (XRD) data (Fig.4.1) reveals that when the annealing temperature was increased to 1200°C , phase transformation from tetragonal to monoclinic started taking place in the sample 5Eu (5mol% Eu). This phase transformation is assumed to happen due to nanocrystal grain size increase which results in excess surface energy being insufficient for stabilization [149]. For the sample containing Nb, the monoclinic phase was dominant for all annealing temperatures and at lower temperatures, besides the presence of monoclinic and tetragonal phases, additional phases of Nb_2O_5 can be seen. This means that the chosen method of synthesis does not ensure the creation of pure hafnia phases only, although niobium related phases disappear with the increase of the annealing temperature. Previous research demonstrates that inability to remain stable in a tetragonal phase for samples containing Nb is due to the resulting oxygen vacancy decrease in the crystallites [140]. Ln^{3+} ions are expected to not take part in tetragonal phase stabilizations due to oxygen vacancies not forming as a result of the charge compensation. Due to the oxygen vacancy reduction when doping with Nb ions, the lattice constant increases and according to Braggs law, the tetragonal peaks shift to lower angles as compared to samples doped only with Eu^{3+}. Crystallite sizes were calculated using the Scherrer equation [156] and were found to be (in nm): 5.8, 10.6, 48.4 for 5Eu samples, 5.3, 9.4, 26.5 for 10Eu and 13.4, 16.4, 45.5 for 5Eu5Nb for annealing temperatures of 800°C , 1000°C , 1200°C , respectively.

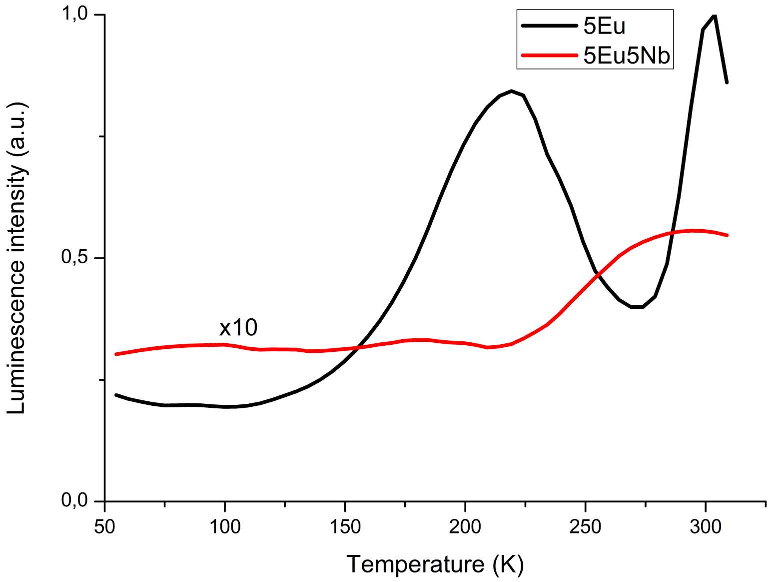

Figure 4.2: TL intensity distribution for peaks at 613nm.

Sample 10Eu (10mol% Eu) maintained a steady tetragonal phase for all annealing temperatures due to the relatively large Ln^{3+} concentration. It can be seen that the stabilization of tetragonal phases is dependent on Eu ion concentration and 5mol% is not sufficient for higher (>1000°C) annealing temperatures. However the concentration of 5mol% in various metal oxides is considered to be optimal for maximum luminescence intensity and phase stabilization [140, 152].

The oxygen vacancies in the HfO_2 matrix act as electron traps and as such, they have their characteristic TL (Fig.4.2) curves. Therefore, to determine the relative number of defects in samples with and without Nb, thermoluminescence measurements were performed for samples 5Eu and 5Eu5Nb (5mol%Eu and 5mol%Nb), annealed at 1200°C. TL peaks for the $^5D_0 \rightarrow {}^7F_2$ transition were monitored over all temperatures. With a geometric factor $\mu_g = 0.46$, the peak at 220K is somewhere in between the first- and second-order kinetics [157]. Possibly meaning that the probability of retrapping is not absolutely negligible (as it would be for first-order kinetics), but it also does not reach a full second-order kinetic status. Luminescence intensity throughout heating was ten times greater for the sample 5Eu, confirming a significant decrease in defects (electron traps) for the sample containing Nb, of which most are assumed to be oxygen vacancies [158].

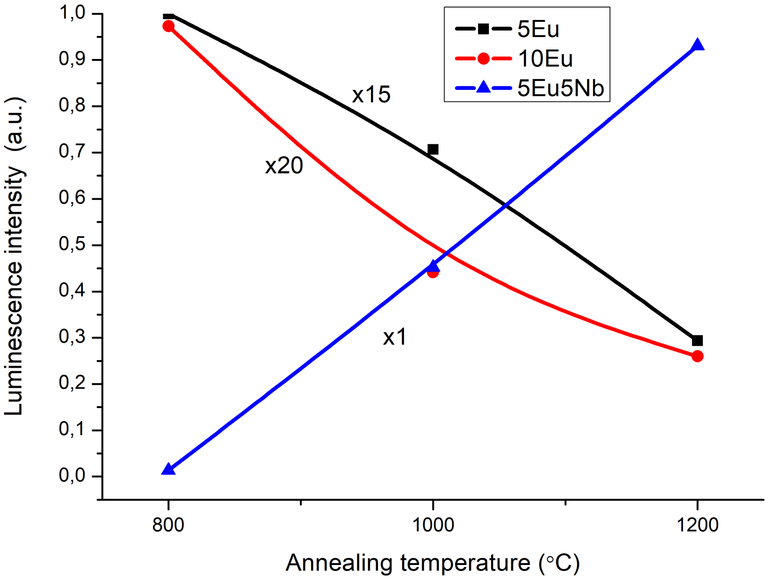

Figure 4.3: Integrated photoluminescence intensity (570-670nm range) dependence on annealing temperatures.

For samples annealed at 800°C , the most intense luminescence was observed for the sample containing 5% Eu (Fig.4.3) This observation correlates with previous results obtained for Eu doped hafnia [152, 154] and zirconia [159] where the optimal concentration for maximum Eu luminescence was also found to be 5%. The lower luminescence intensity of the sample containing 10mol%Eu can be explained by concentration quenching [152, 153]. With the increase of annealing temperatures, oxygen vacancies are thought to relocate between Ln^{3+} ions wherever charge compensation is needed. The distance to the oxygen vacancies becomes smaller as the temperature rises, thus increasing the chances for the energy coming from Ln^{3+} ions to get trapped in the defects.

Luminescence intensity for the Nb doped sample increases by a great margin for samples annealed at higher temperatrues. We associate the lesser luminescence intensity seen at lower annealing temperatures with Eu ion mixing with Nb_2O_5 phases, as the tenfold increase in luminescence for higher temperatures could not be explained solely by larger particle sizes or a decrease in defects.

At 1000°C and 1200°C the most intense luminescence was observed for the sample containing Nb, excluding the possibility that the increase in intensity of the Nb doped samples is a positive effect of Nb_2O_5 presence. Despite the larger grain sizes, with the increase in annealing temperature from 800°C to 1200°C the luminescence intensity halves for samples without Nb. This counterintuitive behaviour can be explained with the cation inability to diffuse at temperatures below 1200°C , therefore an anion diffusion takes place in the oxygen sublattice. The luminescence quenching is explained with oxygen vacancies present in the near vicinity of Eu ion (in the first coordination sphere). Similar behaviour has been shown in other research works [160].

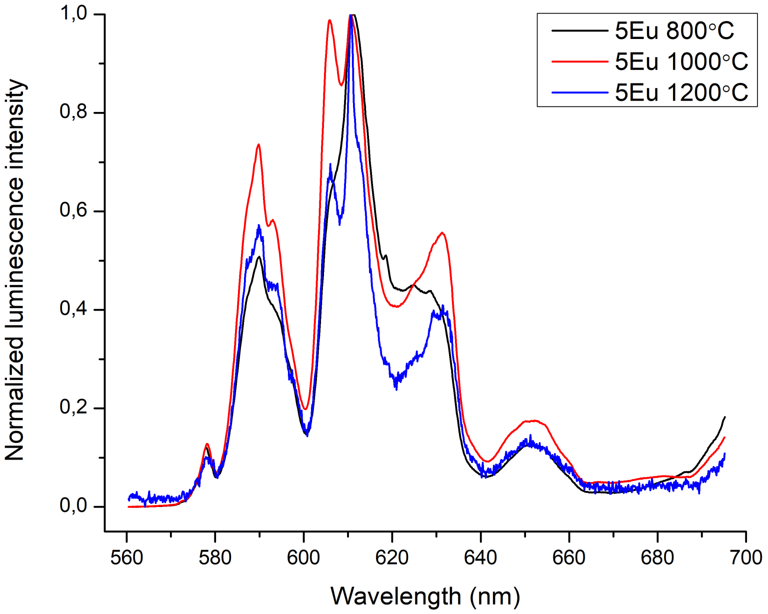

Figure 4.4: Spectral distribution for the sample containing 5mol% Eu

The peak at 607nm related to $^5D_0 \rightarrow ^7F_2$ transition in Eu ions is related to oxygen vacancy presence in Eu surroundings [161]. Figure 4.4 shows the spectral distribution at all annealing temperatures for the sample 5Eu. A new line at 607nm appears when the annealing temperature changes from 800°C to 1000°C, which fits the description presented in [161], however, the intensity decreases again at higher temperatures. From XRD measurements it can be seen that for the sample 5Eu, a phase shift starts taking place from tetragonal to monoclinic. For the stabilization of the tetragonal phase, oxygen vacancies are needed, however they are not necessary for the monoclinic phase. At 1100°C - 1300°C cation diffusion starts so the luminescence quenching can be explained by Eu ion agglomeration.

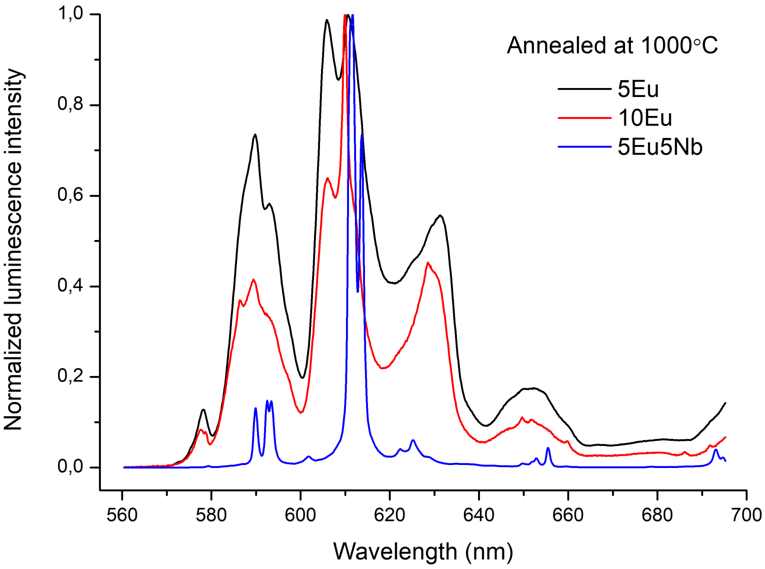

Figure 4.5: Spectral distribution for all samples annealed at 1000°C .

Due to the tetragonal phase being associated with the most efficient luminescence in previous studies of zirconia [161–163] it might seem that luminescence intensity would increase significantly if a tetragonal or cubic phase was achieved for hafnia doped with Nb too. However recent studies have shown that an increase in luminescence intensity occurs even after phase change from tetragonal to monoclinic in Er, Nb or Eu, Nb doped ZrO_2 [149, 150], which leads to think that both luminescence intensity and spectral distribution is mostly influenced by structure related defects (such as oxygen vacancies) and less so by local crystal field differences between monoclinic and tetragonal structures [164].

The spectral distribution in Fig.4.5 shows that the peak at 607 nm for the sample containing Nb is greatly reduced in intensity as compared to the other samples. The changes in the crystalline environment change the distribution of oxygen vacancies present in the lattice and is the main contributor to changes in luminescence spectrum.

As magnetic dipole transitions $^5D_0 \rightarrow {}^7F_1$ are assumed to be unaffected by local crystal fields (as opposed to electric dipole transition $^5D_0 \rightarrow {}^7F_2$)[89, 165], a local symmetry evaluation using the relation between the electric dipole and magnetic dipole intensities is presented.

Figure 4.6 shows that the overall symmetry for samples containing Nb is significantly lower, though, increases as the grain size becomes larger (at 1200°C). Symmetry for samples without Nb is higher and more allied. The observed results again lead to think that luminescence intensity is more related to intrinsic defects rather than the local crystal field influence.

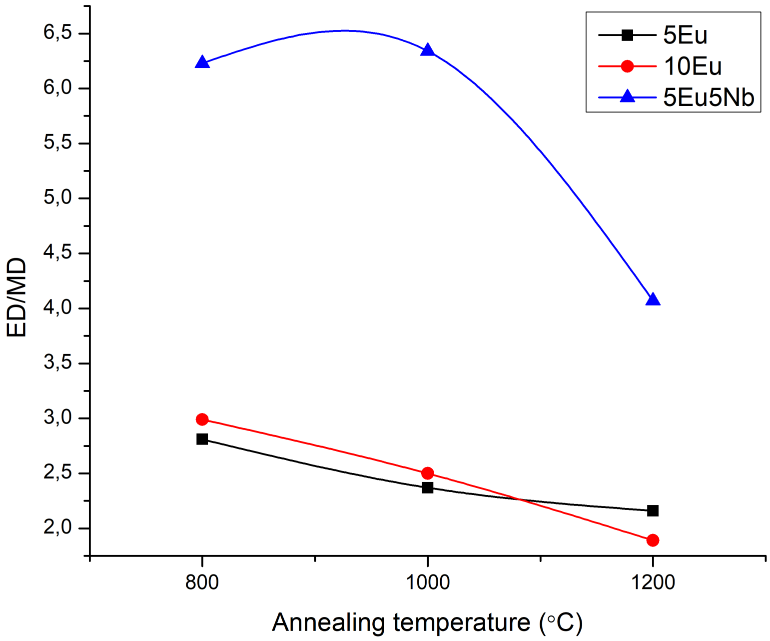

Figure 4.6: Local symmetry determined by the electric/magnetic dipole relation

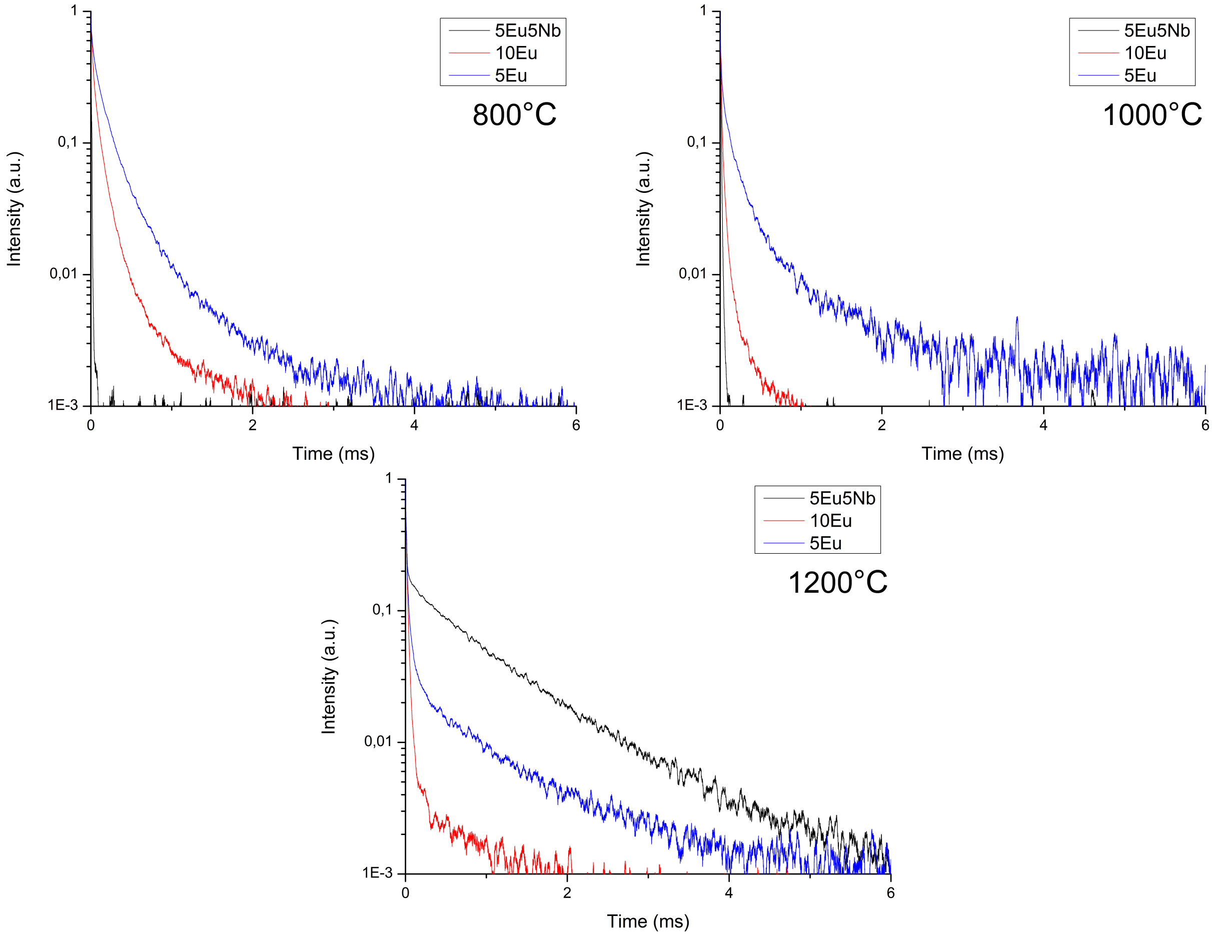

Figure 4.7: Time resolved luminescence measurements for samples annealed at 800°C (upper left), 1000°C (upper right) and 1200°C (bottom) (at 613nm)

Luminescence decay is strongly dependent on the presence of defects present in hafnia. Time-resolved luminescence measurements were made (Fig. 4.7) and by integrating the area of the obtained kinetics, the slow to fast component ratio was determined (Table 4.1). The kinetics were recorded for the most intense Eu peak - 613 nm. Luminescence decays showed complex nature and therefore the approximation was divided in three parts. All ratios correlate with luminescence intensity well - the smaller the ratio of slow to fast, the greater the luminescence intensity, with the exception of the 613nm line for samples containing Nb, for which a different fast component mechanism seems to be in place. Combined with luminescence intensity results, this ratio generally indicates that the transition is not only more probable, but also energy transfer is taking place and nonradiative transitions have become more dominant.

Table 4.1: Integrated area ratio of the slow component (30µs - 5ms) versus the fast component (0 -30µs)

		5Eu			**10Eu**			**5Eu5Nb**	
nm	**800°C**	**1000°C**	**1200°C**	**800°C**	**1000°C**	**1200°C**	**800°C**	**1000°C**	**1200°C**
613	1.0	1.3	2.2	1.5	3.3	16.1	264.4	56.0	72.3
607	0.9	1.3	4.1	1.7	4.9	12.9	15750.9	39.5	0.6
590	0.8	1.2	3.9	2.6	4.7	11.6	7360.0	66.2	0.4

Judd-Ofelt analysis

For the calculations of spontaneous emission probability and the quantum efficiency Judd-Ofelt theory was applied to the emission spectra and the necessary parameters were calculated as is described in this paragraph. Due to the fact that for Eu^{3+} electric dipole (ED) $^5D_0 \to {}^7F_{2,4,6}$ transitions depend only on one squared reduced matrix element [166] , the experimental Ω_λ intensities can be calculated from the ratio of the single magnetic dipole (MD) transition $^5D_0 \to {}^7F_1$ to ED transitions and are determined by the following formula[167]:

$$\Omega_\lambda = \frac{D_{md}\nu_1^3}{e^2\nu_\lambda^3}\frac{9n^3}{n(n^2+2)^2|\langle\Psi J||U^{(\lambda)}||\Psi' J'\rangle|^2}\frac{\int I_\lambda(\nu)d\nu}{\int I_1(\nu)d\nu} \tag{4.1}$$

where D$_{md}$ is assumed to be 9.6 x 10^{-42} esu^2 cm^2 according to previous calculations [168]. e is the elementary charge 4.803 x 10^{-10} esu, n is the refractive index 2.08 [50] and $|\langle\Psi J||U^{(\lambda)}||\Psi' J'\rangle|^2$ are the squared reduced matrix elements for Eu^{3+} that are independent of the host material and have been taken from Ref.[166]. Electric dipole transition strengths can be determined from the corresponding JO parameters using the following equation:

$$D_{ed} = e^2 \sum_{\lambda=2,4,6} \Omega_\lambda |\langle \Psi J || U^{(\lambda)} || \Psi' J' \rangle|^2 \tag{4.2}$$

The spontaneous emission probability A_R is related to electric and magnetic dipole strengths as follows:

$$A(\Psi J, \Psi' J') = \frac{64\pi^4 \nu^3}{3h(2J+1)} \left[\frac{n(n^2+2)^2}{9} D_{ed} + n^3 D_{md} \right] \tag{4.3}$$

where ν is the average transition energy, h is the Planck constant (6.63 x 10^{-27} erg s) and 2J+1 is the degeneracy of the initial state $^5D_0$. The total radiative rate A_R, determined by the sum over all radiative rates can be used to calculate nonradiative rate and emission quantum efficiency η (the ratio of photons emitted to photons absorbed by Eu^{3+} ions).

$$A_{NR} = 1/\tau - A_R \tag{4.4}$$

$$\eta = A_R/(A_R + A_{NR}) \tag{4.5}$$

Table 4.2: Ω_2, Ω_4 JO parameters, experimental decay lifetimes (τ) for $^5D_0 \rightarrow ^7F_2$, radiative transition rates (A_R), nonradiative rates (A_{NR}), emission quantum efficiency (η)

Sample, T (°C)	Ω_2**(x10^{-20}cm^2)**	Ω_4**(x10^{-20}cm^2)**	τ, μ**s**	A_R**(s^{-1})**	A_{NR}**(s^{-1})**	η**,%**
5Eu, 800°C	3.8	1.8	204.7	188	4697	3.8
5Eu, 1000°C	3.2	1.3	179.6	174	5395	3.1
5Eu, 1200°C	3.1	1.2	48.7	169	20349	0.8
10Eu, 800°C	4.2	2.0	117.4	199	8317	2.3
10Eu, 1000°C	3.6	1.1	57.7	177	17166	1.0
10Eu, 1200°C	2.9	0.9	27.1	162	36794	0.4
5Eu5Nb, 800°C	7.5	2.5	0.1	261	7131676	0.004
5Eu5Nb, 1000°C	8.2	2.2	110.4	268	8790	3.0
5Eu5Nb, 1200°C	5.3	1.9	914.8	215	878	19.7

For all samples $\Omega_2 > \Omega_4$. This indicates that Eu^{3+} ions are located at assymetric sites [169, 170]. A higher Ω_2 value indicates a more significant impact of the surrounding crystal field, which in our case means that samples annealed at lower temperatures are residing at more asymmetric sites and the ED transitions are supposedly stronger than they would be for more symmetric sites. However the increasing luminescence intensity of the 5Eu5Nb sample for more symmetric sites indicates other factors (such as size of the particles) being determinative.

4.1.4 Conclusions

This study demonstrates that the Nb ions implemented in 4th group oxides doped with lanthanide ions drastically increase the luminescence intensity. HfO_2 is the second system where this effect is demonstrated, therefore other similar systems are expected to fall in this category too. Doping with 5% Eu is not sufficient for phase stabilization at higher temperatures, however samples doped with 10% Eu (sufficient for phase stabilization) show lower luminescence intensity due to concentration quenching. Sample containing Nb has a significantly higher luminescence intensity starting at 1000°C and higher. The partial phase change from mostly tetragonal to mostly monoclinic accompanied by an increase in luminescence intensity in the samples containing Nb, indicates that the changes in luminescence intensity for samples not containing Nb are mostly due to oxygen vacancy presence and are not directly related to changes in the phase of crystallites and the resulting local crystal field. The calculated quantum efficiency also indicates a fivefold increase for the sample containing Nb annealed at 1200°C.

4.1.5 Thesis 1

The thesis of this study is therefore that the vicinity and distribution of oxygen vacancies determine the resulting rare-earth ion luminescence in HfO_2 and ZrO_2 rather than the surrounding crystal symmetry and phase. As it was seen, while the phase change from tetragonal to monoclinic in purely europium-doped samples seems to result in a reduction in the luminescence intensity, when the material is additionally doped with the charge-compensating element niobium, the phase change does not affect the resulting luminescence intensity and it increases with increasing annealing temperatures.

Thesis 1: The luminescence intensity of rare-earth ions in HfO_2 is determined more by the vicinity and distribution of nearby oxygen vacancies than by phase transition from monoclinic to tetragonal.

4.2 Formation of translucent nanostructured zirconia ceramics

Hypothesis 2:

A hypothesis is put forward that erbium ion luminescence is an effective way of monitoring defect formation and phase transformation in nanostructured ZrO_2 ceramics during the sintering process. In order to prove this hypothesis, zirconia samples are formed using the sol-gel method and solar physical vapor deposition and are doped with erbium. The pressure applied when pressing the powder into pellets impacts the phase of the resulting ceramics - this is thus monitored by studying rare-earth up-conversion luminescence in the different samples as the surroundings of the luminescent probe change.

4.2.1 Introduction

Interest in transparent and translucent zirconia ceramics has been growing in recent years due to the wide range of potential applications such as high temperature windows and viewports, high power laser diffuse optics, transparent armor, optical electronics and optical data storage [171–175]. The ceramics can also be used as fast scintillators [78].

Up until recently, the obtained translucent zirconia ceramics have been either monocrystals or cubic crystals as only with the advent of nanotechnology transparent ceramics from non-cubic crystals became possible [176–180]. Nanostructured ceramics can be obtained at low temperatures and low pressures and have high thermal stability [181–183]. Such ceramics can be used in laser optics, optical windows and other applications where high thermal stability is needed [184–187]. For example, in laser optics a limiting factor for the emission intensity is the thermal stability of the crystal [187] – if the optical pumping power is too intense, a large thermal gradient is formed across the crystal and the crystal might shatter. Nanostructured ceramics would allow for larger pumping powers and thus larger emission intensities.

Zirconium dioxide (ZrO_2) is a good potential material for use in nanostructured ceramics [175] as it has a wide band gap and a relatively large refraction coefficient [164, 175] compared to similar materials. The goal of this paper is to study the formation of translucent nanostructured ceramics. Research of mechanisms that affect the optical translucency was carried out by doping the translucent ZrO_2 ceramics with Er^{3+},Yb^{3+} and performing XRD, up-conversion luminescence, TEM and SEM studies.

4.2.2 Experimental procedure

Materials

Zirconium(IV) oxychloride octahydrate ($ZrOCl_2 \cdot 8H_2O$, purity 98 %, Sigma-Aldrich), erbium oxide (Er_2O_3, purity 99.99 %, Alfa Aesar) and ytterbium oxide (Yb_2O_3, purity 99.995, Alfa Aesar) were used as the starting materials for the preperation of Er^{3+}/Yb^{3+} codoped ZrO_2 sample. Glycine (Gly, purity 99.7 %, Sigma Aldrich) was used as a fuel, gelling agent and chelate. Nitric acid (HNO_3, assay 70 %, Sigma Aldrich) was used to dissolve Er_2O_3 and Yb_2O_3, as a oxidant and for elimination of chlorine. Analytical grade chemicals were used without any further purification.

4.2.3 Sample synthesis

Our preliminary studies showed that for transparent ceramic preparation the samples should be of minimal agglomeration and have high quality free standing nanocrystals with sizes 10-30 nm. To obtain homogenous samples with little agglomeration, the samples that were synthesized by the sol-gel method [164] were placed in a solar reactor in order to undergo solar physical vapor deposition (SPVD) process [140]. Additionally the samples were doped with 1 mol% Er^{3+} and 2 mol% Yb^{3+}, in order to allow spectroscopical studies of the obtained ceramics by using the Er^{3+} as a luminescent probe. The resulting samples also exhibited a more crystalline structure with even particles smaller than 5 nm showing easily recognizable crystalline structure in TEM measurements.

Sol-gel synthesis

ZrO_2 samples doped with 1 mol% Er_2O_3 and 2 mol% Yb_2O_3 were prepared by the glycine-nitrate assisted sol–gel combustion method following the procedure described by Lamas et al. [188]. The stoichiometric amount of $ZrOCl_2 \cdot 8H_2O$, Er_2O_3 and Yb_2O_3 were dissolved in nitric acid. After all starting materials were completely dissolved, a sufficient volume of deionized water was added to the solution so the molar concentration of all metal ions in the solution would be 0.2 M. After that, appropriate amount of glycine was added to the solution under constant stirring speed. The molar ratio of metal ions and glycine was 1:1.5, and molar ratio of glycine and NO_3- was 1:1.4. The resulting mixture was then heated at 90°C under constant stirring speed until a gel consistency was reached. The gel was heated up to 300°C, which led to the auto-ignition process and a dark gray powder was obtained. Subsequently, this powder was heated for 2 hours at 350°C in an open oven for nitric oxides and carbonaceous impurity elimination and a black powder was obtained. After synthesis, the obtained powder was calcined for 2 hours at 1000°C with heating rate 5°C/min in the air. Then the sample was naturally cooled down to room temperature, and as a result, white powder was obtained. For further applications, the prepared powder was pressed into pellet with a diameter of 13 mm and thickness of 5 mm under 10 tons and was used as a target for SPVD method.

SPVD method

Zirconia is a high-temperature material, and therefore, the evaporation temperature for zirconia in the Heliotron reactor is estimated to be about 3000°C. Such temperatures are achieved with heat transfer via concentration of solar radiation focused to small spot sizes. The estimated maximal power density can reach up to 5 kW/cm^2. Mobile plane mirrors follow the movement of the sun and reflect solar radiation onto the parabolic mirror, whose emission is concentrated on the sample with spot sizes below 1 cm^2. For power control, flaps between the mobile plane mirrors and a parabolic mirror are used. The target material is placed at the focus of the parabolic mirror in a water-cooled target holder, which is placed at the center of the glass balloon of the reactor. This setup facilitates variation of the ambient gas and gas pressure while also allowing gas flow for controlled material transport. The evaporated particles are transported by gas flow along the cooling part (the cold finger) to nanoporous ceramic filters. Such particle transport reduces the particle condensation on the walls and allows controlled particle collection at the filters. The power density, gas type, pressure, and flow rate in the reactor also affect the properties of the prepared samples. A schematic of the SPVD method can be seen in [140].

Measurements

The crystal structure of the samples was examined via X-ray diffraction (XRD) using an X-ray diffractometer X'Pert Pro (Cu K-$\alpha_{1,2}$.) The morphology of samples was characterized by high-resolution SEM-FIB electron microscope Helios 5 UX (Thermo Scientific) operated at 2 kV using the TLD (through-the-lens detector) detector. For lamella preparation samples were covered with gold. The crystalline size verification and morphology studies were performed using a transmission electron microscope (TEM, Tecnai G20, FEI) operated at 200 kV. The samples for TEM studies were prepared in two ways - by crushing the pellets and by preparing lamellas using SEM-FIB. The luminescence measurements were carried out at room temperature using a 975- nm Thorlabs L975P1WJ laser diode coupled with a Thorlabs ITC4005 controller as the excitation source. The luminescence spectra were recorded using an Andor Shamrock B-303i spectrograph equipped with a CCD camera (Andor DU-401A-BV).

Ceramic sample preparation

Several high quality samples were obtained from the SPVD process, such that when pressed at approximately 250 MPa pressure (limit of hand pumped hydraulic press) a slightly translucent ceramic was obtained. The obtained pellets showed a distinctive brown color, in contrast to the white color of the powders. It should be noted that we were not able to obtain transparent ceramics using any kind of sol-gel nanopowder samples without the additional step of SPVD method. The samples were pressed into pellets of 5mm diameter with a thickness of 1mm.

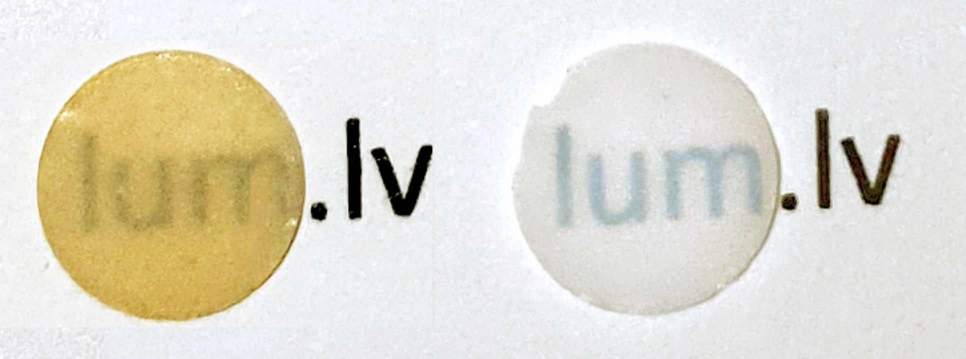

Figure 4.8: Pressed pellets with no annealing (left) and annealing at 700°C temperature (right).

4.2.4 Results and discussion

To understand the origin of the color of the ceramic and to study ceramic sintering, after pressing the powder into pellets the samples underwent annealing at various temperatures – 500°C, 700°C, 800°C and 900°C. The annealed samples lost the brown coloring and started to become white in color (Figure 4.9) with increasing annealing temperatures. At 900°C the sample remained white, however became non-translucent.A previous study by Srdić et al. in which zirconia nanocrystals were synthesized by chemical vapor synthesis also noted a brownish green color. According to Srdić, full density of the pressed ceramics is reached at around 950°C [189]. We assume that origin of this is enhanced light scattering and increase in pore size due to the enlargement of particle and cavity sizes when annealing at high temperatures [62, 149]. Several sets of samples were prepared and translucency achieved repeatedly. Annealing at various temperatures showed consistent results.

Figure 4.9: Pressed pellet with no annealing (RT) and annealing at 500°C, 700°C, 800°C and 900°C temperatures (right).

X-Ray diffraction

Figure 4.27 shows XRD spectra of the ZrO_2 powder as well as an unsintered pellet and pellets annealed at 750°C and 900°C. To ensure that the data is comparable the RT and 750°C spectra were taken of the same pellet before and after annealing. The data reveals an unexpected phase transformation from a mostly tetragonal phase powder sample to almost monoclinic phase when pressed in pellets (with monoclinic phase varying depending on annealing temperature from 68% to 84%, the rest being tetragonal phase) .

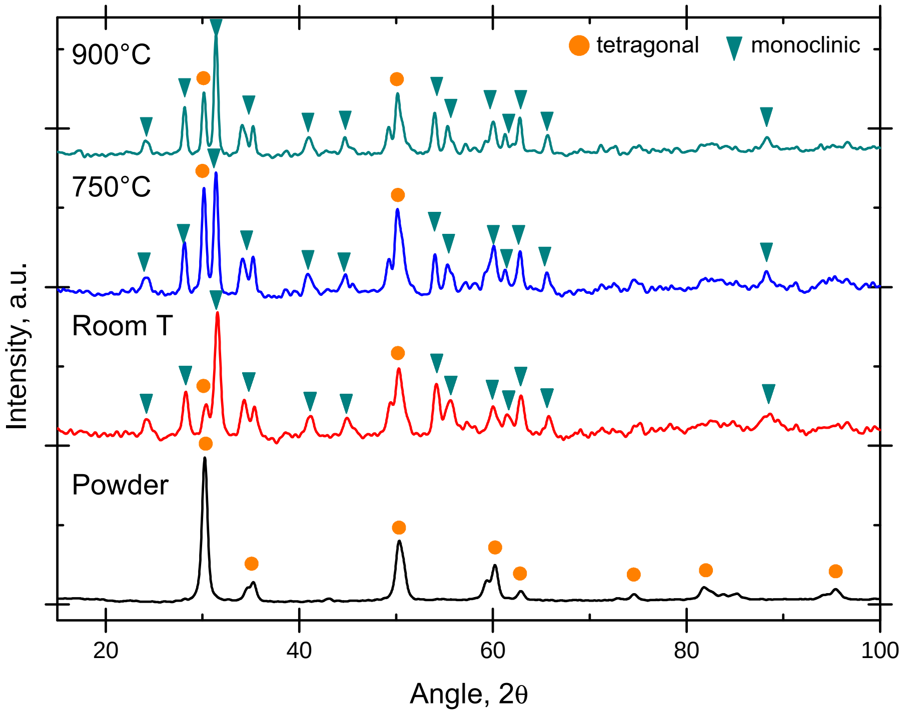

Figure 4.10: X-Ray diffraction data for the powder sample (black) and unsintered pellet (red), pellet annealed at 750°C (blue), and pellet annealed at 900°C (cyan).

To understand the phase transformation, stabilization processes in zirconia need to be considered. At ambient pressure ZrO_2 has three polymorphs — monoclinic, tetragonal, and cubic. Only the monoclinic phase of the undoped ZrO_2 is stable at room temperature (RT), however, the tetragonal and cubic phases can be stabilized by adding dopants with lower valence such as Mg^{2+}, Ca^{2+}, Y^{3+} (usually 3-14 mol%) [190–192]. In our case, the Er^{3+} and Yb^{3+} concentration is too low and the tetragonal phase in powders is stabilized mainly by grain size (surface energy). Once the nanoparticles are pressed together, the surface energy reduces and the tetragonal phase is no longer able to remain stable and a phase transformation to monoclinic takes place. This is due to the nanoparticles fusing together and as a result the effective surface area reducing. Srdić et al. observe a lower specific surface area for the pressed ceramics and explainit by the formation of contacts between individual particles decreasing the free surface area [189]. After applying a pressure of 250 MPa, the ceramic acquires a brown color - a large amount of defects are created that stabilize the monoclinic phase, as the pressure is not high enough to start phase transformation to tetragonal (according to Alzyab et al. the transformation from monoclinic to tetragonal phase starts at around 2 GPa [193]). By annealing at 750°C the defects disappear and tetragonal phase content slightly increases. By further annealing at 900°C rapid grain growth occurs, thus further reducing the surface impact in tetragonal phase stabilization. To understand the defect creation the samples were doped with Er for upconversion luminescence studies.

Up-conversion luminescence

Figure 4.11 shows that when comparing the up-conversion luminescence spectra between the pressed pellets and powder form, an increase in the red part of the spectrum relative to the green part can be seen. An overall decrease in the luminescence intensity can also be observed for the pressed sample. The red luminescence of the Er^{3+} ion is associated with cross-relaxation processes, which are correlated with the presence of defects near Er ions, therefore the position of Er^{3+} ions in the nanoparticles should be investigated further. Furthermore, the phase transformation from tetragonal in powders to monoclinic in ceramic pellets, could be the reason for the changes in upconversion luminescence.

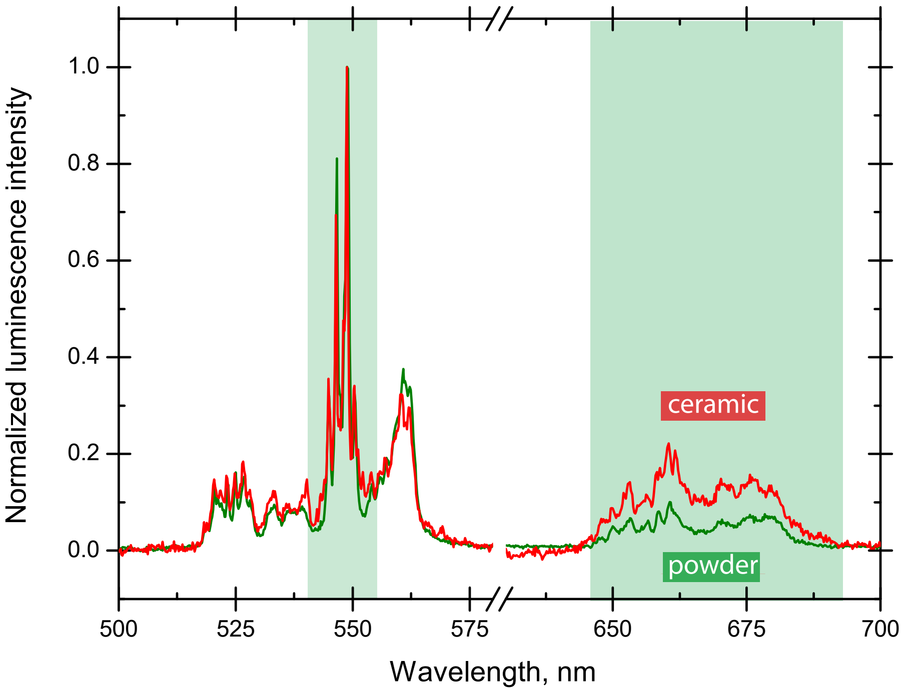

Figure 4.11: Up-conversion luminescence spectra for powder (green) and pressed pellet (red) samples before annealing.

When comparing the spectra of the annealed samples, it is shown in Figure 4.12 that the samples annealed at higher temperatures exhibit lower luminescence intensity in the red part of the spectrum relative to the green and have a higher total luminescence intensity. When annealed at 900°C, the luminescence intensity and red/green peak ratio returns to the level measured for powder sample, thus indicating that the crystalline phase affects upconversion luminescence less than intrinsic defect concentration. Until recently, it was believed that the decrease in photoluminescence that occurs at higher annealing temperatures is caused by the phase shift from tetragonal to monoclinic [148, 190, 194, 195]. However, a study by Smits et al [149] showed that when a charge compensating element such as Nb^{5+} is incorporated into ZrO_2 samples additionally to Er^{3+}, the phase change to monoclinic does not reduce photoluminescence intensity . Therefore the changes in the intensity of up-conversion luminescence can not be explained by changes in the local crystal field that occur due to a phase shift and instead lanthanide ion positions and interaction with defects should be evaluated.

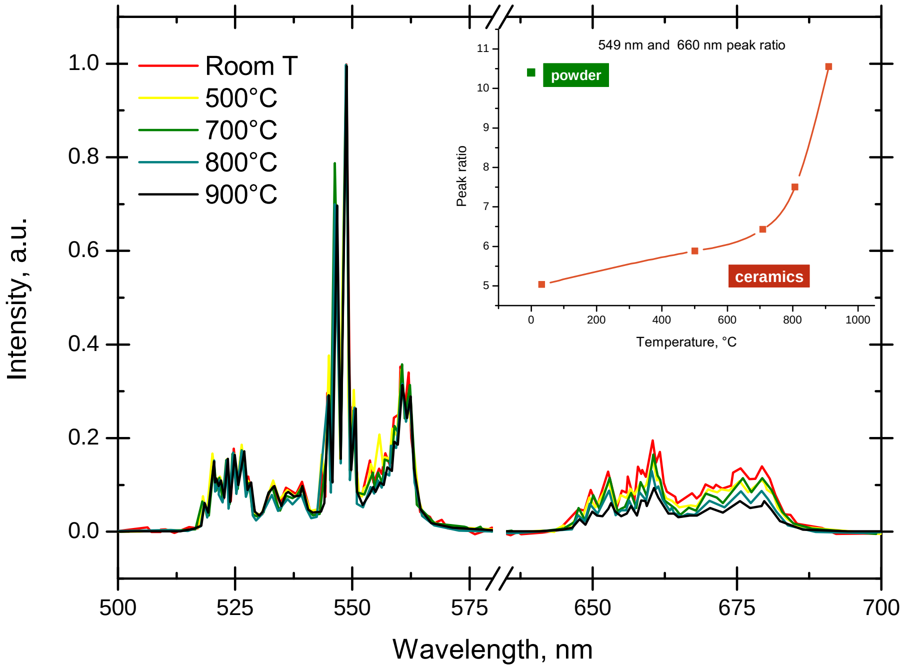

Figure 4.12: Up-conversion luminescence dependence on annealing temperatures.

It is known that cation (lanthanide) diffusion begins at around 1400°C, however anions start diffusing at 600°C [161]. Therefore the changes in the luminescence spectra can be explained rather by intrinsic defects than by an increase in Er^{3+} cross-relaxation efficiency. If the increase in the red luminescence when pressing the samples into pellets was due to the distance between Er^{3+} ions becoming shorter, annealing would not have a large impact on the luminescence intensity. As a result of the annealing, oxygen vacancy diffusion and a decrease in defect amount takes place, which results in the increase of the total luminescence. Unlike pressed ceramics, the impact of heating up to 900°C has minimal impact on the luminescence intensity of the powder, which also indicates that the decrease of luminescence intensity after pressing and the subsequent increase when pressed samples are annealed can be explained by intrinsic defects.

TEM and SEM study

Figure 4.13 shows bright-field TEM images of the powder samples obtained by the SPVD method. It can be seen that there is practically no agglomeration in the sample and a homogenous structure is maintained. It can also be seen that grains in powder samples have a round shape, whereas the pressed pellet ceramic grains are deformed and have a hexagon type shape as shown in Figure 4.14 B and C. At the same time, the ceramic samples have an increased tendency to stick together by the edges.

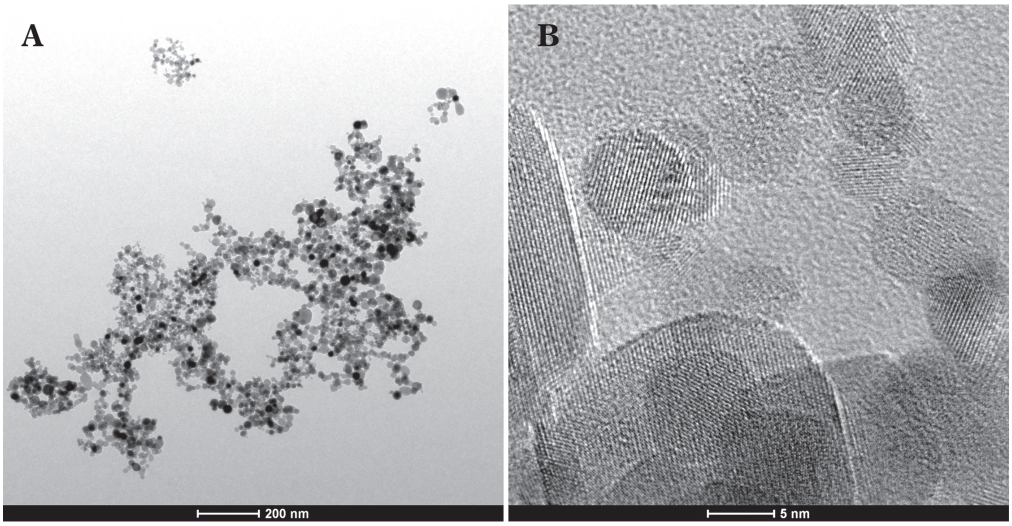

Figure 4.13: TEM images of the powder obtained by SPVD method.

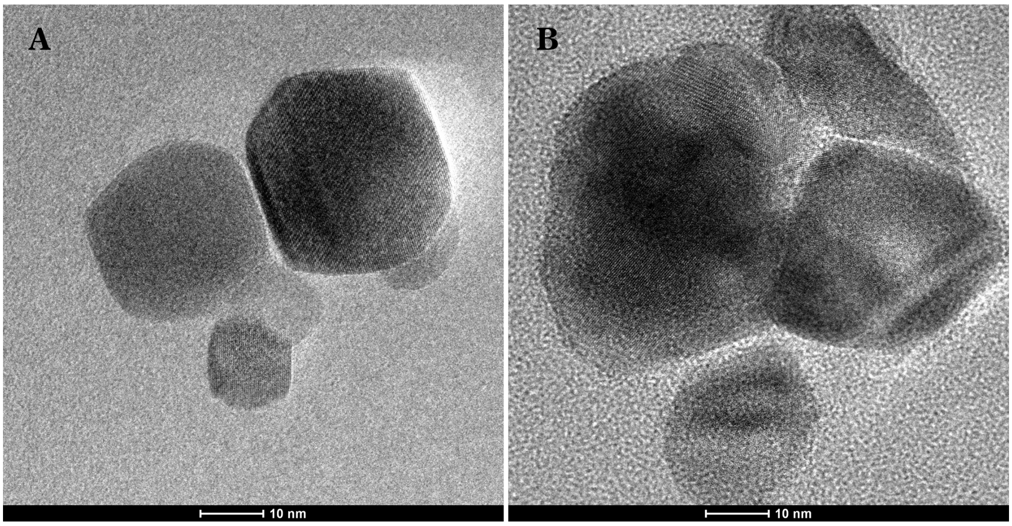

Figure 4.14: TEM images of the ZrO_2 powder from crushed ceramic pellet at room temperature A and annealed at 900°C B.

A typical site for defect creation is the boundary where two particles are pressed together. In Figure 4.15 cross-section (lamella) TEM images of pellets show a relatively low amount of pores and the pore size is comparable to the size of the particles. At the same time the grain size growth by annealing at 900°C is clearly visible and the pores are also more distinct. When pressure is applied to the powder, edges are formed at the boundaries of crystals. During annealing the smaller nanocrystals are fused into these edge arrangements.

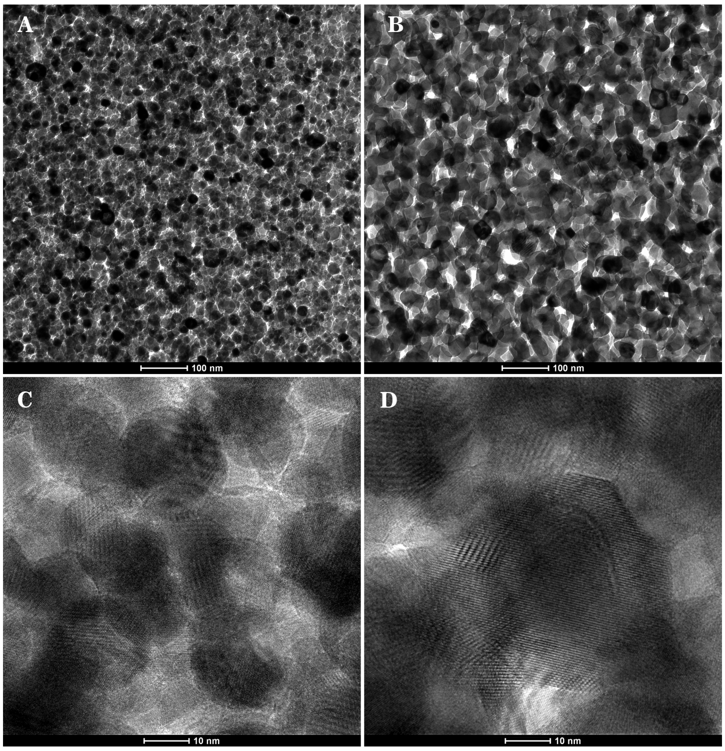

Figure 4.15: TEM images of lamella samples for unannealed ceramics (left), and lamellas from 900°C (right)

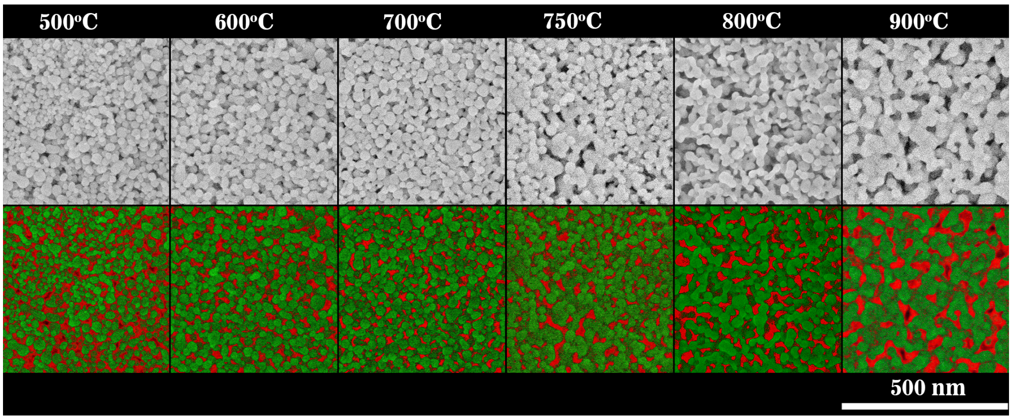

Figure 4.16: Top row: SEM images of pressed ceramic samples annealed at various temperatures. Bottom row: same images false colored to show particles (green) and pores (red).

Figure 4.16 shows SEM images of the pressed ceramics annealed at various temperatures. It can be seen that at low temperatures the pores (colored in red) are more abundant leading to less translucent samples. As the particle size increases with the annealing temperatures, the pores also change and become larger and fewer. During the sintering of zirconia nano-particles, small pores are eliminated and considerable growth of pores takes place. However at 900°C the particles (colored in green) have become too large and the sample becomes opaque. No shrinking was visible when the samples were annealed, meaning that the volume fraction of pores (i.e. the porosity) remains constant and only the pore size changes, becoming larger with higher annealing temperatures.

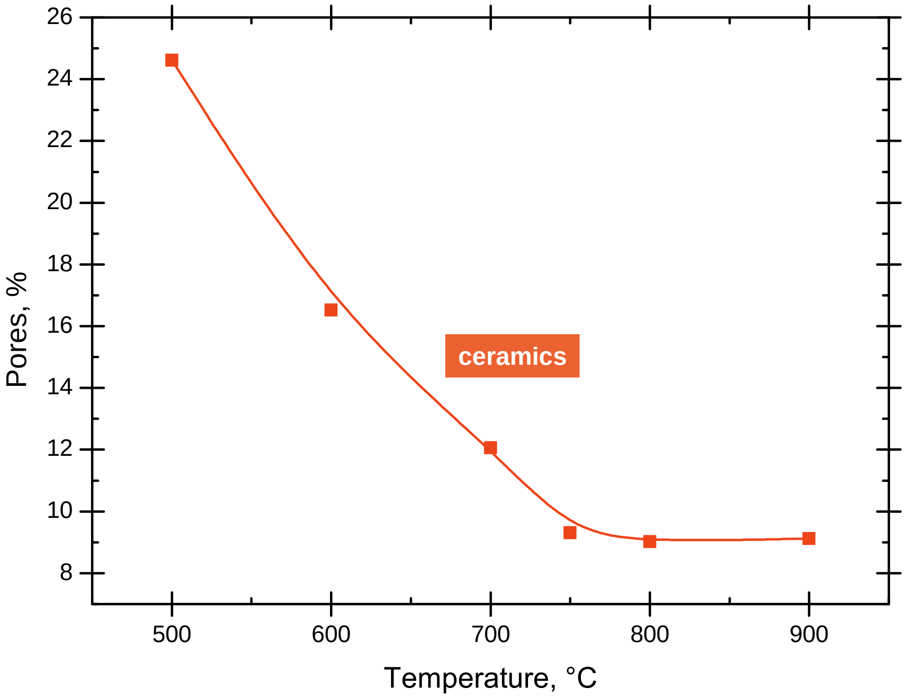

Figure 4.17: Top row: SEM images of pressed ceramic samples annealed at various temperatures. Bottom row: same images false colored to show particles (green) and pores (red).

Figure 4.17 shows the percentage of pores as determined from SEM images in Figure 4.16 It can be seen that around 750°C degrees the total volume of pores remains the same, while the number of pores decreases and individual volume of other pores increases.

In order to obtain a correlation between crystallite sizes and annealing temperatures we calculated mean crystallite sizes (τ) from XRD data (Figure 4.18) using the Scherrer equation

$$\tau = K \cdot \frac{\lambda}{\beta \cdot cos\vartheta}, \tag{4.6}$$

where shape factor K has been assumed to be 0.9; Cu Kαwavelengths λ_1=0.15406 nm, λ_2=0.15444 nm; β- line broadening at half the maximum intensity (FWHM) after substracting the instrumental broadening (0.06 - 0.07 FWHM); ϑ– Bragg angle.

Phase transformation could lead to inconsistencies in the calculated values, therefore additionally crushed ceramics were measured in TEM and particle size distribution acquired (Figure 4.19). The particle size in the samples follows a normal distribution and the average particle size increases significantly with an increase in the annealing temperature.

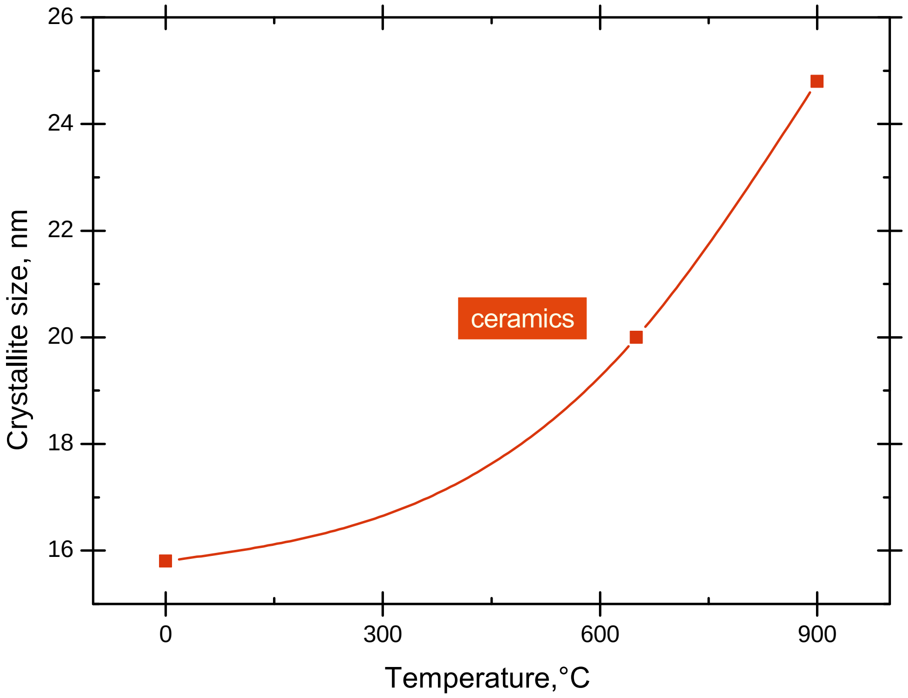

Figure 4.18: Average crystallite size in pressed ceramics depending on annealing temperatures (calculated from XRD line broadening).

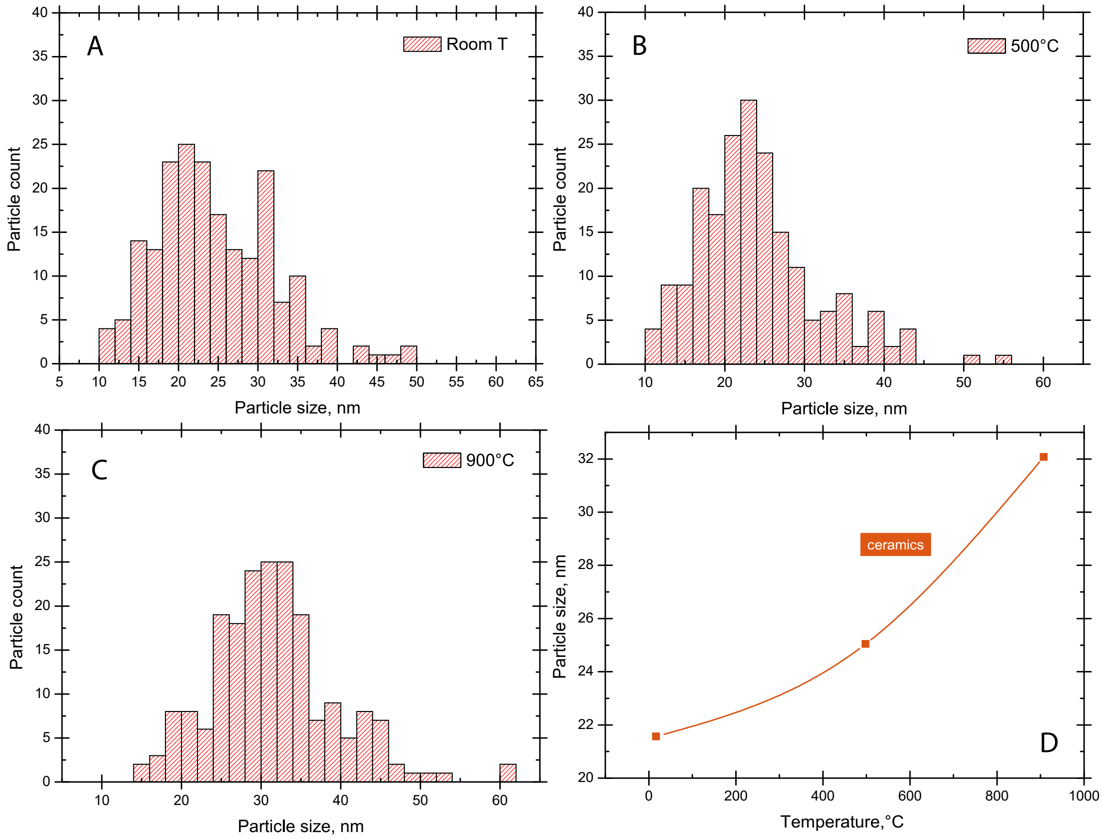

Figure 4.19: Nanocrystal size distribution in pressed ceramics depending on annealing temperatures. A-C particle size distribution for an unannealed sample and samples annealed at 500°C and 900°C respectively. D shows the arithmetic means of the number-weighted distributions shown in Figures 11A, B and C.

4.2.5 Conclusions

Translucent ZrO_2 ceramics have been obtained by performing SPVD after sol-gel synthesis.

The pressure of 250 MPa (diameter of pellet 5mm) is enough to create defects in nanocrystals of average size 25 nm. The luminescence quenching seen when pressing the ZrO_2 powder into pellets can be explained by the creation of intrinsic defects when pressure is applied rather than by the change in Er^{3+} ion cross-relaxation efficiency due to crystalline phase transformation. The annealing reduces the defects in ceramics thus increasing transparency, but at the same time, the pore size increases thus increasing light scattering.

4.2.6 Thesis 2

The thesis of this study is therefore that erbium ion luminescence is an effective way of monitoring defect formation and phase transformation in nanostructured ZrO_2 ceramics during the sintering process. When the samples were pressed into pellets, it was seen that the phase of the material is changed and intrinsic defects are created. Doping the materials with erbium, allowed studying this process in detail by analyzing the up-conversion luminescence data of the samples.

Thesis 2: Erbium ion luminescence is an effective way of monitoring defect formation and phase transformation in nanostructured ZrO_2 ceramics during the sintering process.

4.3 Thermoluminescence study of oxygen vacancies in HfO_2

Hypothesis 3:

A hypothesis is put forward that single (+1) and double (+2) charged oxygen vacancies at 3-fold coordinated (VO_3^{1+}, VO_3^{2+}) and 4-fold coordinated (VO_4^{1+}+VO_4^{2+}) sites of monoclinic HfO2 can be identified by thermoluminescence. Several factors are needed to perform this accurate analysis. First, to obtain a large enough sample group for a reliable study, the samples are synthesized using various methods and materials that ensure that the defects present are not case-typical. These samples are then studied and correlations of different characteristics with the resulting thermoluminescence data are analyzed. Secondly, the samples are doped with europium to create oxygen vacancies in a controlled manner. This allows for direct observation of oxygen vacancy formation and behavior via changes in their thermoluminescence spectra.

4.3.1 Introduction

Because of its desirable features such as a broad band gap of 5.25–5.95 eV [3] and a high-k value of 25 [4, 146], hafnia has become a popular choice among high dielectric gate materials for CMOS applications. Hafnia has a high heat of formation as well as excellent chemical compatibility with silicon, in addition being chemically and thermally stable [22, 196]. In recent years HfO_2 has been the material of choice in replacing SiO_2 when further downward scaling was rendered highly difficult due to leakage currents caused by the comparatively low dielectric constant of SiO_2 [197–200]. In addition, hafnia is also a promising material in transparent thin-film electroluminescence devices due to its high dielectric constant combined with transparency characteristics [201, 202].

In 2011 it was also discovered by Böscke et al.[5], followed by other publications [117, 118, 203] that under certain conditions, hafnia exhibits ferroelectric properties and further studies have enabled important technological prospects, such as ferroelectric field-effect transistors, which up until now have been mostly a theoretical concept due to the lack suitable materials [5, 115]. Ferroelectric hafnia is also a highly promising material in ferroelectric random-access memories [204–206].

However, compared to SiO_2, HfO_2 has a higher defect concentration [145, 200], resulting in a higher density of charge traps, transient instability of the gate threshold voltage, coulomb scattering of carriers in the substrate channel, and source-level voltage instability [6, 207]. Although HfO_2 has already been successfully used in large scale manufacturing as a high-k metal gate material, the intrinsic defects still present a significant challenge and require further studies.

Thorough theoretical studies of intrinsic defects in undoped HfO_2 have been published [6, 17, 21–23] examining the probabilities of defect creation and stability under various conditions, however, complementary experimental studies have provided limited information [43, 46, 48, 84, 208, 209].

The focus of this study therefore is on the oxygen vacancies found in hafnia studied using different methods of synthesis and thorough TL measurements, in addition with photoluminescence, XRD and TEM measurements. An in-depth analysis is enabled by combining two main factors: 1) various synthesis methods are used allowing to obtain more reliable and thorough data; 2) in addition to undoped HfO_2 samples were also doped with Eu^{3+}. Rare-earth ions are often used as luminous probes of the local structure of the system in which they are embedded [62, 86, 89, 90, 149, 210], however in addition to that, Eu^{3+} ions are known to create oxygen vacancies when incorporated into HfO_2 matrix. [43, 62, 87, 149].

4.3.2 Materials and methods

Materials

Hafnium tetrachloride ($HfCl_4$, purity 99.9 % (metals basis excluding Zr), Zr<0.5 %), europium oxide (Eu_2O_3, purity 99.99 %) were used as the starting materials for non-doped and doped HfO_2 and were purchased from Alfa Aesar, Germany. Hafnium dioxide (HfO_2, purity 99.9% (metals basis excluding Zr), Zr<0.5%, Alfa Aesar, Germany) was used as a references material.

Citric acid anhydrous ($C_6H_8O_7$, purity 99.0 %, Lach:ner, Czech Republic) and ethylene glycol ($HO(CH_2)_2OH$, purity 99.5 %, Fisher Chemical, Belgium) were used as a chelating agent and esterification agent for the sol-gel polymerized complex synthesis method, respectively. Additionally, citric acid was used as a chelating agent for the solution combustion synthesis method, where ammonium hydroxide (NH_4OH, concentration 25 %, Honeywell Fluka, Germany) was used as fuel. NH_4OH and potassium hydroxide (KOH, assay (acidimetric, KOH): 84.0 %, EMPLURA, Germany) were used as precipitating agents and as alkaline sources for hydrothermal and precipitation synthesis methods, respectively. Glycine ($C_2H_5NO_2$, purity 99.7 %, Sigma Aldrich, China) was firstly used as a chelating agent and also as a gelling agent for the sol-gel glycine synthesis method. Urea (NH_2CONH_2, purity 99.5 %, Carl Roth, Germany) was used a chelating and a gelling agent for the sol-gel urea synthesis method, and also as a fuel for the solution combustion synthesis methods. Hexamethylenetetramine ($C_6H_{12}N_4$, HMTA, purity 99.0 %, Chempur, Poland) was used as a chelating agent and fuel for the solution combustion synthesis methods. Absolute ethanol (C_2H_5OH, EtOH, 99.8 %, SIA “Jaunpagasts Plus”) was used for removal of synthesis reaction residue from the hydrothermal synthesis method. Nitric acid (HNO3, assay 70 %, Sigma Aldrich, France) was used for dissolved Eu_2O_3. All the chemicals used in this work are reagent and analytical grade and used without further purification.

Synthesis

Sol-gel synthesis (SG) 1.1) SG-PC:

Citric acid (CA) was dissolved in 100 ml of deionized water (0.2 mol L^{-1}) at room temperature under constant stirring speed for 10 min. Then 0.2 mol L^{-1} of $HfCl_4$ was added to this. Stirring was continued at room temperature for 10 min to dissolve the $HfCl_4$. Then ethylene glycol (EG) was added to this complex solution at room temperature under constant stirring speed. The molar ratio of CA and EG was 1:4, respectively.

1.2) SG-G:

$HfCl_4$ was dissolved in 100 mL of deionized water (0.2 mol L^{-1}) at room temperature under constant stirring speed for 10 min. Then 4 mol L^{-1} of glycine was added to this solution. Stirring was continued at room temperature for 10 min. Then appropriate amount of conc. HNO_3 was added to this complex solution at room temperature under constant stirring speed. The molar ratio of Gly and HNO_3 was 1:1.43, respectively.

1.3) SG-U:

$HfCl_4$ was dissolved in 100 mL of deionized water (0.2 mol L^{-1}) at room temperature under constant stirring speed for 10 min. Then 4 mol L^{-1} of urea was added to this solution.

2) Continued for all:

The reaction then was then carried out at 90 ℃ under constant stirring speed. After 3 hours a had formed. Heating of this gel was continued at 90 ℃ and a white solid gel was obtained. The gel was then placed in a vertical muffle furnace and heated at 400 ℃ with heating rate 13 ℃ min^{-1} for 2 hours. Subsequently, the sample was naturally cooled down to room temperature. After synthesis, the obtained sample was calcined at 800 ℃ for 2 hours with a heating rate of 5 °C min^{-1} in an air atmosphere.

For 5 atom% Eu^{3+}-doped HfO_2 nanomaterial synthesis Eu^{3+} ion solution was added dropwise to the Hf^{4+} ion solution and stirred for 10 min before the addition of urea.

Combustion synthesis (CO) 1) For all:

$HfCl_4$ was dissolved in 100 mL of deionized water (0.2 mol L^{-1}) at room temperature under constant stirring speed for 10 min.

2.1) CO-U:

A homogeneous Hf^{4+} ion solution was obtained and 4 mol L^{-1} urea was added to this solution. Stirring was continued for another 10 min to obtain a homogeneous metal-urea complexes solution. Then appropriate amount of conc. HNO_3 was added to this complex solution at room temperature under constant stirring speed. The molar ratio of urea and

HNO_3 was 1:1.5, respectively.

2.2) CO-H:

Then 0.4 mol L^{-1} of hexamethylenetetramine (HMTA) was added to this solution at room temperature under constant stirring speed. The molar ratio of Hf^{4+} ions and HMTA was 1:2, respectively. Appropriate amount of conc. HNO_3 was added to this complex solution at room temperature under constant stirring speed to obtain a molar ratio of HMTA and HNO_3 was 1:5, respectively.

2.3) CO-UH:

Then 0.4 mol L^{-1} of hexamethylenetetramine (HMTA) was added to this solution at room temperature under constant stirring speed. The resulting mixture was stirred at room temperature for 10 min and then 0.4 mol L^{-1} of urea was added to this solution at room temperature under constant stirring speed. The molar ratios of Hf^{4+} ions, HMTA and urea were 1:2:2, respectively. Stirring was continued for another 10 min to obtain a homogeneous metal-complexes solution. Then appropriate amount of conc. HNO_3 was added to this complex solution at room temperature under constant stirring speed. The molar ratios of HMTA:HNO_3 and urea:HNO_3 were 1:3 and 1:1.5, respectively.

3) Continued for all:

The resulting reaction mixture was stirred at room temperature for 10 min and the pH was measured to be 3. The mixture was heated at 100 ℃ until white gel was formed. The resulting white gel was then placed in a preheated vertical muffle furnace and the SCS reaction was carried out at 300 ℃ until a rapid gas evolution and self-ignition process was observed. After SCS, the obtained grayish white powder sample was calcined at 800 ℃ for 2 hours with a heating rate of 5 °C min^{-1} in the air atmosphere.

For 5 atom% Eu^{3+}-doped HfO_2 nanomaterials, the appropriate amount of Eu^{3+} ion solution was added dropwise to the Hf^{4+} ion solution under constant stirring speed before the addition of urea/HMTA.

Auto-ignition combustion synthesis (AIC) Citric acid (CA) was dissolved in 100 ml of deionized water (0.8 mol L^{-1}) at room temperature under constant stirring speed. Stirring was continued for another 10 min to obtain a homogeneous CA solution and then 0.2 mol L^{-1} of $HfCl_4$ was added to this solution. The molar ratio of Hf^{4+} ions and CA was 1:4, respectively. Stirring was continued at room temperature for 10 min to dissolve the $HfCl_4$ and to obtain a homogeneous precursor metal-citric complexes solution. Then 5 mL of conc. HNO_3 and 11.5 mL of 26 % NH_4OH were added to this complex solution. The molar ratio of NH_4OH and HNO_3 was 1:1, respectively. The resulting reaction mixture was stirred at room temperature for 10 min and the pH was measured to be 7. A colorless, clear reaction mixture was obtained and then this mixture was heated at 100 ℃ until intense gas evolution was observed and dark brown gel was formed. The resulting dark gel was then placed in a preheated vertical muffle furnace and the solution combustion synthesis (SCS) reaction was carried out at 300 ℃ until a rapid gas evolution and self-ignition process was observed. After SCS, the obtained powder sample was calcined at 800 ℃ for 2 hours with a heating rate of 5 °C min^{-1} in an air atmosphere.

For 5 atom% Eu^{3+}-doped HfO_2 nanomaterials the appropriate amount of Eu^{3+} ion solution was added dropwise to the hafnium citrate complex solution before the addition of conc. HNO_3 and 26 % NH_4OH,

Hydrothermal synthesis (HYT) $HfCl_4$ was dissolved in 20 ml of deionized water (0.2 mol L^{-1}) at room temperature under constant stirring speed. 25 % of NH_4OH was added to the Hf^{4+} ion solution at a rate of 0.05 mL min^{-1} under constant stirring. The hydrothermal reaction was carried out at 120 ℃ for 72 hours in a laboratory heating-drying oven. The reaction mixture was naturally cooled down to room temperature after. The nanomaterials in the sol were separated from the solvent by centrifugation for 15 min at 9000 rpm and purified by washing with deionized water and EtOH a total of seven times. The resulting wet sample was dried for 1 hour in a laboratory heating-drying oven at 120 ℃ and calcined at 800 ℃ for 2 hours with a heating rate of 5 °C min^{-1}.

For 5 atom% Eu^{3+}-doped HfO_2 before the addition of EG/NH_4OH/Gly, Eu^{3+} ion solution was added to the Hf^{4+} ion solution, with stirring continued for 10 minutes before the addition of NH_4OH.

Precipitation synthesis (PRE) The precipitation synthesis method of non-doped and doped HfO_2 nanomaterials. In the beginning, the two different solutions were prepared by separately dissolved $HfCl_4$ in 50 mL deionized water (0.4 mol L^{-1}) and KOH in 50 mL deionized water (0.16 mol L^{-1}) at room temperature under constant stirring speed. After dissolving completely, the hydroxide ion solution was slowly added to the hafnium ion solution at a rate of 0.83 mL min^{-1} under constant stirring speed. The molar ratio of Hf^{4+} ions and hydroxide ions was 1:4, respectively. The precipitation (PRE) reaction was carried out at room temperature under constant stirring speed for 24 hours. After the reaction, the nanomaterials in the sol were separated from the solvent by centrifugation for 15 min at 9000 rpm and purified by washing with deionized water and EtOH a total of seven times. After that, the resulting white gel-like sample was dried for 24 hours at room temperature and large, hard and semi-transparent crystals were obtained, which, when crushed in an agate pestle. The powder sample was calcined at 800 ℃ for 2 hours with a heating rate of 5 °C min^{-1} in an air atmosphere.

For 5 atom% Eu^{3+}-doped HfO_2 nanomaterials, Eu^{3+} ion solution was added dropwise to the Hf^{4+} ion solution at room temperature under constant stirring speed before the addition of KOH. After the addition of both the Eu^{3+} ion ion solution, stirring was continued for 10 minutes to obtain a homogeneous metal ion solution, and then KOH solution was added.

Characterization

The crystalline structure of the samples was determined by X-ray diffraction (XRD) using an X-ray diffractometer (X'Pert Pro MPD) with Cu-Kα radiation (λ= 1.54 nm). Crystalline sizes were determined from XRD data using the Scherrer equation.

Luminescence measurements were performed using a YAG laser FQSS266 (CryLas GmbH) 4th harmonic at 266 nm (4.66 eV) at room temperature. All samples were pressed into tablets of equal size, which allowed for intensity comparison between the samples. The luminescence spectra were recorded using an Andor Shamrock B-303i spectrograph equipped with a CCD camera (Andor DU-401A-BV).

The TL measurements were done with Lexsyg Research TL/OSL reader from Freiberg Instruments with samples being irradiated by X-rays for 30 min before measuring TL.

The crystalline size verification and morphology studies were performed using a transmission electron microscope (TEM, Tecnai G20, FEI) operated at 200 kV.

4.3.3 Results and discussion

Based on the need for the samples to have similar characteristics to ensure comparability and luminescent probes being affected more by the concentration of oxygen vacancies than the phase [62, 149], the parameters of the synthesis methods were adjusted to achieve a monoclinic phase for all samples.

Samples from here on will be referred to as SG-PC (sol-gel polymerized complex), SG-G (sol-gel glycine), SG-U (sol-gel urea), CO-UH (combustion urea, HMTA), CO-U (combustion urea), CO-H (combustion HMTA), AIC (auto-ignition combustion), HYT (hydrothermal), PRE (precipitation).

X-Ray diffraction

Figure 4.27 shows the results of X-ray diffraction measurements for the undoped nanocrystalline HfO_2 samples. Some of the undoped hafnia samples show traces of tetragonal phase, however precise percentages are below the limit of detection. The Eu doped samples showed a tetragonal phase ranging from 6.48% to 9.1% in the overall phase distribution according to the Rietveld refinement results. The larger fraction of the tetragonal phase found in the Eu doped samples is expected, as the incorporation of Eu^{3+} ions in the HfO_2 matrix creates oxygen vacancies that tend to stabilize the tetragonal phase at room temperature [8]. However no correlation was found between the percentage of tetragonal phase present in the Eu samples and the performed PL and TL measurements.

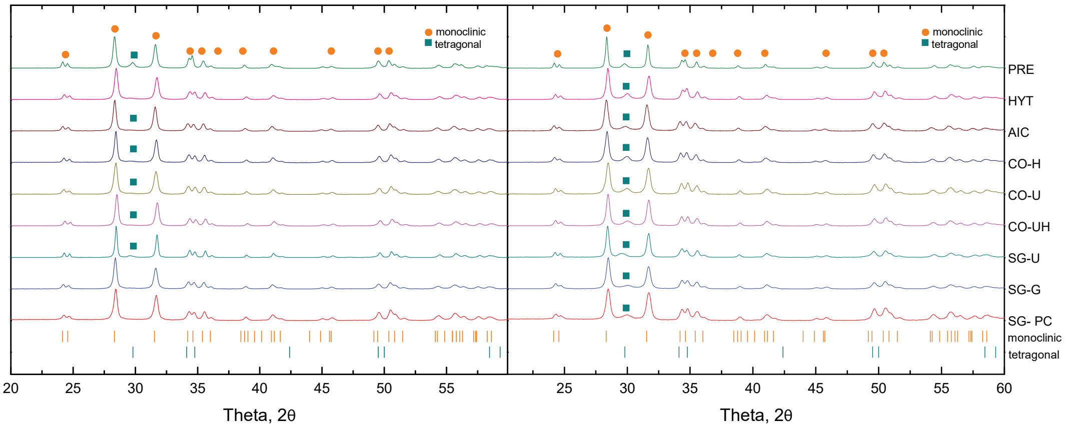

Figure 4.20: X-Ray diffraction pattern for undoped (left) and Eu doped (right) hafnia samples.

Additionally, crystallite size was determined for all samples using the Scherrer equation. The determined crystallite sizes can be seen in Table 4.7. During the various synthesis, the synthesis parameters were adjusted with the purpose of achieving similar grain sizes in order to ensure that the size and the resulting surface to volume ratios would not create a significant impact on other properties.

Table 4.3: Grain sizes in nm for undoped HfO_2 and Eu^{3+} doped HfO_2

	SG-PC	SG-G	SG-U	CO-U	CO-H	CO-UH	AIC	HYT	PRE
HfO_2	18.6	22.8	24.1	37.3	17.3	25.4	16.1	14.1	26.4
Eu	22.6	26.2	32.4	28.0	23.9	27.0	25.4	28.0	40.4

Photoluminescence

Photoluminescence spectra were measured for the undoped and Eu doped nanoparticles excited by a 4.66 eV laser (Fig.4.21). The normalized photoluminescence spectra for the undoped samples Figure 4.21(left) show slight differences in the slopes of the peaks. AIC and CO-H samples show a more intense slope on the lower energy side with their peak maxima also shifted to slightly lower energies, while CO-UH, HYT and PRE samples showed small changes in the shape of the peak closer around maxima on the higher energy side and had their maxima shifted to slightly higher energies. The maxima are located between 2.36-2.41 eV for all spectra however no correlation between the precise maxima and other parameters was found.

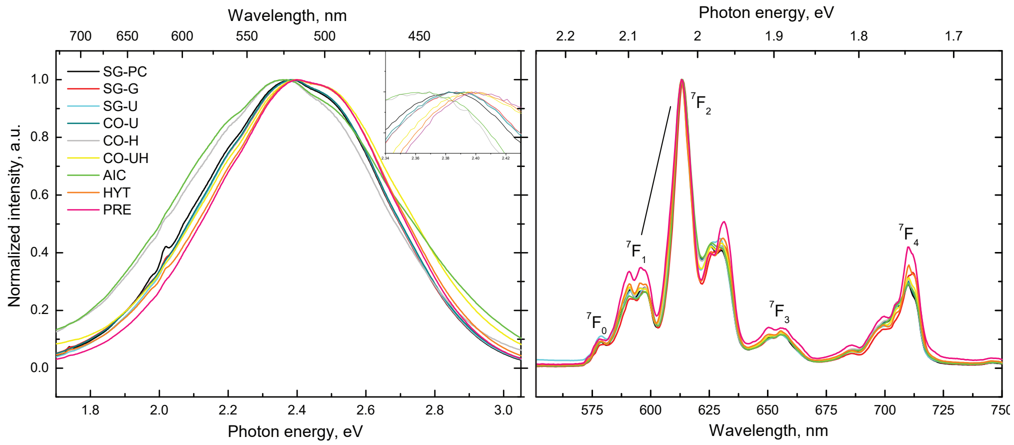

Figure 4.21: Photoluminescence spectra for the undoped HfO_2 samples (left) and Eu doped HfO_2 (right).

HfO_2:Eu sample spectra can be seen in Figure 4.21(right). As magnetic dipole transitions ($^5D_0 \rightarrow ^7F_1$) are assumed to be unaffected by local crystal fields (as opposed to the electric dipole transition $^5D_0 \rightarrow ^7F_2$) [89, 165], a local symmetry evaluation using the ratio of the electric dipole and magnetic dipole intensities can be carried out. The highest asymmetry ratios were seen for the samples AIC, SG-G and SG-PC, while the lowest were for the samples PRE, HYT and CO-H.

Intrinsic defect parameter evaluation

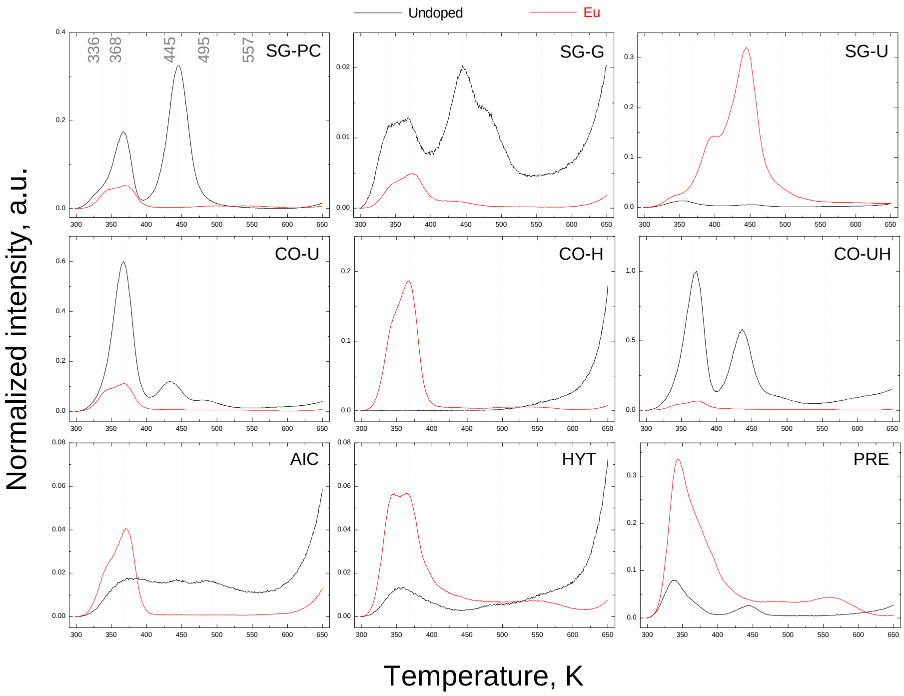

Figure 4.22: Thermoluminescence glow curves for undoped HfO_2 (black line) an 5 at% Eu doped (red line) samples with intensities normalized against the maximum value (undoped CO-UH).

Figure 4.22 shows TL glow peaks for undoped and 5 at% Eu doped samples after a 30 minute irradiation with X-rays. The peaks were registered at 550 nm for the undoped samples and 613 nm for the Eu doped samples. As photons in a similar mechanism to photoluminescence after the initial excitation via thermostimulation, the shown TL curves were corrected according to the PL intensities of the samples. Additionally, the TL curves were normalized with respect to the most intense TL peak (CO-UH undoped sample) in order to not lose information on the relative intensities of the peaks.

Multiple peaks in the glow curves signify the presence of traps with different activation energies. The shape of the TL curves does not allow to state unambiguously that peaks are of the first order kinetics and therefore second order kinetics were used to ensure consistency and avoid mixed order kinetics [54]. The activation energies were evaluated using second order glow-curve deconvolution functions developed by Kitis et al. [211] and are shown in Equation 4.7. The frequency factor for all glow curves was chosen to be $s = 10^{-12}$ as the approximate typical lattice vibration frequency of HfO_2 [54].

$$I_m = n_0 exp\left(\frac{E}{kT_m}\right)\left[\frac{skT_m^2}{\beta E} \times exp\left(-\frac{E}{kT_m}\right)(1-\Delta_m)+1\right]^{-2} \tag{4.7}$$

where $\Delta_m = 2kT_m/E$, I_m is the glow peak intensity, E (eV) the activation energy, s

(s^{-1}) the frequency factor, n_0 the initial concentration of trapped carriers, k (eV K^{-1}) the Boltzmann constant, T_m (K) the absolute temperature of the peaks.

The obtained trap activation energies are shown in Table 4.4. It can be seen that largely there are five different traps located at energies:

1) 0.89 - 0.96 eV (336 K)
2) 1.00 - 1.08 eV (368 K)
3) 1.20 - 1.24 eV (445 K)
4) 1.35 - 1.40 eV (495 K)
5) 1.44 - 1.55 eV (557 K)

Table 4.4: Trap activation energies for undoped HfO_2 and Eu doped samples, eV

	Undoped				Eu			
SG-PC	0.89	1.00	1.23		0.95	1.02		1.54
SG-G	0.94	1.03	1.22	1.35	0.94	1.03	1.22	
SG-U	0.95	1.02	1.24		0.94	1.08	1.23	1.48
CO-U		1.01	1.24	1.35	0.96	1.00	1.20	1.44
CO-H					0.95	1.01		1.47
CO-UH		1.01	1.21	1.40	0.95	1.04	1.22	1.50
AIC		1.05	1.20	1.35	0.94	1.01		
HYT	0.94	1.01	1.11	1.38	0.95	1.04		1.50
PRE	0.92	1.02	1.23		0.95	1.06		1.55

Theoretical studies provide valuable insights into trap activation energies of oxygen vacancies as well as defect formation energies. Although the seminal work of Foster et al. [17] had undervalued the band gap of HfO_2 (3.92 eV for the monoclinic phase), resulting in traps being located too close to valence band, when corrected for more recent theoretical values of the band gap (5.75 eV for the monoclinic phase), the values obtained are 1.10 eV for VO_3^{2+} and 0.93 eV for VO_3^{1+} and 1.43 eV for VO_4^{2+} and 1.44 eV for VO_4^{1+}. No electron affinity values for VO_3^0 and VO_4^0 were given by Foster.

Defect formation energies in undoped HfO_2 are provided by another seminal study by Zheng et al [21] and Chimata et al. [22]. While Chimata largely confirms the calculations of Zheng, only Zheng provides formation energies for VO_3 and VO_4 separately.

Zheng reports 1.12 eV, -—1.66 eV, -—4.83 eV and 0.98 eV, -—1.39 eV, -—4.20 eV for VO_3^0, VO_3^{1+}, VO_3^{2+} and V_{O4}^0, VO_4^{1+}, VO_4^{2+} under oxygen poor conditions respectively. A similar trend is seen under oxygen rich conditions, however the defect formation energies being higher with 0.81 eV and 1.44 eV for VO_3^{2+} and VO_4^{2+} respectively.

Based on these studies we propose the following assignment of defect types to the obtained TL curves:

1) 0.89 - 0.96 eV (336K) - VO_3^{1+}

The theoretical trap depth is 0.93 eV [17]. We obtained values in the range of 0.89 - 0.96 eV. Due to the "negative U" tendency of oxygen vacancies and VO_3^{1+} not being stable against disproportionation into VO_3^0 and VO_3^{2+} [17, 21, 22], it is expected for there to be only a small amount of these defects found in undoped hafnia. This corresponds to the low 336 K TL peak intensity seen in the undoped samples and the increase of the peak intensity in Eu doped samples when the "negative U" tendency is disrupted.

2) 1.00 - 1.08 eV (368K) - VO_3^{2+}

The theoretical trap depth is 1.10 eV[17]. We obtained values in the range of 1.00 - 1.08 eV. Although the energy ranges do not correspond within the necessary range, we base this proposition on the observation that the the electron affinity for VO_3^{2+} is the most favorable and it is the most intense TL peak in the majority of the undoped samples as well as Eu doped samples.

3) 1.20 - 1.24 eV (445K) - $VO_4^{1+} + VO_4^{2+}$

The theoretical trap depth is 1.44 and 1.43 eV for VO_4^{1+} and VO_4^{2+} correspondingly [17]. We obtained values in the range of 1.20 - 1.24 eV. Here the difference between the theoretical values and the ones we have obtained is significant. However, based on the electron affinity being the second most favorable among VO_3 and VO_4 defects corresponding with the intensities of TL peaks and the already seen underestimation of trap depth with the previous defect type, the authors believe this to be the $VO_4^{2+} + VO_4^{1+}$ defect peak. The difference between the theoretical values and our experimentally obtained ones might be explained by being due to Foster et al. using the theoretical band gap of 3.95 eV instead of 5.75 eV as has been calculated in more recent studies or a different frequency factor needing to be used for these traps (at $s = 10^{-14}$ the obtained trap values are in the ranges 1.37-1.41 eV).

4) 1.35 - 1.40 eV (495 K)

Seen only in the undoped samples, it is possible that these might be oxygen interstitials O^0 as Zheng [21] provides point defect formation energies of 7.22 eV and 1.58 eV under oxygen poor and rich conditions respectively. Foster gives a corrected trap depth of 2.12 eV.

5) 1.44 - 1.55 eV (557 K) The peak overall is of very low intensity and found only in Eu doped samples. It is possible that this peak belongs to hafnium interstitials which appear when Eu^{3+} is introduced, however we do not speculate on this further.

Temperature dependant behaviour

For all samples PL peak maxima exhibit a shift to lower energies with an average of 0.06 eV when measured at a temperature of 10 K. This might be explained by non-radiative transitions to a higher energy level when measured at room temperature. The PL spectra of the undoped SG-PC sample measured at room temperature and 10 K are shown in Figure 4.23.

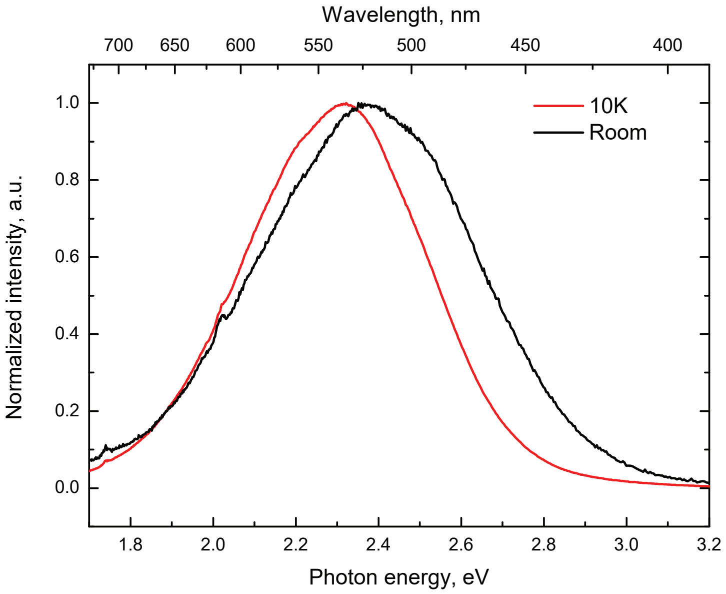

Figure 4.23: Spectra of the undoped SG-PC sample at room temperature and at 10 K.

Similar to PL spectra at 10 K and room temperatures, low temperature TL wavelength spectra also show a tendency to shift the peak maxima to higher energies at increasing temperatures. Figure 4.24 shows TL spectra peak position shift with the corresponding TL glow peaks for samples SG-PC, SG-G, PRE, CO-U and CO-UH. The rest of the samples exhibited a signal-to-noise ratio that was too low for meaningful analysis.

However, it can be seen that the process is not straightforward and the more significant shift to higher temperatures happens around the same temperatures (although preceding the glow peaks by around 50 K) at which the TL glow peaks increase in intensity, signifying an unknown underlying mechanism to play a part in the resulting processes that require further studies.

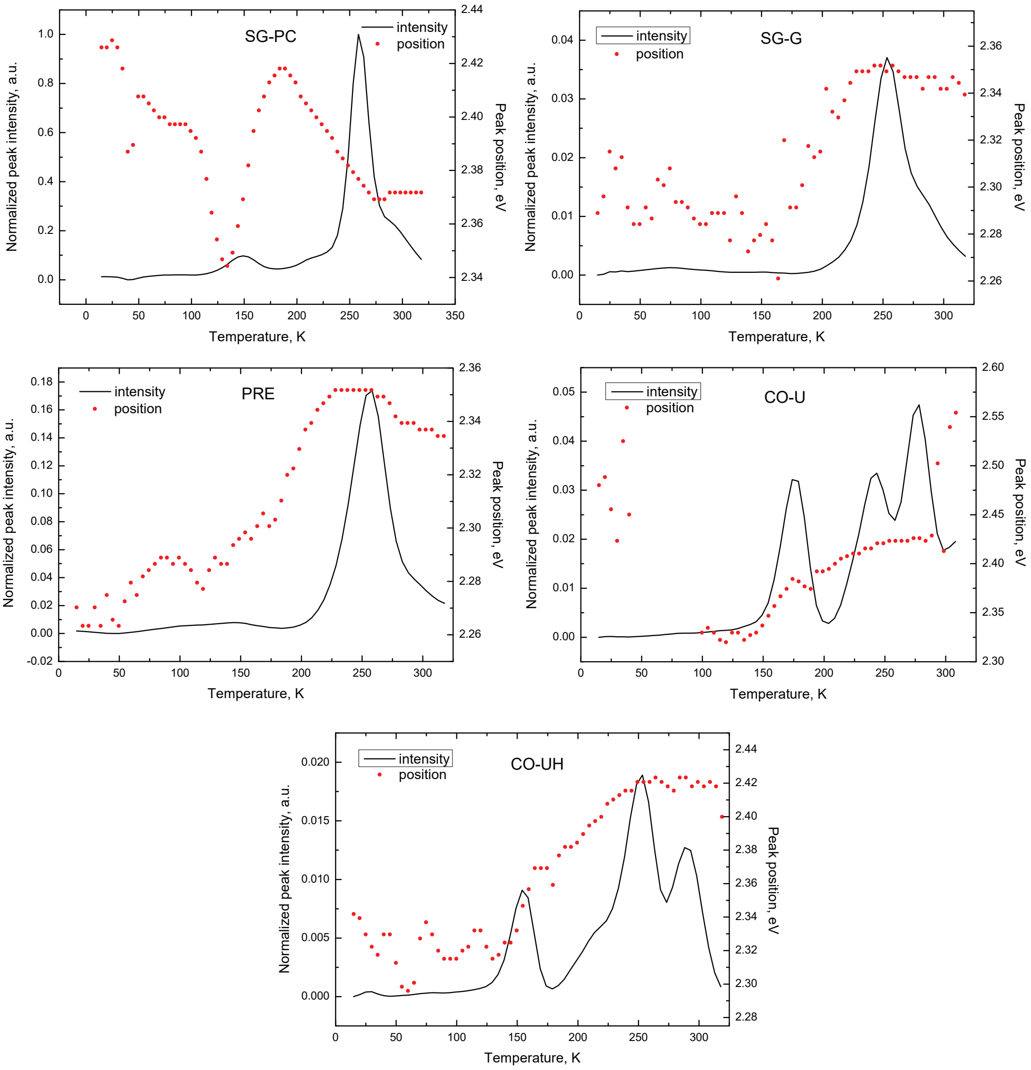

Figure 4.24: TL glow peaks (intensity) and TL spectrum peak position (eV) dependence on temperature for samples SG-PC, SG-G, PRE, CO-U and CO-UH.

The calculated trap depth energies for can be seen in Table 4.5. The samples not included in this table did not have sufficient TL intensity. Due to a lack of both theoretical and experimental data, we do not speculate on the precise nature of these defects apart from them probably being more surface related than the above room temperature defects.

Table 4.5: Trap activation energies for undoped samples below room temperatures (eV)

Sample	150K	210K	250K	290K
SG-PC		0.58	0.71	0.82
SG-G		0.6	0.68	0.78
CO-U	0.47	0.61	0.66	0.76
CO-UH	0.41	0.59	0.68	0.79
PRE		0.6	0.7	0.8

The phenomenon is further observed when the TL wavelength spectra at higher temperatures are considered. For all undoped samples except AIC the peak maximum of the room temperature photoluminescence spectrum is located at lower energies than the TL wavelength spectra maximums (Fig. 4.25. This might be partially explained by the non-radiative transitions happening at increasing temperatures, however not fully.

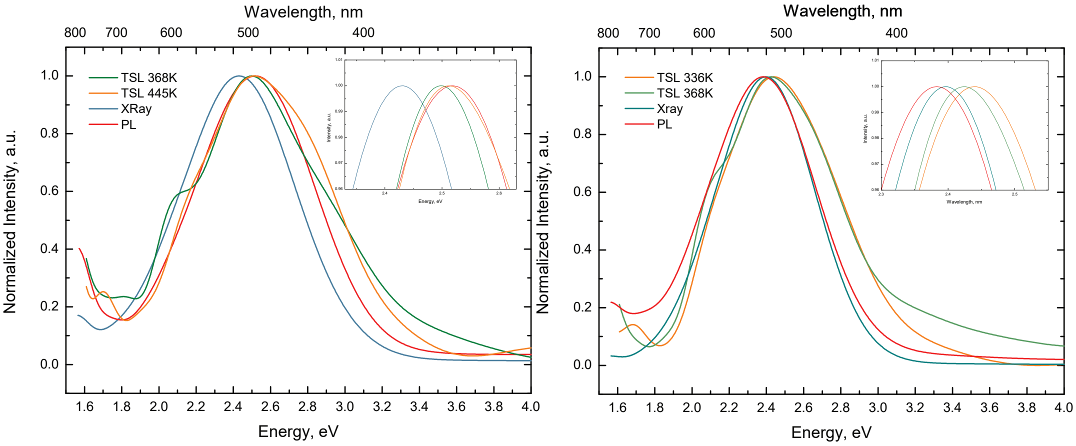

Figure 4.25: TL and Xray peak maximuma in regard to the PL maximum; (left) - sample AIC with TL and X-ray spectra energies are located at lower values than the PL peak, (right) - sample SG-U where the opposite is seen

In addition to TL and PL peak shifts, XRL measurements at room temperature were performed. It can be seen that when the PL spectra is located at lower energies than TL spectra, the same is true for XRL spectra and vice versa when PL peak is located at higher energies than TL spectra, XRL peak is located at lower energies as well. A possible factor of the additional peak shift might be due to PL spectra having a larger interaction with the surface of the particles where the grain boundaries exhibit a larger amount of defects such as oxygen vacancies and are more amorphous thus lowering the band-gap.

To further expand on this factor, the authors turn to TEM images. TEM images for undoped SG-PC, SG-G, SG-U, AIC, PRE and CO-UH samples can be seen in Figure 4.26. It can be seen that the sample AIC for which PL peak was higher than TL and XRL peaks is highly crystalline near grain boundaries and shows no signs of an amorphous phase, however, samples SG-U and PRE also show similar characteristics while their PL peaks were located at lower energies. Other samples show significant amounts of an amorphous phase near the grain boundaries. Although most samples seem to confirm the influence of grain boundary and surface defects on the resulting photoluminescence peak position, the exceptions show that the resulting PL peak shift is a result of several factors, possibly only a couple of them being the amount of amorphousness on grain boundaries and non-radiative transitions.

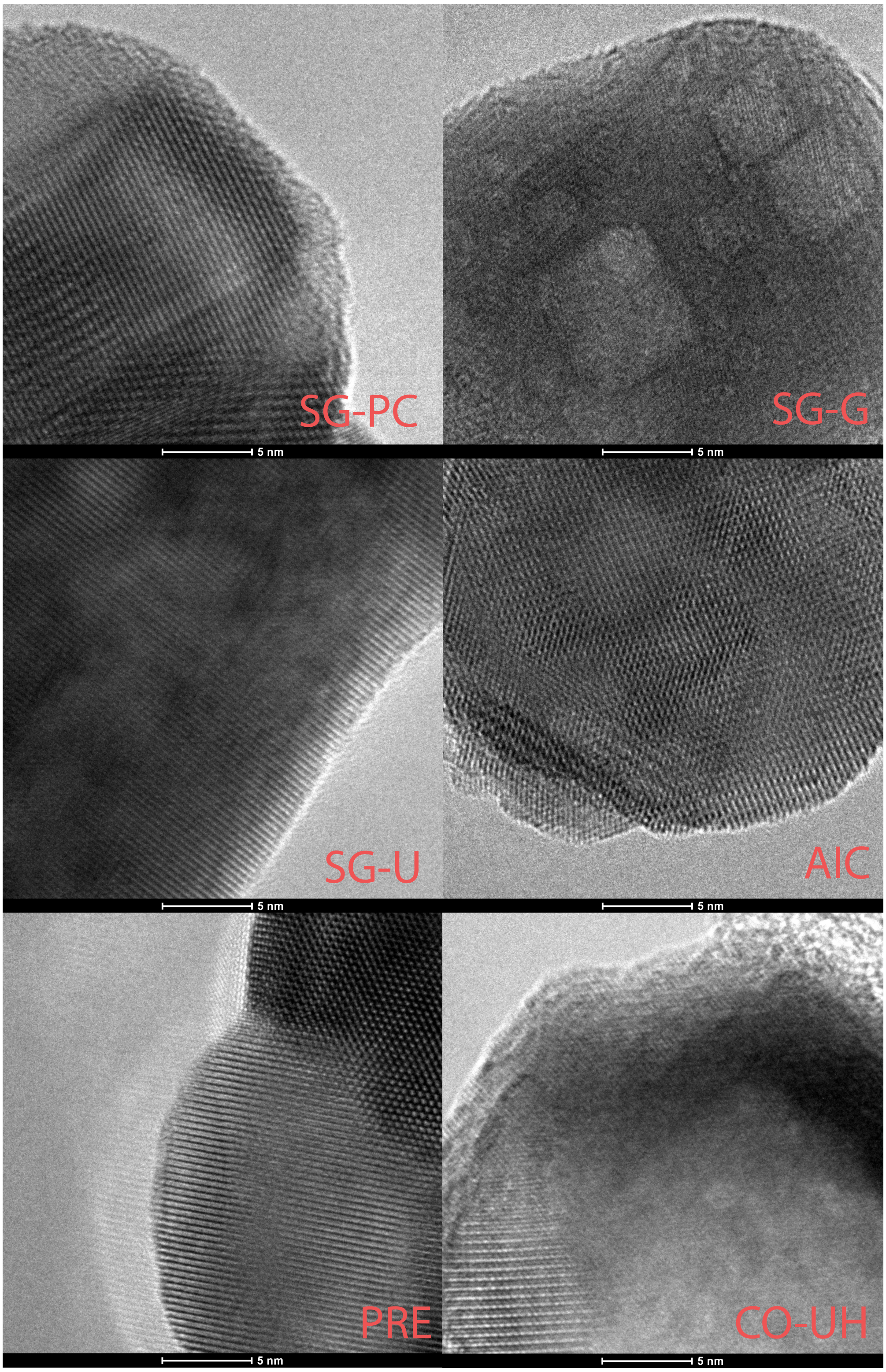

Figure 4.26: TEM images of the undoped HfO_2 samples SG-PC, SG-G, SG-U, AIC, PRE and CO-UH

Sample correlation patterns

In order to exclude other factors such as grain size from the obtained PL and TL data analysis as well as gain understanding on whether any correlation exists between different characteristics, the authors evaluated the obtained data using the Pearson correlation coefficient (with $p<0.05$) and manually assessed for circumstantial outlier errors.

The initial chosen characteristic parameters were: Integrated PL intensity, integrated above room TL intensities, integrated below room temperature TL intensity, grain size, TL peaks at 150K, 258K, 340 K, 370 K, 450 K, PL peak intensities and peak positions at 10K and ambient temperatures, phase composition (% of tetragonal phase). No significant correlations were found.

4.3.4 Conclusions

For the first time a thorough experimental study of the possible intrinsic defects originating in hafnia has been performed. Trap depths for VO_3^{1+}, VO_3^{2+}, VO_4^{1+}, VO_3^{2+} oxygen vacancies were evaluated from above room temperature TL data. Below room temperature TL measurements were also performed with further studies needed to determine the trap origin.

Possible non-radiative transition phenomena was observed with PL and TL wavelength spectra shifting to higher energies with increasing temperatures.

Additionally when PL spectra was compared to TL wavelength spectra a potential indication of direct surface defect contribution to the resulting PL spectra was observed in both TL, XRL spectra and TEM images.

4.3.5 Thesis 3

Different types of oxygen vacancies in monoclinic HfO_2 have been successfully identified by studying undoped and europium-doped samples and their thermoluminescence spectra. The experimentally identified vacancy characteristics strongly correlate with the theoretical calculations discussed both in this study and section 2.2.1, confirming that the identification of oxygen vacancies using thermoluminescence is a valid and reliable method.

Thesis 3: Single (+1) and double (+2) charged oxygen vacancies at 3-fold coordinated (VO_3^{1+}, VO_3^{2+}) and 4-fold coordinated (VO_4^{1+}+VO_4^{2+}) sites of monoclinic HfO2 can be identified by thermoluminescence.

4.4 Europium ion incorporation characteristics in HfO_2

Hypothesis 4:

A hypothesis is put forward that in monoclinic HfO_2, Eu^{3+} ions tend to incorporate in pairs as well as single ions, creating VO_3^{2+} and VO_3^{1+} oxygen vacancies. In order to prove this hypothesis, undoped and europium doped hafnia samples are synthesized and their characteristics analyzed. By using the information on the types of oxygen vacancies identified in thermoluminescence data acquired in the previous study, a further study on the properties of rare-earth ion incorporation into the host matrix is performed.

4.4.1 Introduction

Hafnium dioxide (HfO_2) is a versatile and promising material with a wide range of potential applications in fields such as engineered ceramics, electronic materials, optoelectronics, solid electrolytes, ferroelectric devices etc., due to its impressive physical and chemical properties. These properties include high chemical and thermal stability, strong mechanical resistance, a high melting point of 2800°C, and high phase transition temperatures, making it an ideal material for use in high-temperature refractory applications, such as thermal oxidation protection layers and thermal barrier coatings [212–215].

Hafnia has also gained popularity as a high dielectric gate material for CMOS applications due to its favorable characteristics, including a broad bandgap of 5.25-5.95 eV and a high-k value of 25 [22, 196]. It has become the preferred alternative to SiO_2 as technology continues to reduce in size, as the low dielectric constant of SiO_2 resulted in leakage currents that hindered further downsizing [197, 198, 200].

Rare-earth ions are often used as luminescent probes to investigate the local structure of the system in which they are embedded, due to the well-defined electronic levels determined by their $4f^n$ electronic configuration [62, 86, 89, 90, 149] and the shielding effect provided by the $5s$ and $5p$ electronic shells to the $4f$ electrons [87]. However the characteristics and effect of Eu^{3+} ion incorporation into metal oxides from the experimental point of view have not been thoroughly investigated.

Therefore in this work we examine the properties of hafnia synthesized by various methods with an emphasis on the study of defects and the mechanisms of Eu^{3+} incorporation into the host lattice. X-Ray diffraction, photoluminescence, luminescence decay kinetics and thermoluminescence measurements were performed in order to analyze the obtained samples.

4.4.2 Materials and methods

See Section 4.3.2 for the full list of chemicals used. Additonally, Niobium pentachloride ($NbCl_5$, purity 99 %) was used for the Nb doped samples, purchased from Alfa Aesar, Germany.

The synthesis process is described in detail in Section 4.3.2. An additional step of adding niobium to the sol-gel and combustion methods was performed:

Sol-gel (SG):

For 5 atom% Eu^{3+}-doped HfO_2 and 5 atom% Eu^{3+}, 5 atom% Nb^{5+}-doped HfO_2 nanomaterial synthesis Eu^{3+} and Nb^{5+} ion solution was added dropwise to the Hf^{4+} ion solution and stirred for 10 min before the addition of urea.

Combustion (CO):

For 5 atom% Eu^{3+}-doped HfO_2 and 5 atom% Eu^{3+}, 5 atom% Nb^{5+}-doped HfO_2 nanomaterials, the appropriate amount of Eu^{3+} and Nb^{5+} ion solution was added dropwise to the Hf^{4+} ion solution under constant stirring speed before the addition of urea/HMTA.

Characterization methods and parameters are described in Section 4.3.2.

4.4.3 Results and discussion

Although previous studies suggest that a more intense luminescence can be attained for tetragonal HfO_2, more recent studies have shown that the luminescence intensity is not as dependent on the phase of the material as it is on the distribution of oxygen vacancies [62, 149]. Based on this knowledge, the parameters of the synthesis methods were adjusted to achieve a monoclinic phase for all samples for the purpose of comparability.

X-Ray diffraction

Figure 4.27 shows the results of X-ray diffraction measurements for the Eu and Eu,Nb doped HfO_2 samples. One of the undoped hafnia samples (CO-H) showed traces of tetragonal phase (2%), with the rest of the undoped samples being >99% monoclinic. The Eu doped samples showed a tetragonal phase ranging from 6.03% to 9.09% in the overall phase distribution, with Eu,Nb doped samples ranging from 0.74% to 4.39% according to the Rietveld refinement results. The larger fraction of the tetragonal phase found in the Eu doped samples is expected, as the incorporation of Eu^{3+} ions in the HfO_2 matrix creates oxygen vacancies that tend to stabilize the tetragonal phase at room temperature [149]. However no correlation was found between the percentage of tetragonal phase present in the Eu and Eu,Nb samples and the performed PL and TL measurements in this study.

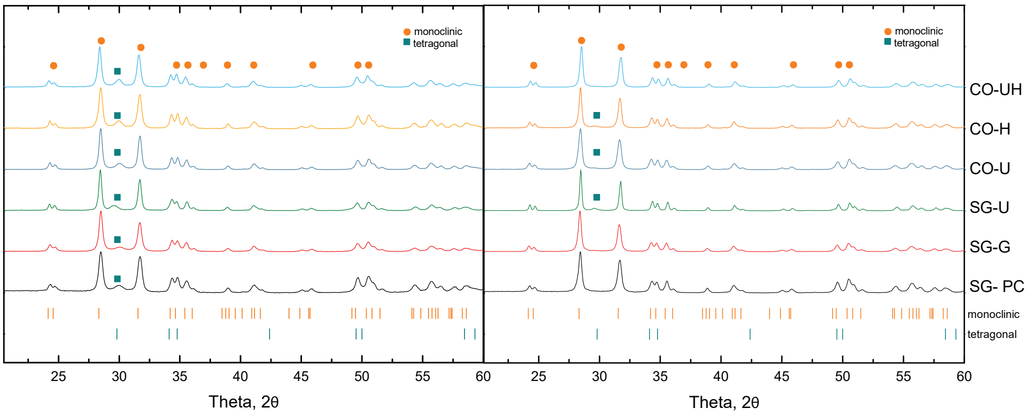

Figure 4.27: X-Ray diffraction pattern for Eu doped (left) and Eu,Nb doped (right) hafnia samples.

It must also be noted that it is difficult to determine whether the additional phase is tetragonal or cubic. According to [8], when HfO_2 is doped with ions that have a larger radius than Hf^{4+}, the phase tends to be cubic rather than tetragonal, however Rietveld refinement indicated the phase to be tetragonal for the doped samples. Additionally, there can be seen a visual peak shift for the tetragonal peak located at around 30 2ϑ from 29.5 2ϑ to 30.0 2ϑ which is perhaps an indication of mixed cubic and tetragonal phases. The percentages of monoclinic and tetragonal phases can be seen in Table 4.6.

Table 4.6: Monoclinic and tetragonal phase Rietveld analysis of undoped, Eu and Eu, Nb doped samples.

	Undoped		Eu		Nb	
	M, %	T, %	M, %	T, %	M, %	T, %
SG-PC	99.98	0.02	91.94	8.06	99.26	0.74
SG-G	99.54	0.46	93.97	6.03	98.90	1.10
SG-U	99.73	0.27	93.52	6.48	95.61	4.39
CO-U	99.55	0.45	92.54	7.46	98.93	1.07
CO-H	97.90	2.10	91.26	8.74	98.76	1.24
CO-UH	99.35	0.65	90.91	9.09	97.76	2.24

Additionally, the crystallite size was determined for all samples using the Rietveld refinement. The determined crystallite sizes can be seen in Table 4.7. During the various synthesis, the synthesis parameters were adjusted to achieve similar crystallite sizes to ensure that the size and the resulting surface-to-volume ratios would not significantly impact other properties. It can be seen that when doped, the crystallite sizes also tend to increase in size.

Table 4.7: Crystallite sizes determined by Rietveld refinement(nm).

Sample	Undoped	Eu	Eu,Nb
SG-PC	18.6	22.6	28.0
SG-G	22.8	26.2	30.0
SG-U	24.1	32.4	42.5
CO-U	37.3	28.0	31.2
CO-H	17.3	23.9	26.2
CO-UH	25.4	27.0	32.4

Photoluminescence

Photoluminescence spectra were measured for the undoped, Eu doped and Eu,Nb doped nanoparticles excited by a 4.66 eV laser. The PL spectra for the undoped samples showed the typical broad peak with maxima being located between 2.36 - 2.41 eV. No correlation between the position of peak maxima and other parameters were found.

Photoluminescence spectra for samples doped with Eu and Eu,Nb are presented in Figure 4.28. Both Eu and Eu,Nb spectra show the characteristic Eu^{3+} ion luminescence, indicating proper incorporation of Eu^{3+} ions into the HfO_2 matrix.

As magnetic dipole transitions ($^5D_0 \rightarrow {}^7F_1$) are assumed to be unaffected by local crystal fields (as opposed to the electric dipole transition $^5D_0 \rightarrow {}^7F_2$) [89, 165], a local symmetry evaluation using the ratio of the electric dipole and magnetic dipole intensities was carried out.

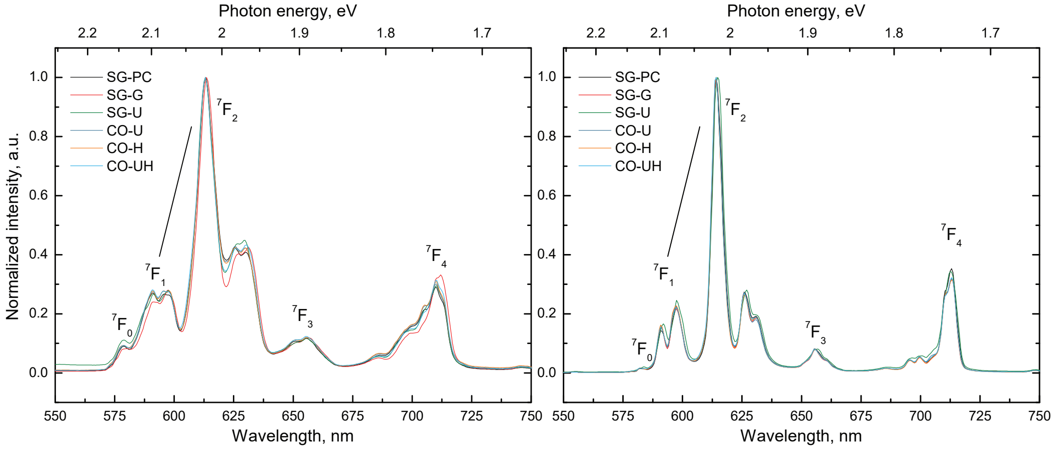

Figure 4.28: Photoluminescence spectra for Eu doped samples (left) and Eu,Nb doped samples (right).

The general pattern observed from these spectra is the highly increased asymmetry when samples are additionally doped with Nb^{5+} ions. Therefore it can be reasoned that although the Nb^{5+} ions compensate the charge disparities caused by Eu^{3+} ion incorporation and lower the amount of oxygen vacancies present in the material (discussed in section 4.4.4), the overall asymmetry of the Eu^{3+} sites is increased. Smits et al. presents a possible mechanism of Nb ion incorporation in similar conditions in [149].

Time resolved luminescence and Judd-Ofelt parameters

Figure 4.29 shows the time-resolved luminescence measurements for Eu and Eu,Nb doped samples at 613 nm. It can be seen that for samples doped additionally with Nb, the decay rate is slower than for only Eu doped samples. For Eu doped samples, SG-G shows the slowest decay rate, while luminescence for samples SG-U and CO-H decays faster. The decay rates showed a complex nature and were approximated using a double exponent to separate the fast and slow decay rates.

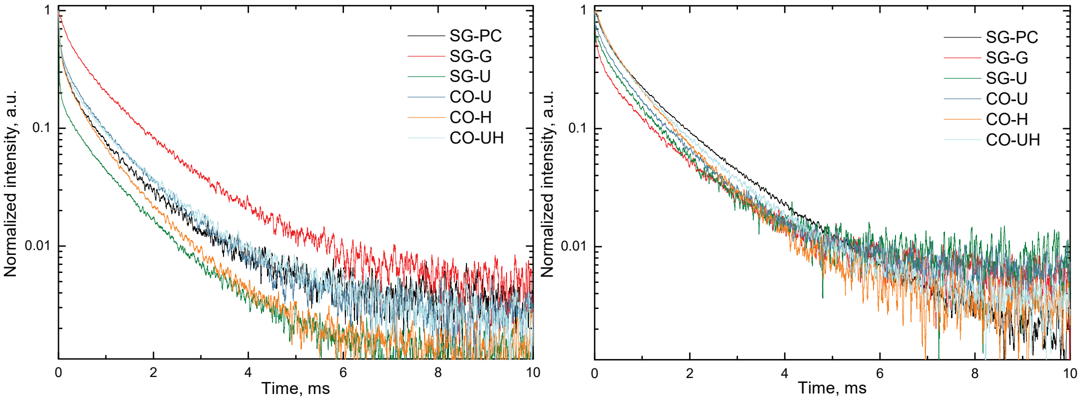

Figure 4.29: Time resolved luminescence measurements for Eu doped samples (left) and Eu,Nb doped samples (right).

For the calculations of spontaneous emission probability and quantum efficiency Judd-Ofelt theory was applied to the emission spectra and the necessary parameters were calculated as is described in this paragraph. Due to the fact that for Eu^{3+} electric dipole $^5D_0 \rightarrow {}^7F_{2,4,6}$ transitions depend only on one squared reduced matrix element [216] , the experimental Ω_λ intensities can be calculated from the ratio of the single MD transition $^5D_0 \rightarrow {}^7F_1$ to ED transitions and are determined by the following formula[167]:

$$\Omega_\lambda = \frac{D_{md}\nu_1^3}{e^2\nu_\lambda^3}\frac{9n^3}{n(n^2+2)^2|\langle\Psi J||U^{(\lambda)}||\Psi' J'\rangle|^2}\frac{\int I_\lambda(\nu)d\nu}{\int I_1(\nu)d\nu} \tag{4.8}$$

where D_{md} is assumed to be 9.6 x 10^{-42} esu^2 cm^2 according to previous calculations [168]. e is the elementary charge 4.803 x 10^{-10} esu, n is the refractive index 2.08 [50] and $|\langle\Psi J||U^{(\lambda)}||\Psi' J'\rangle|^2$ are the squared reduced matrix elements for Eu^{3+} that are independent of the host material and have been taken from Ref.[216]. The results obtained from the calculations can be seen in Table 4.8. It can be seen that overall when samples are additionally doped with Nb^{5+} the emission quantum efficiency increases from an average

17.1% to 20.1%. This slight increase indicates that oxygen vacancies, created when doping with Eu^{3+}, lower the quantum efficiency of the material.

Table 4.8: Ω_2, Ω_4 JO parameters, experimental decay lifetimes (τ) for ${}^{5}\mathrm{D}_0 \rightarrow {}^{7}\mathrm{F}_2$, radiative transition rates (A_R), nonradiative rates (A_{NR}), emission quantum efficiency (η)

		Ω_2, 10^{-20}	**Ω_4, 10^{-20}**	**τ,μs**	**A_R**	**A_{NR}**	**η %**
Eu	**SG-PC**	5.27	2.91	739	227	1127	16.8
	SG-G	5.39	3.10	961	232	809	22.3
	SG-U	5.11	2.86	654	234	1296	15.3
	CO-U	5.10	2.96	682	224	1243	15.3
	CO-H	5.09	3.06	740	216	1136	16.0
	CO-UH	5.12	2.90	858	222	944	19.0
Nb	**SG-PC**	6.17	3.58	631	251	1335	15.8
	SG-G	5.98	3.31	854	244	927	20.8
	SG-U	5.69	3.46	1022	249	730	25.4
	CO-U	5.74	3.24	822	241	975	19.8
	CO-H	5.60	3.08	583	239	1476	13.9
	CO-UH	5.92	3.27	603	244	1414	14.7

4.4.4 Intrinsic defect parameter evaluation

Figure 4.30 shows TL glow peaks for undoped, 5 at% Eu doped and 5 at% Eu, 5 at% Nb doped samples after a 30 minute irradiation with X-rays. The TL curves were adjusted based on the PL intensities of the samples as it is believed that the photons are emitted in a mechanism similar to that seen in the photoluminescence process. To preserve information on the relative intensities of the peaks, the TL curves were additionally normalized in relation to the TL peak with the highest intensity (CO-UH undoped sample). It can be seen that as expected, when the samples are additionally doped with Nb^{5+}, the charge compensation reduces the amount of defects acting as traps as compared to undoped and Eu^{3+} doped samples. The Eu doped sample SG-U shows a significantly different behaviour from the rest of the samples. As this sample had used relatively larger amounts of urea during the synthesis, it is possible that some C or N impurities have remained in the final sample and this sample will not be taken into consideration in further analysis.

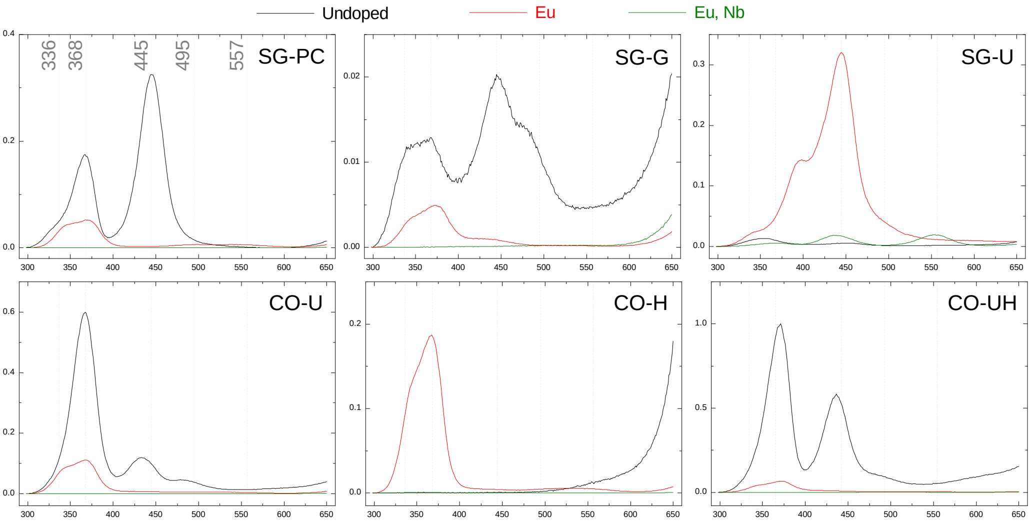

Figure 4.30: Thermoluminescence spectra for undoped HfO_2 (black line), 5 at% Eu doped (red line) and 5 at% Eu, 5 at% Nb doped (green line) samples with intensities normalized against the maximum value (undoped CO-UH).

A previous publication by Laganovska et al. identified various defect types and energy ranges. The traps at 336K, 368K and 445K were identified as a threefold coordinated oxygen vacancy VO_3^{1+}, a threefold coordinated oxygen vacancy VO_3^{2+} and the fourfold coordinated oxygen vacancies VO_4^{1+} together with VO_4^{+2} respectively.

In this study, two novel aspects on the nature of Eu^{3+} ion incorporation into monoclinic HfO_2 matrix is seen:

1) The VO_3^{1+} peak in undoped HfO_2 has a very low TL intensity as is expected due to the "negative U" tendency [18] to disproportionate into VO_3^{0} and VO_3^{2+} vacancies. However, when doped with Eu^{3+}, the VO_3^{1+} peak at 336K greatly increases in intensity. This indicates that contrary to the previous assumption by Smits et al.[149] that Eu^{3+} ions mostly incorporate themselves in the host matrix in pairs so that the resulting oxygen vacancy charge V_O^{2+} is compensated by two Eu^{3+} ions, a significant part of Eu^{3+} ions also incorporate themselves as single ions and create a stable VO_3^{1+} vacancy. An illustration is shown in Figure 8.

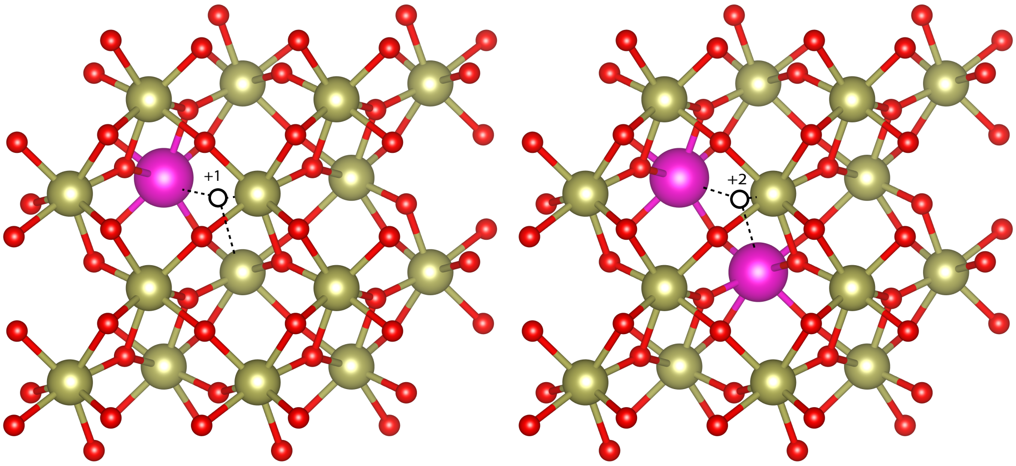

Figure 4.31: Possible incorporation of Eu^{3+} ions in the HfO_2 matrix, (left) a V_O^+ vacancy charge compensated by a single Eu^{3+}; (right) V_O^{2+} charge compensated by two Eu^{3+} ions.

2) The VO_4^{1+} and VO_4^{2+} peak at 445K for most undoped samples is the second or even first highest glow peak. However, when doped with Eu^{3+} ions this peak disappears almost completely. The effect of threefold coordinated vacancy creation preference has been discussed in theoretical calculations, where Foster et al. [18] notes that the total system energy is much lower (0.44 eV and 0.76 eV, respectively) for the threefold-coordinated site. This implies that although the formation of an initial neutral vacancy is energetically balanced between sites, once electrons are removed, the threefold coordinated oxygen vacancy is strongly favored for both VO_3^{1+} and VO_3^{2+}, and vacancies are likely to diffuse to these sites. It is therefore possible that when Eu^{3+} ions are incorporated into the matrix, the total system energy is lower when Eu^{3+} ions are located next to threefold coordinated oxygen vacancies and is thus the preferred site for Eu^{3+} ions as is seen in our experimental data.

4.4.5 Conclusions

HfO_2 doped with Eu^{3+} and Eu^{3+}, Nb^{5+} of monoclinic structure and crystallite sizes ranging between 17.3 nm and 42.5 nm has been studied. When doped with Nb, an expected decrease in the amount of oxygen vacancies is seen. Judd-Ofelt calculations confirm an increased emission quantum efficiency for samples doped additionally with Nb as compared to samples doped only with Eu.

The analysis of thermoluminescence data shows that a significant amount of Eu^{3+} ions are incorporated into the host matrix not only in pairs that balance out a V_O^{2+} vacancy, but also as single ions located next to a V_O^{1+} vacancy.

Eu^{3+} ion incorporation into the host matrix creates a significantly larger amount of threefold coordinated oxygen vacancies than fourfold coordinated oxygen vacancies. This finding agrees with theoretical calculations where the threefold coordinated oxygen vacancy has a much lower total system energy when electrons are removed. Therefore when Eu^{3+} ions are introduced, mainly threefold coordinated oxygen vacancies are created.

4.4.6 Thesis 4:

By analysing the thermoluminescene data of the undoped and europium-doped samples, it was seen that when Eu^{3+} is incorporated into the matrix, not only a V_O^{2+} vacancy is formed (signifying that the ions are incorporated into pairs), but a V_O^{1+} vacancy is formed as well. The V_O^{1+} vacancy is therefore hypothesized to be charge balanced by single Eu^{3+} ions, leading to the conclusion, that europium also incorporates in single ions. Additionally, a strong preference for threefold-coordinated oxygen vacancy formation is seen, providing valuable insight into the mechanism of rare-earth ion incorporation into metal-oxide materials in general.

Thesis 4: In monoclinic HfO_2, Eu^{3+} ions tend to incorporate in pairs as well as single ions, creating VO_3^{2+} and VO_3^{1+} oxygen vacancies.

5.SUMMARY

This work was focused on the study of defects in hafnia and zirconia nanoparticles and their influence on the various properties of these metal oxides, often using luminescent probes to gain additional insight into these materials.

An important drawback of introducing lanthanides into metal oxides are the oxygen vacancies created as a result of charge disbalance. To mitigate this issue, charge compensation in hafnia and zirconia was studied. It was shown to be a successful approach in reducing the amount of oxygen vacancies, which was observed through a decrease in thermoluminescence intensity and an increase in photoluminescence intensity. As a result, the quantum efficiency of these materials was significantly enhanced.

Even more important, while it was previously assumed that the phase of the host material largely determines the luminescence properties of the dopants, when charge-compensated, the luminescence intensity kept increasing even as the phase changed from tetragonal to monoclinic. This change suggested that the presence of oxygen vacancies is the primary cause of changes in luminescence intensity, rather than changes in the phase of the material and the resulting local crystal field.

This behaviour was shown to be true also with up-conversion luminescence. We observed luminescence quenching in ceramic samples when powders were pressed into pellets. By studying the differences in up-conversion luminescence spectra at different annealing temperatures, it was determined that the cause of the quenching could not be due to a change in lanthanide ion cross-relaxation efficiency as a result of phase change with applied pressure, but was yet again the impact of intrinsic defect creation.

Seeing as oxygen vacancies played a significant role in the resulting properties of metal oxides, it was necessary to carry out an in-depth research on the oxygen vacancies themselves. Through the use of thermoluminescence and the study of samples synthesized using various methods, threefold- and fourfold- coordinated, singly and doubly charged oxygen vacancies in hafnia were identified experimentally for the first time. These results enable an easier and more in-detail identification of oxygen vacancies in future studies.

Finally, although lanthanides are widely used as luminescent probes to carry out studies on the materials they are incorporated into, the nature of the incorporation of these ions had not been fully studied. Therefore, building on the knowledge gained while studying oxygen vacancies in hafnia, it was shown that the incorporation of lanthanide ions into the host matrix creates specifically threefold-coordinated oxygen vacancies which the ions then locate next to. It was also observed that lanthanide ions tend to incorporate into the matrix as both single ions and in pairs, which provides a key insight into the behavior of lanthanide ions in metal oxides.

6.THESES

Thesis 1: The luminescence intensity of rare-earth ions in HfO_2 is determined more by the vicinity and distribution of nearby oxygen vacancies than by phase transition from monoclinic to tetragonal.

Thesis 2: Erbium ion luminescence is an effective way of monitoring defect formation and phase transformation in nanostructured ZrO_2 ceramics during the sintering process.

Thesis 3: Single (+1) and double (+2) charged oxygen vacancies at 3-fold coordinated (VO_3^{1+}, VO_3^{2+}) and 4-fold coordinated (VO_4^{1+}+VO_4^{2+}) sites of monoclinic HfO2 can be identified by thermoluminescence.

Thesis 4: In monoclinic HfO_2, Eu^{3+} ions tend to incorporate in pairs as well as single ions, creating VO_3^{2+} and VO_3^{1+} oxygen vacancies.

7.LIST OF CONFERENCES AND PUBLICATIONS

7.1 Authors publications reflecting the thesis

Thesis 1:

1. Smits, K., Olsteins, D., Zolotarjovs, A., **Laganovska, K.**, Millers, D., Ignatans, R., Grabis, J. *Doped zirconia phase and luminescence dependence on the nature of charge compensation* (2017) Scientific Reports, 7, art. no. 44453.

2. **Laganovska, K.**, Bite, I., Zolotarjovs, A., Smits, K. *Niobium enhanced europium ion luminescence in hafnia nanocrystals* (2018) Journal of Luminescence, 203, pp. 358-363.

Thesis 2:

3. **Laganovska, K.**, Olsteins, D., Smits, K., Bite, I., Bikse, L.*Formation of translucent nanostructured zirconia ceramics* (2021) Journal of the European Ceramic Society, 41 (13), pp. 6641-6648.

Thesis 3:

4. **Laganovska, K.**, Bite, I., Zolotarjovs, A., Einbergs, E., Vitola, V., Dile, M., Smits, K. *Thermostimulated luminescence analysis of oxygen vacancies in* HfO_2 *nanoparticles* (2023) Materials Research Bulletin, 167, art. no. 112409, .

Thesis 4:

1. Smits, K., Olsteins, D., Zolotarjovs, A., **Laganovska, K.**, Millers, D., Ignatans, R., Grabis, J. *Doped zirconia phase and luminescence dependence on the nature of charge compensation* (2017) Scientific Reports, 7, art. no. 44453.

5. **Laganovska, K.**, I. Bite, A. Zolotarjovs, E. Einbergs, V. Vitola, and M. Dile. Eu^{3+} *ion incorporation in hafnia* – under review in Materials Research Bulletin

7.2 Other publications

(total: 15 publications, h-index: 7)

- Bite, I., **Laganovska, K.**, Vanags, E., Vitola, V. *Synthesis and characterization of translucent hafnia ceramics* (2023) Materialia, 32, art. no. 101887, .

- Kuzmin, A., Pudza, I., Dile, M., **Laganovska, K.**, Zolotarjovs, A. *Examining the Effect of Cu and Mn Dopants on the Structure of Zinc Blende ZnS Nanopowders* (2023) Materials, 16 (17), art. no. 5825

- Dile, M., **Laganovska, K.**, Zolotarjovs, A., Bite, I., Vanags, E., Kuzmin, A., Pudza, I., Smits, K. *The effect of surfactants and precursors on the structure and properties of ZnS:Cu nanocrystalline particles*, (2023) Nano-Structures and Nano-Objects, 35, art. no. 101023,

- Kuzmin, A., Dile, M., **Laganovska, K.**, Zolotarjovs, A. *Microwave-assisted synthesis and characterization of undoped and manganese doped zinc sulfide nanoparticles* (2022) Materials Chemistry and Physics, 290, art. no. 126583, .

- Vitola, V., **Laganovska, K.**, Bite, I., Einbergs, E., Millers, D. *The role of boric acid in optical information storage properties in Eu doped* $BaSi_2O_5$ (2022) Journal of Luminescence, 243, art. no. 118682, . Cited 1 time.

- **Laganovska, K.**, Olsteins, D., Smits, K., Bite, I., Bikse, L. *Formation of translucent nanostructured zirconia ceramics* (2021) Journal of the European Ceramic Society, 41 (13), pp. 6641-6648. Cited 2 times.

- Einbergs, E., Zolotarjovs, A., Bite, I., Cipa, J., Vitola, V., **Laganovska, K.**, Trinkler, L. *Re-Evaluation of Chromium Doped Alumina for Dosimetric Applications* (2021) Latvian Journal of Physics and Technical Sciences, 58 (1), pp. 15-22. Cited 1 time.

- Vitola, V., Bite, I., Millers, D., Zolotarjovs, A., **Laganovska, K.**, Smits, K., Spustaka, A. *The boron effect on low temperature luminescence of* $SrAl_2O_4$*:Eu, Dy* (2020) Ceramics International, 46 (16), pp. 26377-26381. Cited 9 times.

- Karitans, V., **Laganovska, K.**, Kundzins, K. *Phase retrieval of a Kolmogorov phase screen from very sparse data using four binary masks* (2020) Applied Optics, 59 (27), pp. 8362-8369.

- **Laganovska, K.**, Zolotarjovs, A., Vázquez, M., Mc Donnell, K., Liepins, J., Ben-Yoav, H., Karitans, V., Smits, K. *Portable low-cost open-source wireless spectrophotometer for fast and reliable measurements* (2020) HardwareX, 7, art. no. e00108. Cited 29 times.

- Einbergs, E., Zolotarjovs, A., Bite, I., **Laganovska, K.**, Auzins, K., Smits, K., Trinkler, L. *Usability of Cr-doped alumina in dosimetry* (2019) Ceramics, 2 (3), pp. 525-535. Cited 5 times.

- Zolotarjovs, A., Smits, K., **Laganovska, K.**, Bite, I., Grigorjeva, L., Auzins, K., Millers, D., Skuja, L. *Thermostimulated luminescence of plasma electrolytic oxidation coatings on 6082 aluminium surface* (2019) Radiation Measurements, 124, pp. 29-34. Cited 6 times.

- Auzins, K., Zolotarjovs, A., Bite, I., **Laganovska, K.**, Vitola, V., Smits, K., Millers, D. *Production of Phosphorescent Coatings on 6082 Aluminum Using Sr0.95Eu0.02Dy0.03Al2O4-Powder and Plasma Electrolytic Oxidation* (2019) Coatings, 9 (12), art. no. 865, . Cited 3 times.

- Bite, I., Krieke, G., Zolotarjovs, A., **Laganovska, K.**, Liepina, V., Smits, K., Auzins, K., Grigorjeva, L., Millers, D., Skuja, L. *Novel method of phosphorescent strontium aluminate coating preparation on aluminum* (2018) Materials and Design, 160, pp. 794-802. Cited 32 times.

- Gavrilović, T., **Laganovska, K.**, Zolotarjovs, A., Smits, K., Jovanović, D.J., Dramićanin, M.D. *High resolution luminescence spectroscopy and thermoluminescence of different size LaPO4:Eu3+ nanoparticles* (2018) Optical Materials, 82, pp. 39-46. Cited 3 times.

7.3 Conferences

- E-MRS 2023 Fall Laganovska K., Bite I., Zolotarjovs A., Smits K. ”Thermostimulated luminescence analysis of oxygen vacancies in HfO2 nanoparticles”, Warsaw, Poland, 2023

- Advanced Materials and Technologies Laganovska K., Bite I., Smits K. ”Study of Defects in Hafnia via Luminescent Properties”, Palanga, Lithuania, 2020

- Luminescent Detectors and Transformers of Ionizing Radiation K.Laganovska, K.Smits, I.Bite, A.Zolotarjovs, ”Defect reduction and europium ion luminescence enhancement in hafnia nanocrystals”, Prague, Czechia, 2017

- Advanced Materials and Technologies K. Laganovska, E.Einbergs, I. Bite, K. Smits, ”Terbium Ion Luminescence in Zirconia Single Crystals and Nanocrystals”, Palanga, Lithuania, 2017

- Functional Materials and Nanotechnologies K.Laganovska, I.Bite, K.Smits., ”Optical properties of HfO2 and HfO2:Eu3+ synthesized by various methods”, Riga, Latvia, 2017

- University of Latvia, Institute of Solid State Physics, 34. scientific conference K.Laganovska, I.Bite, K.Smits, ”Niobium enhanced europium ion luminescence in hafnia nanocrystals”, Riga, Latvia, 2017

8.ACKNOWLEDGEMENTS

The author sincerely expresses her gratitude to the scientific supervisor Dr.Phys. Krišjānis Šmits as well as the head of the Optical materials laboratory Dr.Phys. Aleksejs Zolotarjovs. No less significant is the support (both scientific and emotional) the author received from colleagues MSc.Chem. Ivita Bite and Dr.Phys. Virginīja Vitola.

The help of colleagues from other laboratories, as well as staff of the Institute of Solid State Physics, is also greatly appreciated.

Additionally, the author wants to thank the Faculty of Physics, Mathematics and Optometry of the University of Latvia for the constant support in studies and research through various programs, consultations, software licensing, and seminars.

This research was partly supported by the ERDF project No. 1.1.1.1/21/A/055.

Institute of Solid State Physics, University of Latvia as the Center of Excellence has received funding from the European Union's Horizon 2020 Framework Programme H2020-WIDESPREAD-01-2016-2017-TeamingPhase2 under grant agreement No. 739508, project CAMART^2

ERAF
EIROPAS REĢIONĀLĀS
ATTĪSTĪBAS FONDS

LATVIJAS UNIVERSITĀTES
CIETVIELU FIZIKAS INSTITŪTS
INSTITUTE OF SOLID STATE PHYSICS
UNIVERSITY OF LATVIA

9.REFERENCES

1. Moore, G. E. Progress in digital integrated electronics. *Electron Devices Meeting* (1975).
2. Chau, R., Datta, S., Doczy, M., Doyle, B., Kavalieros, J. & Metz, M. High-κ/metal-gate stack and its MOSFET characteristics. *IEEE Electron Device Lett.* **25,** 408–410 (June 2004).
3. Jiang, H., Gomez-Abal, R. I., Rinke, P. & Scheffler, M. Electronic band structure of zirconia and hafnia polymorphs from the *GW* perspective. *Phys. Rev. B Condens. Matter* **81,** 085119 (Feb. 2010).
4. Huang A.P. Yang Z.C., C. P. K. Hafnium-based High-k Gate Dielectrics. *Advances in Solid State Circuit Technologies* (2010).
5. Böscke, T. S., Müller, J., Bräuhaus, D., Schröder, U. & Böttger, U. Ferroelectricity in hafnium oxide thin films. *Appl. Phys. Lett.* **99,** 102903. ISSN: 0003-6951 (Sept. 2011).
6. Wang, B., Wang, M., Duan, F., Ren, J., Li, Y. & Zhou, T. First principles study of defects in high-k HfO_2. *Superlattices Microstruct.* **99,** 88–93. ISSN: 0749-6036 (Nov. 2016).
7. Zhao, X. & Vanderbilt, D. First-principles study of structural, vibrational, and lattice dielectric properties of hafnium oxide. *Phys. Rev. B Condens. Matter* **65,** 233106 (June 2002).
8. Johnson, B. & Jones, J. L. in *Ferroelectricity in Doped Hafnium Oxide: Materials, Properties and Devices* (eds Schroeder, U., Hwang, C. S. & Funakubo, H.) 25–45 (Woodhead Publishing, 2019). ISBN: 978-0-08-102430-0.
9. Shannon, R. D. Revised effective ionic radii and systematic studies of interatomic distances in halides and chalcogenides. en. *Acta Crystallogr. A* **32,** 751–767. ISSN: 0567-7394 (Sept. 1976).
10. Ruh, R. & Corfield, P. W. R. Crystal structure of monoclinic Hafnia and comparison with monoclinic Zirconia. en. *J. Am. Ceram. Soc.* **53,** 126–129. ISSN: 0002-7820, 1551-2916 (Mar. 1970).
11. Wang, J., Li, H. P. & Stevens, R. Hafnia and hafnia-toughened ceramics. *J. Mater. Sci.* **27,** 5397–5430. ISSN: 0022-2461, 1573-4803 (Oct. 1992).
12. Ho, S.-M. On the structural chemistry of zirconium oxide. *Materials Science and Engineering* **54,** 23–29. ISSN: 0025-5416 (1982).

13. Huan, T. D., Sharma, V., Rossetti, G. A. & Ramprasad, R. Pathways towards ferroelectricity in hafnia. *Phys. Rev. B* **90,** 064111 (6 Aug. 2014).

14. Curtis, C. E., Doney, L. M. & Johnson, J. R. Some properties of hafnium oxide, hafnium silicate, calcium hafnate, and hafnium carbide. en. *J. Am. Ceram. Soc.* **37,** 458–465. ISSN: 0002-7820, 1551-2916 (Oct. 1954).

15. Smith, D. K. & Newkirk, W. The crystal structure of baddeleyite (monoclinic ZrO_2) and its relation to the polymorphism of ZrO_2. *Acta Crystallographica* **18,** 983–991 (1965).

16. Patil, R. & Subbarao, E. Monoclinic–tetragonal phase transition in zirconia: mechanism, pretransformation and coexistence. *Acta Crystallographica Section A* **26.** Cited by: 89, 535–542 (1970).

17. Foster, A. S., Lopez Gejo, F., Shluger, A. L. & Nieminen, R. M. Vacancy and interstitial defects in hafnia. *Phys. Rev. B Condens. Matter* **65,** 174117. ISSN: 0163-1829 (May 2002).

18. Foster, A. S., Sulimov, V. B., Lopez Gejo, F., Shluger, A. L. & Nieminen, R. M. Structure and electrical levels of point defects in monoclinic zirconia. *Phys. Rev. B Condens. Matter* **64,** 224108. ISSN: 0163-1829 (Nov. 2001).

19. Crocombette, J.-P. Theoretical study of point defects in crystalline zircon. *Phys. Chem. Miner.* **27,** 138–143 (1999).

20. Rosenblatt, G. H., Rowe, M. W., Williams Jr, G. P., Williams, R. T. & Chen, Y. Luminescence of F and F+ centers in magnesium oxide. en. *Phys. Rev. B Condens. Matter* **39,** 10309–10318. ISSN: 0163-1829, 1095-3795 (May 1989).

21. Zheng, J. X., Ceder, G., Maxisch, T., Chim, W. K. & Choi, W. K. First-principles study of native point defects in hafnia and zirconia. *Phys. Rev. B Condens. Matter* **75,** 104112. ISSN: 0163-1829 (Mar. 2007).

22. Chimata, R., Shin, H., Benali, A. & Heinonen, O. Defect energetics of cubic hafnia from quantum Monte Carlo simulations. *Phys. Rev. Materials* **3,** 075005 (July 2019).

23. Xiong, K. & Robertson, J. Point defects in HfO_2 high K gate oxide. *Microelectron. Eng.* **80,** 408–411. ISSN: 0167-9317 (June 2005).

24. Anderson, P. W. Model for the electronic structure of amorphous semiconductors. *Phys. Rev. Lett.* **34,** 953–955. ISSN: 0031-9007, 1079-7114 (Apr. 1975).

25. Bylander, D. M. & Kleinman, L. Good semiconductor band gaps with a modified local-density approximation. en. *Phys. Rev. B Condens. Matter* **41,** 7868–7871. ISSN: 0163-1829 (Apr. 1990).

26. Rushton, P. P., Tozer, D. J. & Clark, S. J. Nonlocal density-functional description of exchange and correlation in silicon. *Phys. Rev. B Condens. Matter* **65,** 235203. ISSN: 0163-1829 (May 2002).

27. Afanasev, V. V., Stesmans, A., Chen, F., Shi, X. & Campbell, S. A. Internal photoemission of electrons and holes from (100) Si into HfO_2. *Appl. Phys. Lett.* **81,** 1053–1055. ISSN: 0003-6951, 1077-3118 (Aug. 2002).

28. Kang, A. Y., Lenahan, P. M. & Conley, J. F. Electron spin resonance observation of trapped electron centers in atomic-layer-deposited hafnium oxide on Si. *Appl. Phys. Lett.* **83,** 3407–3409. ISSN: 0003-6951 (Oct. 2003).

29. Xiong, K., Robertson, J., Gibson, M. C. & Clark, S. J. Defect energy levels in HfO_2 high-dielectric-constant gate oxide. *Appl. Phys. Lett.* **87,** 183505. ISSN: 0003-6951, 1077-3118 (Oct. 2005).

30. Robertson, J. Band offsets of wide-band-gap oxides and implications for future electronic devices. *J. Vac. Sci. Technol. B Microelectron. Nanometer Struct. Process. Meas. Phenom.* **18,** 1785–1791. ISSN: 1071-1023 (May 2000).

31. Houssa, M., Tuominen, M., Naili, M., Afanas'ev, V., Stesmans, A., Haukka, S. & Heyns, M. M. Trap-assisted tunneling in high permittivity gate dielectric stacks. *J. Appl. Phys.* **87,** 8615–8620. ISSN: 0021-8979 (June 2000).

32. Kukli, K., Ritala, M., Sundqvist, J., Aarik, J., Lu, J., Sajavaara, T., Leskelä, M. & Hårsta, A. Properties of hafnium oxide films grown by atomic layer deposition from hafnium tetraiodide and oxygen. *J. Appl. Phys.* **92,** 5698–5703. ISSN: 0021-8979 (Nov. 2002).

33. Cho, M.-H., Roh, Y. S., Whang, C. N., Jeong, K., Nahm, S. W., Ko, D.-H., Lee, J. H., Lee, N. I. & Fujihara, K. Thermal stability and structural characteristics of HfO_2 films on Si (100) grown by atomic-layer deposition. *Appl. Phys. Lett.* **81,** 472–474. ISSN: 0003-6951, 1077-3118 (July 2002).

34. Wang, L., Maxisch, T. & Ceder, G. Oxidation energies of transition metal oxides within the GGA+U framework. *Phys. Rev. B Condens. Matter* **73,** 195107. ISSN: 0163-1829 (May 2006).

35. Xue, K.-H. & Miao, X.-S. Oxygen vacancy chain and conductive filament formation in hafnia. *J. Appl. Phys.* **123,** 161505. ISSN: 0021-8979 (Apr. 2018).

36. Freysoldt, C., Grabowski, B., Hickel, T., Neugebauer, J., Kresse, G., Janotti, A. & Van de Walle, C. G. First-principles calculations for point defects in solids. *Rev. Mod. Phys.* **86,** 253–305. ISSN: 0034-6861 (Mar. 2014).

37. Feng, Y. P., Lim, A. T. L. & Li, M. F. Negative-U property of oxygen vacancy in cubic HfO_2. *Appl. Phys. Lett.* **87,** 062105. ISSN: 0003-6951, 1077-3118 (Aug. 2005).

38. Lim, S.-G., Kriventsov, S., Jackson, T. N., Haeni, J. H., Schlom, D. G., Balbashov, A. M., Uecker, R., Reiche, P., Freeouf, J. L. & Lucovsky, G. Dielectric functions and optical bandgaps of high-K dielectrics for metal-oxide-semiconductor field-effect transistors by far ultraviolet spectroscopic ellipsometry. *J. Appl. Phys.* **91,** 4500–4505. ISSN: 0021-8979 (Apr. 2002).

39. Umezawa, N., Shiraishi, K., Torii, K., Boero, M., Chikyow, T., Watanabe, H., Yamabe, K., Ohno, T., Yamada, K. & Nara, Y. Role of Nitrogen Atoms in Reduction of Electron Charge Traps in Hf-Based High- κ Dielectrics. *IEEE Electron Device Lett.* **28,** 363–365. ISSN: 0741-3106, 1558-0563 (May 2007).

40. Shin, H., Luo, Y., Ganesh, P., Balachandran, J., Krogel, J. T., Kent, P. R. C., Benali, A. & Heinonen, O. Electronic properties of doped and defective NiO: A quantum Monte Carlo study. *Phys. Rev. Materials* **1,** 073603 (Dec. 2017).

41. Kylänpää, I., Balachandran, J., Ganesh, P., Heinonen, O., Kent, P. R. C. & Krogel, J. T. Accuracy of ab initio electron correlation and electron densities in vanadium dioxide. *Phys. Rev. Materials* **1,** 065408 (Nov. 2017).

42. Maurya, S. Effect of nitrogen passivation/pre nitration on interface properties of atomic layer deposited HfO_2. *J. Mater. Sci.: Mater. Electron.* **29,** 7917–7923. ISSN: 0957-4522, 1573-482X (May 2018).

43. Kiisk, V., Lange, S., Utt, K., Tätte, T., Mändar, H. & Sildos, I. Photoluminescence of sol–gel-prepared hafnia. *Physica B Condens. Matter* **405,** 758–762. ISSN: 0921-4526 (Jan. 2010).

44. Muñoz Ramo, D., Gavartin, J. L., Shluger, A. L. & Bersuker, G. Spectroscopic properties of oxygen vacancies in monoclinic HfO_2 calculated with periodic and embedded cluster density functional theory. *Phys. Rev. B Condens. Matter* **75,** 205336. ISSN: 0163-1829 (May 2007).

45. Petrik, N. G., Taylor, D. P. & Orlando, T. M. Laser-stimulated luminescence of yttria-stabilized cubic zirconia crystals. *J. Appl. Phys.* **85,** 6770–6776. ISSN: 0021-8979 (May 1999).

46. Gritsenko, V. A., Islamov, D. R., Perevalov, T. V., Aliev, V. S., Yelisseyev, A. P., Lomonova, E. E., Pustovarov, V. A. & Chin, A. Oxygen vacancy in Hafnia as a blue luminescence center and a trap of charge carriers. en. *J. Phys. Chem. C Nanomater. Interfaces* **120,** 19980–19986. ISSN: 1932-7447, 1932-7455 (Sept. 2016).

47. Rastorguev, A. A., Belyi, V. I., Smirnova, T. P., Yakovkina, L. V., Zamoryanskaya, M. V., Gritsenko, V. A. & Wong, H. Luminescence of intrinsic and extrinsic defects in hafnium oxide films. *Phys. Rev. B Condens. Matter* **76,** 235315. ISSN: 0163-1829 (Dec. 2007).

48. Perevalov, T. V., Aliev, V. S., Gritsenko, V. A., Saraev, A. A., Kaichev, V. V., Ivanova, E. V. & Zamoryanskaya, M. V. The origin of 2.7 eV luminescence and 5.2 eV excitation band in hafnium oxide. *Appl. Phys. Lett.* **104,** 071904. ISSN: 0003-6951 (Feb. 2014).

49. Dexter, D. L. & Schulman, J. H. Theory of Concentration Quenching in Inorganic Phosphors. *J. Chem. Phys.* **22,** 1063–1070. ISSN: 0021-9606 (June 1954).

50. Martínez, F. L., Toledano-Luque, M., Gandía, J. J., Cárabe, J., Bohne, W., Röhrich, J., Strub, E. & Mártil, I. Optical properties and structure of HfO_2 thin films grown by high pressure reactive sputtering. *Journal of Physics D: Applied Physics* **40,** 5256–5265. ISSN: 00223727 (2007).

51. Fan, X., Liu, H., Zhong, B., Fei, C., Wang, X. & Wang, Q. Optical characteristics of H_2O-based and O_3-based HfO_2 films deposited by ALD using spectroscopy ellipsometry. *Appl. Phys. A: Mater. Sci. Process.* **119,** 957–963. ISSN: 1432-0630 (June 2015).

52. Lucovsky, G., Seo, H., Lee, S., Fleming, L. B., Ulrich, M. D., Lüning, J., Lysaght, P. & Bersuker, G. Intrinsic Electronically Active Defects in Transition Metal Elemental Oxides. en. *Jpn. J. Appl. Phys.* **46,** 1899. ISSN: 1347-4065 (Apr. 2007).

53. Nasyrov, K. A. & Gritsenko, V. A. Charge transport in dielectrics by tunneling between traps. *J. Exp. Theor. Phys.* **112,** 1026–1034. ISSN: 1090-6509 (June 2011).

54. McKeever, S. W. S. *Thermoluminescence of Solids McKeever* (Cambridge University Press, July 1983).

55. Perevalov, T. V., Aliev, V. S., Gritsenko, V. A., Saraev, A. A. & Kaichev, V. V. Electronic structure of oxygen vacancies in hafnium oxide. *Microelectron. Eng.* **109,** 21–23. ISSN: 0167-9317 (Sept. 2013).

56. Kaichev, V. V., Ivanova, E. V., Zamoryanskaya, M. V., Smirnova, T. P., Yakovkina, L. V. & Gritsenko, V. A. XPS and cathodoluminescence studies of HfO_2, Sc_2O_3 and $(HfO_2)_{1-x}(Sc_2O_3)_x$ films. *Eur. Phys. J. Appl. Phys.* **64,** 10302. ISSN: 1286-0042, 1286-0050 (Oct. 2013).

57. Sen, B., Wong, H., Yang, B. L., Huang, A. P., Chu, P. K., Filip, V. & Sarkar, C. K. Nitrogen Incorporation into Hafnium Oxide Films by Plasma Immersion Ion Implantation. en. *Jpn. J. Appl. Phys.* **46,** 3234. ISSN: 1347-4065 (May 2007).

58. Wong, C. K., Wong, H., Liu, J. & Misiuk, A. Properties of Silicon Oxynitride Films Annealed under Enhanced Hydrostatic Pressure. en. *J. Electrochem. Soc.* **158,** H322. ISSN: 0013-4651, 1945-7111 (Jan. 2011).

59. Wong, H. & Iwai, H. On the scaling issues and high-κ replacement of ultrathin gate dielectrics for nanoscale MOS transistors. *Microelectron. Eng.* **83,** 1867–1904. ISSN: 0167-9317 (Oct. 2006).

60. Chen, S., Liu, Z., Feng, L. & Zhao, X. Photoluminescent properties of undoped and Ce-doped HfO_2 thin films prepared by magnetron sputtering. *J. Lumin.* **153,** 148–151. ISSN: 0022-2313 (Sept. 2014).

61. Ortega, A., Rubio, E. J., Abhilash, K. & Ramana, C. V. Correlation between phase and optical properties of yttrium-doped hafnium oxide nanocrystalline thin films. *Opt. Mater.* **35,** 1728–1734. ISSN: 0925-3467 (July 2013).

62. Laganovska, K., Bite, I., Zolotarjovs, A. & Smits, K. Niobium enhanced europium ion luminescence in hafnia nanocrystals. *J. Lumin.* **203,** 358–363. ISSN: 0022-2313 (Nov. 2018).

63. Shilov, A. O., Savchenko, S. S., Vokhmintsev, A. S., Gritsenko, V. A. & Weinstein, I. A. Thermal quenching of self-trapped exciton luminescence in nanostructured hafnia. *J. Lumin.* **247,** 118908. ISSN: 0022-2313 (July 2022).

64. Adams, D. M., Leonard, S., Russell, D. R. & Cernik, R. J. X-ray diffraction study of Hafnia under high pressure using synchrotron radiation. en. *J. Phys. Chem. Solids* **52,** 1181–1186. ISSN: 0022-3697, 1879-2553 (Jan. 1991).

65. Gavartin, J. L., Muñoz Ramo, D., Shluger, A. L., Bersuker, G. & Lee, B. H. Negative oxygen vacancies in HfO_2 as charge traps in high-k stacks. *Appl. Phys. Lett.* **89,** 082908. ISSN: 0003-6951 (Aug. 2006).

66. Franta, D., Ohlídal, I., Nečas, D., Vižd'a, F., Caha, O., Hasoň, M. & Pokorný, P. Optical characterization of HfO_2 thin films. *Thin Solid Films* **519,** 6085–6091. ISSN: 0040-6090 (July 2011).

67. Manikantan, J., Ramalingam, H. B., Shekar, B. C., Murugan, B., Kumar, R. R. & Santhoshi, J. S. Physical and optical properties of HfO_2 NPs – Synthesis and characterization in finding its feasibility in opto-electronic devices. *Adv. Powder Technol.* **28,** 1636–1646. ISSN: 0921-8831 (July 2017).

68. Aarik, J., Mändar, H., Kirm, M. & Pung, L. Optical characterization of HfO_2 thin films grown by atomic layer deposition. *Thin Solid Films* **466,** 41–47. ISSN: 0040-6090 (Nov. 2004).

69. Tauc, J. *Amorphous and Liquid Semiconductors* en (ed Tauc, J.) ISBN: 9781461587057 (Springer Science & Business Media, Dec. 2012).

70. Lozanov, V. V., Baklanova, N. I., Shayapov, V. R. & Berezin, A. S. Crystal Growth and Photoluminescence Properties of Reactive CVD-Derived Monoclinic Hafnium Dioxide. *Cryst. Growth Des.* **16,** 5283–5293. ISSN: 1528-7483 (Sept. 2016).

71. Liu, Q.-J., Zhang, N.-C., Liu, F.-S. & Liu, Z.-T. Structural, electronic, optical, elastic properties and Born effective charges of monoclinic HfO_2 from first-principles calculations. en. *Chin. Physics B* **23,** 047101. ISSN: 1674-1056 (Feb. 2014).

72. Perevalov, T. & Gritsenko, V. Application and electronic structure of high-permittivity dielectrics. *Physics-Uspekhi* **53.** cited By 51, 561–575 (2010).

73. Vokhmintsev, A. S. & Weinstein, I. A. Temperature effects in 3.9 eV photoluminescence of hexagonal boron nitride under band-to-band and subband excitation within 7–1100 K range. *J. Lumin.* **230,** 117623. ISSN: 0022-2313 (Feb. 2021).

74. Williams, R. T. & Song, K. S. The self-trapped exciton. *J. Phys. Chem. Solids* **51,** 679–716. ISSN: 0022-3697 (Jan. 1990).

75. Pelant, I. & Valenta, J. *Luminescence Spectroscopy of Semiconductors* en. ISBN: 9780199588336 (OUP Oxford, Feb. 2012).

76. Muñoz Ramo, D., Shluger, A. L., Gavartin, J. L. & Bersuker, G. Theoretical prediction of intrinsic self-trapping of electrons and holes in monoclinic HfO_2. en. *Phys. Rev. Lett.* **99,** 155504. ISSN: 0031-9007, 1079-7114 (Oct. 2007).

77. Sklénard, B., Dragoni, A., Triozon, F. & Olevano, V. Optical vs electronic gap of hafnia by ab initio Bethe-Salpeter equation. *Appl. Phys. Lett.* **113,** 172903. ISSN: 0003-6951 (Oct. 2018).

78. Kirm, M., Aarik, J., Jürgens, M. & Sildos, I. Thin films of HfO_2 and ZrO_2 as potential scintillators. *Nucl. Instrum. Methods Phys. Res. A* **537,** 251–255. ISSN: 0168-9002 (Jan. 2005).

79. Villa, I., Lauria, A., Moretti, F., Fasoli, M., Dujardin, C., Niederberger, M. & Vedda, A. Radio-luminescence spectral features and fast emission in hafnium dioxide nanocrystals. en. *Phys. Chem. Chem. Phys.* **20,** 15907–15915. ISSN: 1463-9076, 1463-9084 (June 2018).

80. Kong, M., Li, B., Guo, C., Zeng, P., Wei, M. & He, W. The Optical Absorption and Photoluminescence Characteristics of Evaporated and IAD HfO_2 Thin Films. en. *Coat. World* **9,** 307. ISSN: 1527-1129 (May 2019).

81. Gritsenko, V. A., Perevalov, T. V. & Islamov, D. R. Electronic properties of hafnium oxide: A contribution from defects and traps. *Phys. Rep.* **613,** 1–20. ISSN: 0370-1573 (Feb. 2016).

82. Bhuvanesh, N. S. P. & Gopalakrishnan, J. Solid-state chemistry of early transition-metal oxides containing d0 and d1 cations. en. *J. Mater. Chem.* **7,** 2297–2306. ISSN: 0959-9428, 1364-5501 (Jan. 1997).

83. Takeuchi, H., Wong, H. Y., Ha, D. & King, T.-J. *Impact of oxygen vacancies on high-k gate stack engineering* in *IEDM Technical Digest. IEEE International Electron Devices Meeting, 2004.* (Dec. 2004), 829–832.

84. Aleksanyan, E., Kirm, M., Feldbach, E. & Harutyunyan, V. Identification of F+ centers in hafnia and zirconia nanopowders. *Radiat. Meas.* **90,** 84–89. ISSN: 1350-4487 (July 2016).

85. Villa, I. *et al.* Size-Dependent Luminescence in HfO2 Nanocrystals: Toward White Emission from Intrinsic Surface Defects. *Chem. Mater.* **28,** 3245–3253. ISSN: 0897-4756 (May 2016).

86. *Spectroscopic Properties of Rare Earths in Optical Materials* (ed Robert Hull, Jürgen Parisi, R. M. Osgood, Hans Warlimont, Guokui Liu, Bernard Jacquier) (Springer Berlin Heidelberg).

87. Rajnak, K. & Wybourne, B. G. Configuration Interaction in Crystal Field Theory. *J. Chem. Phys.* **41,** 565–569. ISSN: 0021-9606 (July 1964).

88. Freeman, A. J. & Watson, R. E. Theoretical Investigation of Some Magnetic and Spectroscopic Properties of Rare-Earth Ions. *Phys. Rev.* **127,** 2058–2075. ISSN: 0959-8472 (Sept. 1962).

89. Binnemans, K. Interpretation of europium(III) spectra. *Coord. Chem. Rev.* **295,** 1–45. ISSN: 0010-8545 (July 2015).

90. Binnemans, K. & Görller-Walrand, C. Application of the Eu^{3+} Ion for site symmetry determination. English. *Journal of Rare Earths* **14.** Cited By :177, 179–180 (1996).

91. Patra, A., Friend, C. S., Kapoor, R. & Prasad, P. N. Upconversion in Er^{3+}:ZrO_2 Nanocrystals. *J. Phys. Chem. B* **106,** 1909–1912. ISSN: 1520-6106 (Feb. 2002).

92. Silver, J., Martinez-Rubio, M. I., Ireland, T. G., Fern, G. R. & Withnall, R. The Effect of Particle Morphology and Crystallite Size on the Upconversion Luminescence Properties of Erbium and Ytterbium Co-doped Yttrium Oxide Phosphors. *J. Phys. Chem. B* **105,** 948–953. ISSN: 1520-6106 (Feb. 2001).

93. Golding, P. S., Jackson, S. D., King, T. A. & Pollnau, M. Energy transfer processes in Er^{3+}-doped and $Er^{3+}Pr^{3+}$-codoped ZBLAN glasses. *Phys. Rev. B Condens. Matter* **62,** 856–864. ISSN: 0163-1829 (July 2000).

94. Kapoor, R., Friend, C. S., Biswas, A. & Prasad, P. N. Highly efficient infrared-to-visible energy upconversion in Er^{3+}:Y_2O_3). en. *Opt. Lett.* **25,** 338–340. ISSN: 0146-9592 (Mar. 2000).

95. Chen, R. & Kirsh, Y. *The analysis of thermally stimulated processes* en. ISBN: 9780080229300 (Pergamon, Amsterdam, Netherlands, Feb. 1981).

96. Jabłoński, A. Über den Mechanismus der Photolumineszenz von Farbstoffphosphoren. de. *Eur. Phys. J. A* **94,** 38–46. ISSN: 1434-6001, 1434-601X (Jan. 1935).

97. Vij, D. R. *Luminescence of Solids* en (ed Vij, D. R.) ISBN: 9781461374466, 9781461553618 (Springer US, New York, NY, Oct. 2012).

98. Garlick, G. F. J. & Gibson, A. F. The Electron Trap Mechanism of Luminescence in Sulphide and Silicate Phosphors. en. *Proc. Phys. Soc. London* **60,** 574. ISSN: 0959-5309 (June 1948).

99. Chen, R. & Winer, S. A. A. Effects of Various Heating Rates on Glow Curves. *J. Appl. Phys.* **41,** 5227–5232. ISSN: 0021-8979 (Dec. 1970).

100. Plummer, J. & Griffin, P. Material and process limits in silicon VLSI technology. *Proceedings of the IEEE* **89,** 240–258 (2001).

101. Kumar, N., George, B. P. A., Abrahamse, H., Parashar, V., Ray, S. S. & Ngila, J. C. A novel approach to low-temperature synthesis of cubic HfO_2 nanostructures and their cytotoxicity. en. *Sci. Rep.* **7,** 9351. ISSN: 2045-2322 (Aug. 2017).

102. Zafar, S., Callegari, A., Gusev, E. & Fischetti, M. V. Charge trapping related threshold voltage instabilities in high permittivity gate dielectric stacks. *J. Appl. Phys.* **93,** 9298–9303. ISSN: 0021-8979 (June 2003).

103. Cockayne, E. Influence of oxygen vacancies on the dielectric properties of hafnia: First-principles calculations. *Phys. Rev. B Condens. Matter* **75,** 094103. ISSN: 0163-1829 (Mar. 2007).

104. Auciello, O., Scott, J. F. & Ramesh, R. The Physics of Ferroelectric Memories. *Phys. Today* **51,** 22–27. ISSN: 0031-9228 (July 1998).

105. Kaplan, R., Yavits, L., Kaplan, R., Yavits, L. & Ginosar, R. From processing-in-memory to processing-in-storage. *Supercomputing Frontiers and Innovations* **4.** cited By 4, 99–116 (2017).

106. Valasek, J. Piezo-Electric and Allied Phenomena in Rochelle Salt. *Phys. Rev.* **17,** 475–481. ISSN: 0959-8472 (Apr. 1921).

107. Jaffe, B., Roth, R. S. & Marzullo, S. Piezoelectric Properties of Lead Zirconate-Lead Titanate Solid-Solution Ceramics. *J. Appl. Phys.* **25,** 809–810. ISSN: 0021-8979 (June 1954).

108. Martin, R. M. Piezoelectricity. *Phys. Rev. B Condens. Matter* **5,** 1607–1613. ISSN: 0163-1829 (Feb. 1972).

109. Oh, S., Hwang, H. & Yoo, I. K. Ferroelectric materials for neuromorphic computing. *APL Materials* **7,** 091109 (Sept. 2019).

110. Polakowski, P. & Müller, J. Ferroelectricity in undoped hafnium oxide. *Appl. Phys. Lett.* **106,** 232905. ISSN: 0003-6951 (June 2015).

111. Starschich, S., Menzel, S. & Böttger, U. Evidence for oxygen vacancies movement during wake-up in ferroelectric hafnium oxide. *Appl. Phys. Lett.* **108,** 032903. ISSN: 0003-6951 (Jan. 2016).

112. Kim, T., Park, J., Cheong, B.-H. & Jeon, S. Effects of high pressure nitrogen annealing on ferroelectric $Hf_{0.5}Zr_{0.5}O_2$ films. *Appl. Phys. Lett.* **112,** 092906. ISSN: 0003-6951 (Feb. 2018).

113. Kim, S. J. *et al.* A Comprehensive Study on the Effect of TiN Top and Bottom Electrodes on Atomic Layer Deposited Ferroelectric Hf0.5Zr0.5O2 Thin Films. en. *Materials* **13.** ISSN: 1996-1944 (July 2020).

114. Shimizu, T., Mimura, T., Kiguchi, T., Shiraishi, T., Konno, T., Katsuya, Y., Sakata, O. & Funakubo, H. Ferroelectricity mediated by ferroelastic domain switching in HfO_2-based epitaxial thin films. *Appl. Phys. Lett.* **113,** 212901. ISSN: 0003-6951 (Nov. 2018).

115. Park, M. H. *et al.* Ferroelectricity and antiferroelectricity of doped thin HfO_2-based films. en. *Adv. Mater.* **27,** 1811–1831. ISSN: 0935-9648, 1521-4095 (Mar. 2015).

116. Schroeder, U., Yurchuk, E., Müller, J., Martin, D., Schenk, T., Polakowski, P., Adelmann, C., Popovici, M. I., Kalinin, S. V. & Mikolajick, T. Impact of different dopants on the switching properties of ferroelectric hafniumoxide. *Japanese Journal of Applied Physics* **53,** 08LE02 (July 2014).

117. Müller, J., Böscke, T. S., Schröder, U., Mueller, S., Bräuhaus, D., Böttger, U., Frey, L. & Mikolajick, T. Ferroelectricity in simple binary ZrO_2 and HfO_2. en. *Nano Lett.* **12,** 4318–4323. ISSN: 1530-6984, 1530-6992 (Aug. 2012).

118. Mueller, S., Mueller, J., Singh, A., Riedel, S., Sundqvist, J., Schroeder, U. & Mikolajick, T. Incipient ferroelectricity in Al-doped HfO_2 thin films. en. *Adv. Funct. Mater.* **22,** 2412–2417. ISSN: 1616-301X, 1616-3028 (June 2012).

119. Park, M. H., Kim, H. J., Kim, Y. J., Moon, T., Kim, K. D. & Hwang, C. S. Thin $Hf_xZr_{1-x}O_2$ Films: A new lead-free system for electrostatic supercapacitors with large energy storage density and robust thermal stability. en. *Adv. Energy Mater.* **4,** 1400610. ISSN: 1614-6832, 1614-6840 (Nov. 2014).

120. Mimura, T., Shimizu, T., Uchida, H. & Funakubo, H. Room-temperature deposition of ferroelectric HfO_2-based films by the sputtering method. *Appl. Phys. Lett.* **116,** 062901. ISSN: 0003-6951 (Feb. 2020).

121. Kirbach, S., Lederer, M., Eßlinger, S., Mart, C., Czernohorsky, M., Weinreich, W. & Wallmersperger, T. Doping concentration dependent piezoelectric behavior of Si:HfO_2 thin-films. *Appl. Phys. Lett.* **118,** 012904. ISSN: 0003-6951 (Jan. 2021).

122. Xu, X., Huang, F.-T., Qi, Y., Singh, S., Rabe, K. M., Obeysekera, D., Yang, J., Chu, M.-W. & Cheong, S.-W. Kinetically stabilized ferroelectricity in bulk single-crystalline HfO_2:Y. en. *Nat. Mater.* **20,** 826–832. ISSN: 1476-1122 (June 2021).

123. Park, M. H., Lee, Y. H., Mikolajick, T., Schroeder, U. & Hwang, C. S. Review and perspective on ferroelectric HfO_2-based thin films for memory applications. *MRS Communications* **8,** 795–808. ISSN: 2159-6867 (Sept. 2018).

124. Mikolajick, T., Slesazeck, S., Park, M. H. & Schroeder, U. Ferroelectric hafnium oxide for ferroelectric random-access memories and ferroelectric field-effect transistors. *MRS Bull.* **43,** 340–346. ISSN: 0883-7694, 1938-1425 (May 2018).

125. Park, J. Y., Yang, K., Lee, D. H., Kim, S. H., Lee, Y., Reddy, P. R. S., Jones, J. L. & Park, M. H. A perspective on semiconductor devices based on fluorite-structured ferroelectrics from the materials–device integration perspective. *J. Appl. Phys.* **128,** 240904. ISSN: 0021-8979 (Dec. 2020).

126. Pešić, M., Künneth, C., Hoffmann, M., Mulaosmanovic, H., Müller, S., Breyer, E. T., Schroeder, U., Kersch, A., Mikolajick, T. & Slesazeck, S. A computational study of hafnia-based ferroelectric memories: from ab initio via physical modeling to circuit models of ferroelectric device. *J. Comput. Electron.* **16,** 1236–1256. ISSN: 1569-8025, 1572-8137 (Dec. 2017).

127. Park, M. *et al.* Review of defect chemistry in fluorite-structure ferroelectrics for future electronic devices. *Journal of Materials Chemistry C* **8.** cited By 60, 10526–10550 (2020).

128. Lee, D. H. *et al.* Domains and domain dynamics in fluorite-structured ferroelectrics. *Applied Physics Reviews* **8,** 021312 (June 2021).

129. Brinker, C. J. & Scherer, G. W. *Sol-Gel Science: The Physics and Chemistry of Sol-Gel Processing* 1–908 (2013).

130. Schubert, U. in *The Sol-Gel Handbook* 1–28 (John Wiley Sons, Ltd, 2015). ISBN: 9783527670819.

131. Morey, G. W. & Niggli, P. The Hydrothermal Formation of Silicates, A Review. *Journal of the American Chemical Society* **35,** 1086–1130 (1913).

132. Tuttle, O. F. (F. *Origin of granite in the light of experimental studies in the system, NaAlSi3O8=KAlSi3O8=SiO2=H2O* (Geological Society of America], New York, 1958).

133. Fenn, P. M. The nucleation and growth of alkali feldspars from hydrous melts. *The Canadian Mineralogist* **15,** 135–161 (1977).

134. Yang, G. & Park, S.-J. Conventional and Microwave Hydrothermal Synthesis and Application of Functional Materials: A Review. en. *Materials* **12.** ISSN: 1996-1944 (Apr. 2019).

135. Dell'Agli, G., Colantuono, A. & Mascolo, G. The effect of mineralizers on the crystallization of zirconia gel under hydrothermal conditions. *Solid State Ionics* **123,** 87–94. ISSN: 0167-2738 (1999).

136. Cheng, H., Ma, J., Zhao, Z. & Qi, L. Hydrothermal Preparation of Uniform Nanosize Rutile and Anatase Particles. *Chemistry of Materials* **7,** 663–671 (1995).

137. Roble, M., Rojas, S., Wheatley, R., Wallentowitz, S., Cabrera, A. & Diaz-Droguett, D. Hydrothermal improvement for 3R-CuFeO2 delafossite growth by control of mineralizer and reaction atmosphere. *Journal of Solid State Chemistry* **271,** 314–325. ISSN: 0022-4596 (2019).

138. Apostol, I., Saravanan, K. V., Monty, C. J. A. & Vilarinho, P. M. Solar physical vapor deposition: A new approach for preparing magnesium titanate nanopowders. *Appl. Surf. Sci.* **285,** 49–55. ISSN: 0169-4332 (Nov. 2013).

139. Negrea, D., Ducu, C., Moga, S., Malinovschi, V., Monty, C. J. A., Vasile, B., Dorobantu, D. & Enachescu, M. Solar Physical Vapor Deposition Preparation and Microstructural Characterization of TiO_2 Based Nanophases for Dye-Sensitized Solar Cell Applications. *J. Nanosci. Nanotechnol.* **12,** 8746–8750. ISSN: 1533-4880 (2012).

140. Smits, K., Sarakovskis, A., Grigorjeva, L., Millers, D. & Grabis, J. The role of Nb in intensity increase of Er ion upconversion luminescence in zirconia. *J. Appl. Phys.* **115,** 213520. ISSN: 0021-8979 (June 2014).

141. Lange, S., Kiisk, V., Aarik, J., Kirm, M. & Sildos, I. Luminescence of ZrO_2 and HfO_2 thin films implanted with Eu and Er ions. *Physica Status Solidi (C) Current Topics in Solid State Physics* **4,** 938–941. ISSN: 18626351 (2007).

142. Lu, C. H., Raitano, J. M., Khalid, S., Zhang, L. & Chan, S. W. Cubic phase stabilization in nanoparticles of hafnia-zirconia oxides: Particle-size and annealing environment effects. *Journal of Applied Physics* **103.** ISSN: 00218979 (2008).

143. Ordonez-Romero, C. L., Flores J, C., Hernandez A, J., Camarillo G., E., Cabrera B., E., Garcia-Hipolito, M. & Murrieta S., H. Effects of the HfO_2 sinterization temperature on the erbium luminescence. *Journal of Luminescence* **145,** 713–716. ISSN: 00222313 (2014).

144. LeLuyer, C., Villanueva-Ibañez, M., Pillonnet, A. & Dujardin, C. HfO_2:X (X = Eu^{3+}, Ce^{3+}, Y^{3+}) sol gel powders for ultradense scintillating materials. *Journal of Physical Chemistry A* **112.** cited By 41, 10152–10155 (2008).

145. Wilk, G. D., Wallace, R. M. & Anthony, J. M. High-κ gate dielectrics: Current status and materials properties considerations. *J. Appl. Phys.* **89,** 5243–5275. ISSN: 0021-8979 (May 2001).

146. Robertson, J., Xiong, K. & Clark, S. J. Band gaps and defect levels in functional oxides. *Proceedings of the Fourth International Symposium on Transparent Oxide Thin Film for Electronics and Optics (TOEO-4)* **496,** 1–7. ISSN: 0040-6090 (2006).

147. Nadu, T., Nadu, T., Kavitha, P., Ramesh, R., Rajan, M. R. & Stella, C. Synthesis and Characterization of Cerium Oxide Nanoparticles by Using Rapid Precipitation Method. **8,** 91–93 (2015).

148. Fabris, S., Paxton, A. T. & Finnis, M. W. A stabilization mechanism of zirconia based on oxygen vacancies only. *Acta Materialia* **50,** 5171–5178. ISSN: 13596454. eprint: `0206080` (cond-mat) (2002).

149. Smits, K., Olsteins, D., Zolotarjovs, A., Laganovska, K., Millers, D., Ignatans, R. & Grabis, J. Doped zirconia phase and luminescence dependence on the nature of charge compensation. en. *Sci. Rep.* **7,** 44453. ISSN: 2045-2322 (Mar. 2017).

150. Puust, L., Kiisk, V., Eltermann, M., Mändar, H., Saar, R., Lange, S., Sildos, I., Dolgov, L., Matisen, L. & Jaaniso, R. Effect of ambient oxygen on the photoluminescence of sol–gel-derived nanocrystalline ZrO_2:Eu,Nb. *Journal of Physics D: Applied Physics* **50,** 215303 (2017).

151. Ramos-González, R., García-Cerda, L., Alshareef, H. N., Gnade, B. & Quevedo-López, M. Study of Hafnium (IV) Oxide Nanoparticles Synthesized by Polymerized Complex and Polymer Precursor Derived Sol-Gel Methods. *Materials Science Forum* **644,** 75–78. ISSN: 1662-9752 (2010).

152. Meng, J., Jiang, D. Y. & Li, Q. Luminescent properties of Eu^{3+}-doped HfO_2 powders prepared by combustion. *Key Eng. Mater.* **434-435,** 805–807. ISSN: 1013-9826, 1662-9795 (Mar. 2010).

153. Tamrakar, R. K., Bisen, D. P. & Upadhyay, K. Photoluminescence behavior of ZrO_2: Eu^{3+} with variable concentration of Eu^{3+} doped phosphor. *Journal of Radiation Research and Applied Sciences* **8,** 11–16. ISSN: 1687-8507 (Jan. 2015).

154. Martínez-Merlín, I., Guzmán-Mendoza, J., García-Hipólito, M., Sánchez-Resendiz, V. M., Lartundo-Rojas, L., Fragoso, R. J. & Falcony, C. Transparent and low surface roughness HfO_2: Tb3+, Eu^{3+} luminescent thin films deposited by USP technique. *Ceram. Int.* **42,** 2446–2455. ISSN: 0272-8842 (Feb. 2016).

155. Kiisk, V., Puust, L., Mandar, H., Ritslaid, P., Rahn, M., Bite, I., Jankovica, D., Sildos, I. & Jaaniso, R. Phase stability and oxygen-sensitive photoluminescence of ZrO_2:Eu,Nb nanopowders. *Materials Chemistry and Physics.* ISSN: 0254-0584 (2017).

156. Langford, J. I. & Wilson, A. J. C. Scherrer after sixty years: A survey and some new results in the determination of crystallite size. *Journal of Applied Crystallography* **11,** 102–113. ISSN: 0021-8898 (1978).

157. Chen, R. *Glow Curves with General Order Kinetics* 1969.

158. Hu, J., Zhu, F., Matulionis, I., Deutsch, T., Gaillard, N., Miller, E. & Madan, A. Mater. Res. Soc. Symp. Proc. Vol. 1193 2009 Materials Research Society. *Materials Research* **1193,** 2–7 (2009).

159. Lauria, A., Villa, I., Fasoli, M., Niederberger, M. & Vedda, A. Multifunctional role of rare earth doping in optical materials: nonaqueous sol-gel synthesis of stabilized cubic HfO_2 luminescent nanoparticles. en. *ACS Nano* **7,** 7041–7052. ISSN: 1936-0851, 1936-086X (Aug. 2013).

160. Liu, L. X., Ma, Z. W., Xie, Y. Z., Su, Y. R., Zhao, H. T., Zhou, M., Zhou, J. Y., Li, J. & Xie, E. Q. Photoluminescence of rare earth3+ doped uniaxially aligned HfO_2 nanotubes prepared by sputtering with electrospun polyvinylpyrolidone nanofibers as templates. *J. Appl. Phys.* **107,** 024309. ISSN: 0021-8979, 1089-7550 (Jan. 2010).

161. Smits, K., Grigorjeva, L., Millers, D., Sarakovskis, A., Opalinska, A., Fidelus, J. D. & Lojkowski, W. Europium doped zirconia luminescence. *Opt. Mater.* **32,** 827–831. ISSN: 0925-3467 (June 2010).

162. Díaz-Torres, L. a., Rosa-Cruz, E. D. L., Salas, P. & Angeles-Chavez, C. Concentration enhanced red upconversion in nanocrystalline ZrO_2:Er under IR excitation. *J. Phys. D. Appl. Phys.* **37,** 2489–2495. ISSN: 0022-3727 (2004).

163. Soares, M. R. N., Holz, T., Oliveira, F., Costa, F. M. & Monteiro, T. Tunable green to red ZrO_2:Er nanophosphors. en. *RSC Adv.* **5,** 20138–20147. ISSN: 2046-2069 (Feb. 2015).

164. Smits, K., Jankovica, D., Sarakovskis, A. & Millers, D. Up-conversion luminescence dependence on structure in zirconia nanocrystals. *Opt. Mater.* **35,** 462–466. ISSN: 0925-3467 (Jan. 2013).

165. Liu, H.-Q., Wang, L.-L., Chen, S.-G. & Zou, B.-S. Optical properties of nanocrystal and bulk ZrO_2: Eu^{3+}. *J. Alloys Compd.* **448,** 336–339. ISSN: 0925-8388 (Jan. 2008).

166. Malta, O., dos Santos, M., Thompson, L. & Ito, N. Intensity parameters of 4f—4f transitions in the Eu(dipivaloylmethanate)3 1, 10-phenanthroline complex. *Journal of Luminescence* **69,** 77–84. ISSN: 0022-2313 (1996).

167. Dačanin, L., Lukić, S. R., Petrović, D. M., Nikolić, M. & Dramićanin, M. D. Judd-Ofelt analysis of luminescence emission from Zn_2SiO_4:Eu^{3+} nanoparticles obtained by a polymer-assisted solgel method. *Physica B: Condensed Matter* **406,** 2319–2322. ISSN: 09214526 (2011).

168. Görller-Walrand, C., Fluyt, L., Ceulemans, A. & Carnall, W. T. Magnetic dipole transitions as standards for Judd-Ofelt parametrization in lanthanide spectra. *The Journal of Chemical Physics* **95,** 3099–3106. ISSN: 00219606 (1991).

169. Tanabe, S., Ohyagi, T., Soga, N. & Hanada, T. Compositional dependence of Judd-Ofelt parameters of Er^{3+} ions in alkali-metal borate glasses. *Phys. Rev. B* **46,** 3305–3310 (1992).

170. Prasanna Kumar, S., Hari Krishna, R., Kottam, N., Krishna Murthy, P., Manjunatha, C., Preetham, R., Shivakumara, C. & Thomas, T. Understanding the photoluminescence behaviour in nano $CaZrO_3$:Eu^{3+} pigments by Judd-Ofelt intensity parameters. *Dyes and Pigments* **150,** 306–314. ISSN: 01437208 (2018).

171. Casolco, S. R., Xu, J. & Garay, J. E. Transparent/translucent polycrystalline nanostructured yttria stabilized zirconia with varying colors. *Scripta Materialia* **58,** 516–519. ISSN: 13596462 (2008).

172. Alaniz, J. E., Perez-Gutierrez, F. G., Aguilar, G. & Garay, J. E. Optical properties of transparent nanocrystalline yttria stabilized zirconia. *Optical Materials* **32,** 62–68. ISSN: 09253467 (2009).

173. Tsukuma, K., Yamashita, I. & Kusunose, T. Transparent 8 mol% Y_2O_3-ZrO_2 (8Y) ceramics. *Journal of the American Ceramic Society* **91,** 813–818. ISSN: 00027820 (2008).

174. Mariselvam, K. & Liu, J. A novel Er^{3+} ions doped zirconium magnesium borate glass with very high quantum efficiency for green laser and optical amplifier applications. *Solid State Sciences* **111,** 106443. ISSN: 12932558 (2021).

175. Yamashita, I., Kudo, M. & Tsukuma, K. Development of highly transparent zirconia ceramics. *Tosoh Res. Tech. Review* **56,** 11–16 (2012).

176. Durán, P., Recio, P., Jurado, J., Pascual, C. & Moure, C. Preparation, Sintering, and Properties of Translucent Er2O3-Doped Tetragonal Zirconia. *Journal of the American Ceramic Society* **72.** cited By 34, 2088–2093 (1989).

177. Pabst, W. & Hříbalová, S. Light scattering models for describing the transmittance of transparent and translucent alumina and zirconia ceramics. *Journal of the European Ceramic Society* **41,** 2058–2075. ISSN: 1873619X (2021).

178. Anselmi-Tamburini, U., Woolman, J. & Munir, Z. Transparent nanometric cubic and tetragonal zirconia obtained by high-pressure pulsed electric current sintering. *Advanced Functional Materials* **17.** cited By 181, 3267–3273 (2007).

179. Klimke, J., Trunec, M. & Krell, A. Transparent tetragonal yttria-stabilized zirconia ceramics: Influence of scattering caused by birefringence. *Journal of the American Ceramic Society* **94.** cited By 98, 1850–1858 (2011).

180. Zhang, H. & Sulzer, D. Regulation of striatal dopamine release by presynaptic auto- and heteroreceptors. *Basal Ganglia* **2.** cited By 39, 5–13 (2012).

181. Lin, Y. S., Chang, C. H. & Gopalan, R. Improvement of Thermal Stability of Porous Nanostructured Ceramic Membranes. *Industrial and Engineering Chemistry Research* **33,** 860–870. ISSN: 15205045 (1994).

182. Koebrugge, G. W., Winnubst, L. & Burggraaf, A. J. Thermal stability of nanostructured titania and titania-ceria ceramic powders prepared by the sol-gel process. *Journal of Materials Chemistry* **3,** 1095–1100. ISSN: 09599428 (1993).

183. Keyvani, N., Azarniya, A., Hosseini, H. R. M., Abedi, M. & Moskovskikh, D. Thermal stability and strain sensitivity of nanostructured aluminum titanate (Al2TiO5). *Materials Chemistry and Physics* **223,** 202–208. ISSN: 02540584 (2019).

184. He, Y., Liu, K., Xiang, B., Zhou, C., Zhang, L., Liu, G., Guo, X., Zhai, J., Li, T. & Kong, L. B. An overview on transparent ceramics with pyrochlore and fluorite structures. *Journal of Advanced Dielectrics* **10.** ISSN: 20101368 (2020).

185. Liu, X., Zhou, J., Zhou, S., Yue, Y. & Qiu, J. Transparent glass-ceramics functionalized by dispersed crystals. *Progress in Materials Science* **97,** 38–96. ISSN: 00796425 (2018).

186. Bos, A. J. Thermoluminescence as a research tool to investigate luminescence mechanisms. *Materials* **10.** ISSN: 19961944 (2017).

187. Goldstein, A. & Krell, A. Transparent Ceramics at 50: Progress Made and Further Prospects. *Journal of the American Ceramic Society* **99,** 3173–3197. ISSN: 15512916 (2016).

188. Lamas, D. G., Lascalea, G. E. & Walsöe De Reca, N. E. Synthesis and characterization of nanocrystalline powders for partially stabilized zirconia ceramics. *Journal of the European Ceramic Society* **18,** 1217–1221. ISSN: 09552219 (1998).

189. Srdić, V., Winterer, M. & Hahn, H. Sintering behavior of nanocrystalline zirconia prepared by chemical vapor synthesis. *Journal of the American Ceramic Society* **83.** cited By 111, 729–736 (2000).

190. Garvie, R. C. Stabilization of the tetragonal structure in zirconia microcrystals. *Journal of Physical Chemistry* **82,** 218–224. ISSN: 00223654 (1978).

191. Kiisk, V., Puust, L., Mändar, H., Ritslaid, P., Rähn, M., Bite, I., Jankovica, D., Sildos, I. & Jaaniso, R. Phase stability and oxygen-sensitive photoluminescence of ZrO_2:Eu,Nb nanopowders. *Mater. Chem. Phys.* **214,** 135–142. ISSN: 0254-0584 (Aug. 2018).

192. Ćirić, A., Aleksić, J., Barudžija, T., Antić, Ž., Đorđević, V., Medić, M., Periša, J., Zeković, I., Mitrić, M. & Dramićanin, M. D. Comparison of three ratiometric temperature readings from the Er^{3+} upconversion emission. *Nanomaterials* **10,** 1–10. ISSN: 20794991 (2020).

193. Alzyab, B., Perry, C. H. & Ingel, R. P. High-pressure phase transitions in Zirconia and yttria-doped Zirconia. en. *J. Am. Ceram. Soc.* **70,** 760–765. ISSN: 0002-7820, 1551-2916 (Oct. 1987).

194. Garvie, R. C. The Occurrence of Metastable Tetragonal Zirconia as a Crystallite Size Effect. *The Journal of Physical Chemistry* **69,** 1238–1243. ISSN: 0022-3654 (1965).

195. Torchynska, T., El Filali, B., Khomenkova, L., Portier, X. & Gourbilleau, F. Phase transformation and light emission in Er-doped Si-rich HfO_2 films prepared by magnetron sputtering. *Journal of Vacuum Science & Technology A* **37,** 031503. ISSN: 0734-2101 (2019).

196. Jayaraman, V., Sagadevan, S. & Sudhakar, R. Studies on Optical and Electrical Properties of Hafnium Oxide Nanoparticles. *J. Electron. Mater.* **46,** 4392–4397. ISSN: 0361-5235, 1543-186X (July 2017).

197. Sharma, U., Kumar, G., Mishra, S. & Thomas, R. Advancement of Gate Oxides from SiO2 to High-k Dielectrics in Microprocessor and Memory. en. *J. Phys. Conf. Ser.* **2267,** 012142. ISSN: 1742-6588, 1742-6596 (May 2022).

198. Mukhachov, A. P., Kharitonova, O. A. & Terentieva, O. A. Hafnium oxide as efficient material for a new generation dielectric. en. *Acta Phys. Pol. A* **133,** 778–780. ISSN: 0587-4246, 1898-794X (Apr. 2018).

199. Ha, J.-H., McIntyre, P. C. & (KJ) Cho, K. First principles study of the HfO_2/SiO2 interface: Application to high-k gate structures. *J. Appl. Phys.* **101,** 033706. ISSN: 0021-8979, 1089-7550 (Feb. 2007).

200. Robertson, J. High dielectric constant oxides. en. *Eur. Phys. J. Appl. Phys.* **28,** 265–291. ISSN: 1286-0042, 1286-0050 (Dec. 2004).

201. Cheema, D. A., Danial, M. O., Hanif, M. B., Alghamdi, A. S., Ramadan, M., Khaliq, A., Khan, A. F., Subhani, T. & Motola, M. Intrinsic Properties and Future Perspective of HfO_2/V2O5/HfO_2Multi-Layer Thin Films via E-Beam Evaporation as a Transparent Heat Mirror. en. *Coat. World* **12,** 448. ISSN: 1527-1129 (Mar. 2022).

202. Laganovska, K., Olsteins, D., Smits, K., Bite, I. & Bikse, L. Formation of translucent nanostructured zirconia ceramics. *J. Eur. Ceram. Soc.* **41,** 6641–6648. ISSN: 0955-2219 (Oct. 2021).

203. Kim, S. J., Mohan, J., Summerfelt, S. R. & Kim, J. Ferroelectric Hf0.5Zr0.5O2 Thin Films: A Review of Recent Advances. *JOM* **71,** 246–255. ISSN: 1543-1851 (Jan. 2019).

204. Clima, S., Govoreanu, B., Jurczak, M. & Pourtois, G. HfOx as RRAM material – First principles insights on the working principles. *Microelectron. Eng.* **120,** 13–18. ISSN: 0167-9317 (May 2014).

205. Reis, D. *et al.* Design and Analysis of an Ultra-Dense, Low-Leakage, and Fast FeFET-Based Random Access Memory Array. *IEEE Journal on Exploratory Solid-State Computational Devices and Circuits* **5,** 103–112. ISSN: 2329-9231 (Dec. 2019).

206. Puglisi, F. M., Pavan, P., Padovani, A. & Larcher, L. A compact model of hafnium-oxide-based resistive random access memory. *Proceedings of 2013 International Conference on IC Design & Technology (ICICDT)* (2013).

207. Hubbard, K. J. & Schlom, D. G. Thermodynamic stability of binary oxides in contact with silicon. *J. Mater. Res.* **11,** 2757–2776. ISSN: 0884-2914 (Nov. 1996).

208. Gavartin, J. L., Shluger, A. L., Foster, A. S. & Bersuker, G. I. The role of nitrogen-related defects in high-k dielectric oxides: Density-functional studies. *J. Appl. Phys.* **97,** 053704. ISSN: 0021-8979 (Mar. 2005).

209. Papernov, S. *et al.* Optical properties of oxygen vacancies in HfO_2 thin films studied by absorption and luminescence spectroscopy. en. *Opt. Express* **26,** 17608–17623. ISSN: 1094-4087 (June 2018).

210. Vitola, V., Bite, I., Millers, D., Zolotarjovs, A., Laganovska, K., Smits, K. & Spustaka, A. The boron effect on low temperature luminescence of $SrAl_2O_4$:Eu, Dy. *Ceram. Int.* **46,** 26377–26381. ISSN: 0272-8842 (Nov. 2020).

211. Kitis, G., Gomez-Ros, J. M. & Tuyn, J. W. N. Thermoluminescence glow-curve deconvolution functions for first, second and general orders of kinetics. en. *J. Phys. D Appl. Phys.* **31,** 2636. ISSN: 0022-3727, 1361-6463 (Oct. 1998).

212. Mergia, K., Liedtke, V., Speliotis, T., Apostolopoulos, G. & Messoloras, S. *Thermo-Mechanical Behaviour of HfO$_2$ Coatings for Aerospace Applications* in *1st International Conference On New Materials for Extreme Environment* **59** (Trans Tech Publications Ltd, Feb. 2009), 87–91.

213. Roy, C., Noor-A-Alam, M., Choudhuri, A. & Ramana, C. Synthesis and microstructure of Gd$_2$O$_3$-doped HfO$_2$ ceramics. *Ceramics International* **38,** 1801–1806 (2012).

214. Fujimori, H., Yashima, M., Sasaki, S., Kakihana, M., Mori, T., Tanaka, M. & Yoshimura, M. Internal distortion in ceria-doped hafnia solid solutions: High-resolution x-ray diffraction and Raman scattering. *Physical Review B* **64,** 134104 (2001).

215. Wang, C., Akbar, S., Chen, W. & Patton, V. Electrical properties of high-temperature oxides, borides, carbides, and nitrides. *Journal of materials science* **30,** 1627–1641 (1995).

216. Malta, O., dos Santos, M., Thompson, L. & Ito, N. Intensity parameters of 4f—4f transitions in the Eu(dipivaloylmethanate)3 1, 10-phenanthroline complex. *Journal of Luminescence* **69,** 77–84. ISSN: 0022-2313 (1996).